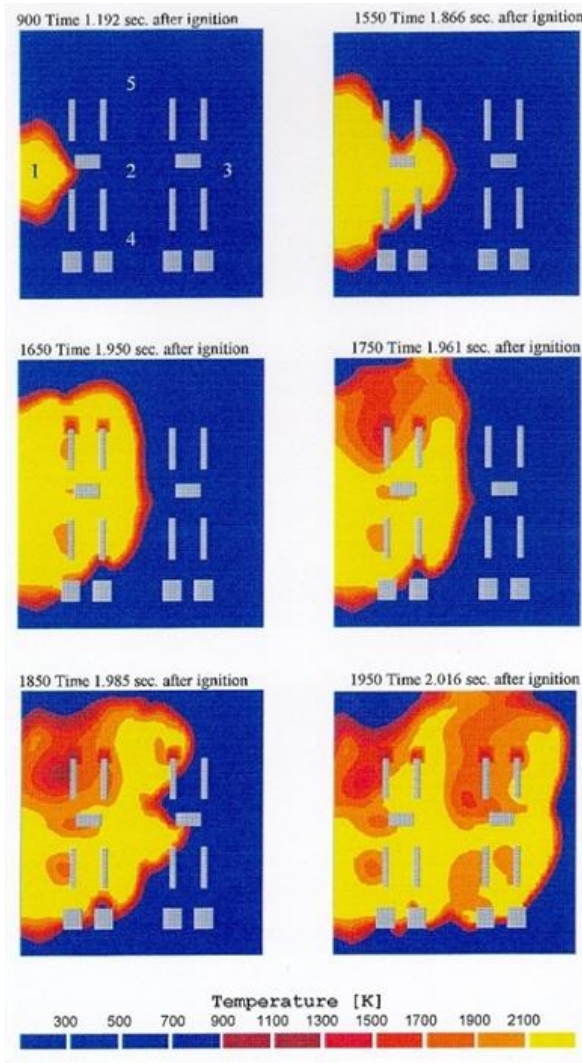


Properly Evaluate Building and Facility Siting Risks



An ioMosaic Corporation White Paper

G. A. Melhem, Ph.D., FAIChE

melhem@iomosaic.com

IO MOSAIC CORPORATION

Properly Evaluate Building and Facility Siting Risks

Safety and Risk Management Practices

authored by

Georges A. MELHEM, Ph.D., FAIChE

March 24, 2020

Contents

| | | |
|-----|---|-----------|
| 1. | What is Driving Facility Siting Studies? | 3 |
| 2. | Overview of Fire, Toxicity, and Explosion Risks | 3 |
| 3. | Potential Impact of Facility Siting Studies | 4 |
| 4. | Building Risks Evaluation Methods | 4 |
| 5. | The ioMosaic Approach | 6 |
| 6. | A Consequence Based Case Study | 8 |
| 6.1 | TNT Equivalence Method | 9 |
| 6.2 | TNO Multi-energy Method | 10 |
| 6.3 | Baker-Strehlow Method | 11 |
| 6.4 | Computational Fluid Dynamics Method | 12 |
| 7. | Mitigation and Risk Reduction Measures | 14 |
| 8. | Conclusions | 14 |
| 9. | How can we help? | 15 |
| | Appendices | 16 |
| | A Overview of Explosion Modeling for Facility Siting | 17 |
| 1. | Deflagrations Vs. Detonations | 18 |
| 2. | Damage From Explosions | 18 |
| 3. | Blast Waves | 19 |
| 4. | Blast Loading Mechanisms | 22 |
| 4.1 | Diffraction Loading | 23 |
| 4.2 | Drag Loading | 25 |
| 4.3 | Peak Reflected Pressure Ratios | 26 |
| 5. | Building Blast Loading | 29 |

| | | |
|----------|---|-----------|
| 5.1 | Front Wall Loading | 29 |
| 5.2 | Side Walls and Roof Loading | 30 |
| 5.3 | Rear Wall Loading | 32 |
| 5.4 | Frame Loading | 33 |
| 5.5 | Negative Pressure and Rebound Loading | 33 |
| 6. | Structural Dynamics | 34 |
| B | Vapor Cloud Explosion Modeling | 39 |
| 1. | Introduction | 39 |
| 2. | Characteristics of Condensed Phase Explosions | 40 |
| 3. | UVCE Incident Histories | 42 |
| 4. | Theoretical and Experimental UVCE Studies | 43 |
| 5. | Obstacles and Confinement Effects | 46 |
| 6. | Jet Ignition Effects | 47 |
| 7. | <i>TNT</i> Equivalence Analysis | 48 |
| 8. | <i>TNO</i> 's Shock Wave Model | 53 |
| 9. | <i>TNO</i> Multi-Energy | 54 |
| 10. | The Baker-Strehlow Method | 55 |
| 11. | Detonation Analysis | 66 |
| 12. | Reaction Zone Length | 67 |
| 13. | Cell Size | 67 |
| 14. | Critical Energy | 68 |
| 15. | Flame Acceleration Mechanisms and DDT | 69 |
| 16. | Detonation Potential of UVCE's | 70 |
| 17. | Tank Overpressurization | 71 |
| 18. | Gas Dynamics | 73 |
| 18.1 | Example: Shock tube problem | 73 |
| 18.2 | Solution | 73 |
| 18.3 | Example: Explosion gas dynamics | 76 |
| 18.4 | Solution | 77 |

1. What is Driving Facility Siting Studies?

Large oil and gas and chemical processing plants operate facilities where hazardous materials are processed and/or stored. These facilities include buildings with varying levels of occupancy that may be at risk from accidental releases that can cause fire and explosion damage and/or toxic chemical exposure.

The design of older facilities may have not initially considered/addressed facility siting risk and may have placed more emphasis on operability and efficiency of operations. It is not typical, for example, for an oil and gas processing facility that was built in the 1950s to have blast resistant control rooms or office buildings, even though these buildings may be very close to operating units processing large volume of hazardous chemicals.

A proper facility siting study considers explosion, fire, and toxicity risks to occupants of buildings. Facility siting risk considerations are required under the process hazards analysis (PHA) element of the process safety management (PSM) standard in the United States. Over 50 % of the OSHA refinery national emphasis program (NEP) citations for PHAs were related to facility siting or human factors ¹. Recognized and generally accepted good engineering practices (RAGAGEP) published by the American institute of chemical engineers (AIChE) center for chemical process safety (CCPS) and the American petroleum institute (API) provide more specific guidance on how facility siting studies should be conducted:

- API Recommended Practice 752, 3_{rd} Edition, Management of Hazards Associated with Location of Process Plant Permanent Buildings, 2009.
- API Recommended Practice 753, 3_{rd} Edition, Management of Hazards Associated with Location of Process Plant Portable Buildings, 2012.
- API Recommended Practice 756, Management of Hazards Associated with Location of Process Plant Tents, 1_{st} Edition, 2014.
- AIChE/CCPS Guidelines for Siting and Layout of Facilities, 2_{nd} Edition, 2018.

2. Overview of Fire, Toxicity, and Explosion Risks

External fire risks to occupants of buildings are usually low and inherently mitigated to some degree. In general, fires that are external to buildings allow building occupants enough time to escape because the fires burn from the outside to the inside. Considerations and availability of adequate and clear escape and evacuation routes are key to addressing and reducing fire risks to building occupants.

Toxicity risks to building occupants can be high, especially if the building air handling systems are not equipped with early warning systems, automatic detection and shutdown or manual shutdown

¹Also see OSHA Instruction CPL 2-2.45A CH-1, September 13, 1994, Directorate of Compliance Programs, https://www.osha.gov/pls/oshaweb/owadisp.show_document?p_id=1558&p_table=directives on September 14th, 2019.

options. Shutdown of air handling systems and shelter in place for buildings at risk can reduce the risk to occupants. Software solutions such as SuperChems Expert™² can model a variety of risk reduction measures as well as the ingress of toxic materials into buildings and the toxic dose response of occupants.

Provision of personal protective equipment (PPE) for safe evacuation, provision of emergency communications equipment, designation of safe evacuation routes and assembly areas, implementation of proper head count procedures, etc., are common sense fire and toxicity risks reduction measures.

Explosion risks tend to be to more dominant risks to building occupants simply because of building partial or total collapse or the falling of heavy equipment/fixtures on occupants. Occupant risk is typically related to building damage using overpressure criteria, overpressure impulse diagrams, or detailed structural dynamics estimates.

Temporary and portable building structures are often exposed to higher fire, toxicity, and explosion risks than permanent buildings. A reasonable method for assessing risks to occupants of those types of structures is to assume that the occupants are outdoors, i.e. not within the confines of a building or structure.

This paper will focus on explosion overpressure risks and provides an example of how different methods can be used to assess the potential risks and the explosion damage.

3. Potential Impact of Facility Siting Studies

Building risk evaluation methodologies that are too conservative can lead to excessive mitigation costs without achieving the intended risk reduction. Building risk evaluation methodologies that are inadequate can leave companies exposed to high levels of risk for its portfolio of buildings.

Depending on the scale of operations, companies will need to balance building mitigation costs with risk reduction for occupied buildings. The portfolio of building risk can be significant for large companies with global presence. There is a need to establish a systematic methodology for:

- (a) Identifying the buildings at risk,
- (b) Assessing if the risk is tolerable, and
- (c) Cost effective risk reduction where applicable to as low as reasonably practicable (ALARP).

4. Building Risks Evaluation Methods

There are several well established methods for the evaluation of building risk. They can be classified into three general categories:

²SuperChems™ is a component of Process Safety Office®

E - Experience Based: The Experience Based methods rely primarily on safe separation distances developed based on historical incident data or consensus based on long operating experiences. These types of methods were popular with insurance companies underwriting the risk of chemical and/or oil and gas facilities. These methods are still used today for risk screening although many of the charts initially proposed by insurance companies have been withdrawn. Safe separation tables or charts are often used. An example is provided in Figure 1.1.

C - Consequence Based: In Consequence based methods a worst case or worst credible case scenario is first selected. The hazard contours are then established, and the building risk is assessed based on the consequences of the selected design scenario. Implicit in the selection of the design scenario is a likelihood of occurrence, or an implied level of risk tolerability.

R - Risk Based: In risk based methods, also referred to as Quantitative Risk Analysis (QRA) methods, all scenarios leading to loss of containment are first identified. A frequency of occurrence is then established for each scenario. Risk contours are established for an entire facility. These contours are then used to identify buildings and other infrastructure at risk. For facility siting, risk contours are typically established for specific overpressure levels. For example, a structure of typical construction (not blast proof) falling within the 3 psi contours at a frequency of 1/10,000 years or more would be considered at risk. An example is provided in Figure 1.2 using SuperChems Expert™.

All three methods described above have advantages and disadvantages and are subject to the same scenario flow rate and flammable dispersion uncertainties.

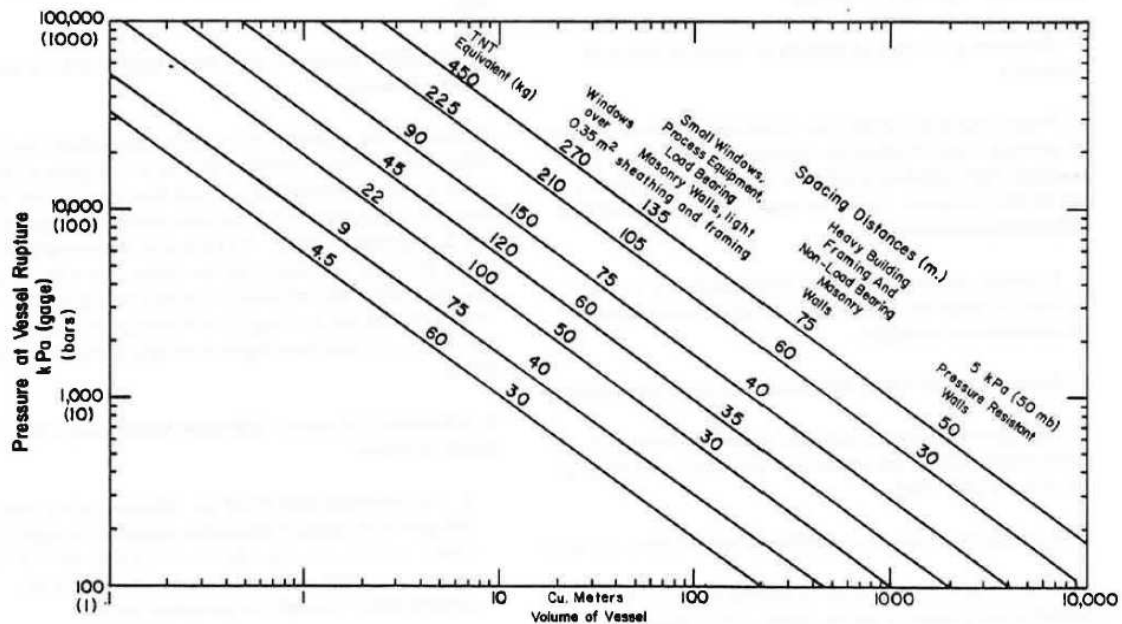
The consequence-based approach does have the advantage of simplicity and speed. Typically, the site is first surveyed, and areas of congestion are identified. The congested volumes are filled with a reasonable selection of a flammable material and form the basis of the explosion overpressure estimates. The explosion scenarios are not assigned a frequency of occurrence.

In the risk-based approach, myriads of scenarios are considered for flammable dispersion with consideration of wind directions, atmospheric stability, and probabilities of occurrence. The overpressure estimates will be in general like the consequence-based approach but with a better understanding of what flammable materials are involved and at what frequency we expect the overpressure to occur.

Methods E and C do not provide a straight forward framework for determining if the money spent on mitigation will provide a good risk reduction return on investment, i.e. the monetary value of risks averted would have to far outweigh the monetary value of what is spent on risk reduction.

Unless a clear basis for the assessment is agreed upon upfront, companies run the risk of spending excessive amounts of money without receiving a coherent risk mitigation and reduction. How much money would a facility be willing to spend on losses not yet incurred due to building risk?

Figure 1.1: An Experience Based Facility Siting Chart for Overpressure



5. The ioMosaic Approach

Proper building risk evaluation requires an assessment of the structural response of buildings that are exposed to explosion overpressure for example. This can be accomplished by simple or complex methods. Simple methods may include overpressure-vs-damage tables, pressure-impulse diagrams for specific building components, single degree of freedom or multiple degree of freedom methods, and in some cases detailed finite element methods. Finite element methods for the assessment of structural response and the prediction of failure mechanisms and criteria are well established and can be very accurate.

Unfortunately, methods for establishing the forcing function (explosion models used to develop overpressure-time history) used in these structural dynamics estimates have many uncertainties. These uncertainties include but are not limited to (a) the scenario identification and associated leak rates especially for multiphase flow, the subsequent dispersion to the lower explosion limits and the mass of cloud, the immediate and/or delayed ignition, the flame acceleration mechanisms due to turbulence, blockage, fuel sensitivity, etc. For vapor cloud explosion involving gaseous or two-phase materials, the center of the explosion is almost always not the initial location/point of ignition.

Incident data and accident investigation studies indicate that the center of explosion where high overpressure is produced is highly correlated with congestion and confinement. As a result many simple methods for the calculation of these overpressure-time histories rely on the identification of areas of heavy congestion and/or confinement in facilities. Note that the scenarios leading to flammable mixture accumulation within the congested/confined volume can originate in a different

Figure 1.2: A Facility Siting Building Risk Summary using SuperChems Expert™

| GUID | Description, Function, or Service | Type | Structural Class | Sensitive Receptor | Risk Frequency /yr | X1. m | Y1. m |
|--------------------------------------|-----------------------------------|--------------------------------|------------------|--------------------|--------------------|---------|---------|
| E1A8ECCC-EC59-11DC-BAED-00151740847B | Operator Shelter | Building - Operator Shelter | CCPS-E | No | 4.866E-05 | 1270.81 | 258.37 |
| 35FB9FFC-EC5B-11DC-BAED-00151740847B | Contractor Shelter | Building - Contractor Shelter | CCPS-B | No | 2.502E-05 | 1257.42 | 185.65 |
| AB0770F3-EC59-11DC-BAED-00151740847B | Operator Shelter | Building - Operator Shelter | CCPS-E | No | 2.219E-05 | 1340.67 | 288.04 |
| 6AF1F792-EC5B-11DC-BAED-00151740847B | Maintenance Shelter #4 | Building - Maintenance Shelter | CCPS-B | No | 1.782E-05 | 1266.03 | 161.72 |
| 7CBFB0B1-EC59-11DC-BAED-00151740847B | Building - SS-B-212 | Building - SS-B-212 | CCPS-E | No | 1.711E-05 | 1297.61 | 161.72 |
| 53EE0692-EC59-11DC-BAED-00151740847B | Operator Shelter | Building - Operator Shelter | CCPS-E | No | 1.477E-05 | 1404.78 | 222.01 |
| D9F2A40A-D2A5-11DC-B566-001438EB97DD | Local Control Room 3 | Building - Control Room | CCPS-E | No | 1.380E-05 | 1401.00 | 166.00 |
| A443694E-EC58-11DC-BAED-00151740847B | Operator Shelter | Building - Operator Shelter | CCPS-A | No | 1.243E-05 | 1342.58 | 350.24 |
| 411B74A0-EC57-11DC-BAED-00151740847B | Operator Shelter | Building - Operator Shelter | CCPS-E | No | 9.756E-06 | 1144.50 | 292.82 |
| 13470652-D2A5-11DC-B566-001438EB97DD | Local Control Room 1 | Building - Control Room | CCPS-E | No | 8.784E-06 | 1181.23 | 97.87 |
| 6345CDB1-DDC2-11DC-92D9-001DD9E780C5 | Building - Maintenance Shelter | Building - Maintenance Shelter | CCPS-B | No | 5.620E-06 | 1164.59 | 455.50 |
| 36960681-DDC3-11DC-92D9-001DD9E780C5 | Building - Maintenance Shelter | Building - Maintenance Shelter | CCPS-B | No | 4.823E-06 | 1169.38 | 474.64 |
| BF878867-EC57-11DC-BAED-00151740847B | Building - SS-B-127 | Building - SS-B-127 | CCPS-E | No | 4.143E-06 | 1057.42 | 95.69 |
| 7C558E21-DDC3-11DC-92D9-001DD9E780C5 | Building - SS-B-122 | Building - SS-B-122 | CCPS-E | No | 3.668E-06 | 1050.72 | 503.35 |
| 119D9D90-D2A6-11DC-B566-001438EB97DD | Local Control Room 2 | Building - Control Room | CCPS-E | No | 3.231E-06 | 1170.17 | 509.77 |
| CD9157F7-EC58-11DC-BAED-00151740847B | Operator Shelter | Building - Operator Shelter | CCPS-E | No | 3.111E-06 | 1369.38 | 530.14 |
| B9840DF1-DOB7-11DC-92D9-001DD9E780C5 | Building - MOB #3 | Building - MOB #3 | CCPS-C | No | 2.817E-06 | 1161.72 | -59.33 |
| AA7D59E1-DDC3-11DC-92D9-001DD9E780C5 | Building - Operator Shelter | Building - Operator Shelter | CCPS-E | No | 2.749E-06 | 1079.43 | 448.80 |
| CEA5E7D1-DOB7-11DC-92D9-001DD9E780C5 | Building - MOB #4 | Building - MOB #4 | CCPS-C | No | 1.780E-06 | 1239.23 | -155.02 |
| 6AC3B42E-D2A8-11DC-B566-001438EB97DD | Central Tool Room | Building - Central Tool Room | CCPS-B | No | 1.686E-06 | 1176.13 | -139.57 |
| DD04D854-D2A4-11DC-B566-001438EB97DD | Local Control Room 6 | Building - Control Room | CCPS-E | No | 1.525E-06 | 991.45 | 96.17 |
| 26B50503-EC61-11DC-BAED-00151740847B | Contractor Shelter | Building - Contractor Shelter | CCPS-B | No | 1.424E-06 | 1058.37 | 543.54 |
| 0B736B65-EC5D-11DC-BAED-00151740847B | Building - SS-B-223 | Building - SS-B-223 | CCPS-E | No | 1.221E-06 | 1401.91 | 596.17 |
| 59569A1C-D2A5-11DC-B566-001438EB97DD | Local Control Room 5 | Building - Control Room | CCPS-E | No | 1.202E-06 | 956.56 | 505.51 |

area in the facility.

As a result, many companies consider the use of single degree of freedom structural dynamics methods adequate for the evaluation of building structural response to explosion overpressure loading.

The quality of building risk assessment will depend heavily on the quality of scenario identification, and consequence evaluation. If cost-benefit is to be used for proper selection of risk reduction measures, then the frequency or likelihood of the scenario will be an important factor as well.

If the number of buildings at risk for example is 100 buildings for all global operations of a large company, and the associated mitigation costs are on average \$1,000,000 per building (control room relocation costs will cost much more than that), total risk reduction expenditures will be close to \$100 million dollars.

As a result, companies should consider the use of risk screening and risk based methods to evaluate building risks and risk reduction cost benefit. In particular, a base-line QRA has to be first conducted to establish overpressure-frequency contours for a specific unit and/or facility. Onsite societal risk data should also be considered.

More importantly, the base-line QRA can be modified to assess the impact of mitigation measures of the risk levels. It may be much more cost effective to consider the addition of detection and isolation systems to reduce the likelihood and impact of large release scenarios than the relocation or blast proofing of control rooms, especially for older facilities.

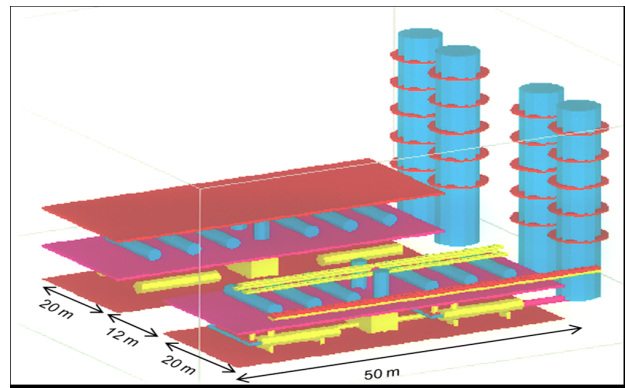
In order to conduct a QRA study, infrastructure information would have to be established. For example, our QRA software, SuperChems Expert™, includes a database with the capability of

locating buildings and other critical infrastructure on the actual site map and then defining the infrastructure information including occupancy levels for different types of population, construction type, etc. The QRA site map will then become the actual building database for cataloging and viewing the overpressure time histories and the structural response of each building (SDOF). Note that the source term and explosion dynamics models in SuperChems Expert™ are very detailed and well validated.

6. A Consequence Based Case Study

To illustrate the use of some of the blast loading models used in SuperChems Expert™, we consider the following release of 14,000 kgs of butane [1, 2].

Four methods of assessment are considered: (1) the TNT equivalence assessment [3], (2) the TNO multi-energy method [4], (3) the Baker-Strehlow method [5], and (4) the AutoReaGas [6] computational fluid dynamics estimate. Data used to perform the consequence modeling is provided below:

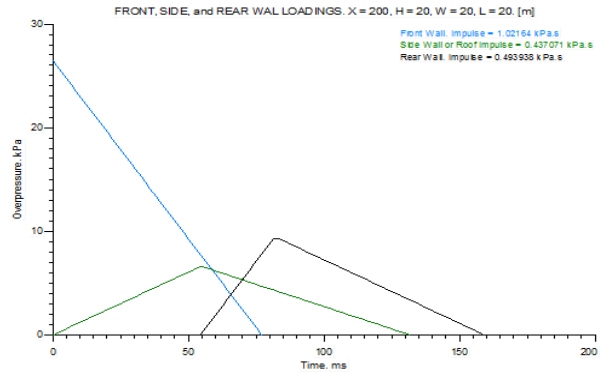


- Two identical units separated by a distance of 12 meters
- 14,000 kg of butane are released over 10 minutes
- A three meters thick layer forms
- Ignition occurs inside the process unit
- The nearest occupied building is 200 meters from the unit (20x20x20)

SuperChems Expert™ provides numerous tools for explosion modeling including methods 1, 2, and 3 discussed above. SuperChems Expert™ also includes additional explosion models such as one dimensional explosion dynamics, vessel deflagration dynamics, and numerous models for deflagration dynamics vent sizing for gases, dusts, and hybrid systems.

6.1 TNT Equivalence Method

A simple TNT equivalence assessment was conducted using a yield factor of 10 % as recommended by EPA for worst case scenario. Overpressure vs. time loading on the front, side/roof, and rear walls of the building are shown graphically. The dynamic loads can be used in conjunction with a structural dynamics computer code to determine the potential for building damage.



Impulse loading data from the TNT equivalence model is shown in tabular form. The impulse data can be used to estimate the degree of potential building damage using impulse-damage diagrams for specific building types. Impulse-damage diagrams published by the US DOD are popular and can be used.

```

**BUILDING BLAST LOADING RESULTS
Positive phase duration. s                0.077
Incident overpressure. kPa                12.585
Incident pressure. kPa                   113.910

Front wall impulse. kPa.s                 1.022
Side wall or roof impulse. kPa.s         0.437
Rear wall impulse. kPa.s                 0.494

Air Cp/Cv ratio                          1.404
Side wall Ce factor                       0.770
Speed of sound in air. m/s               346.402
Shock velocity. m/s                      366.356
Blast wind velocity. m/s                 31.139
Blast wind dynamic overpressure. kPa     0.575
Blast wave length. m                     28.263
    
```

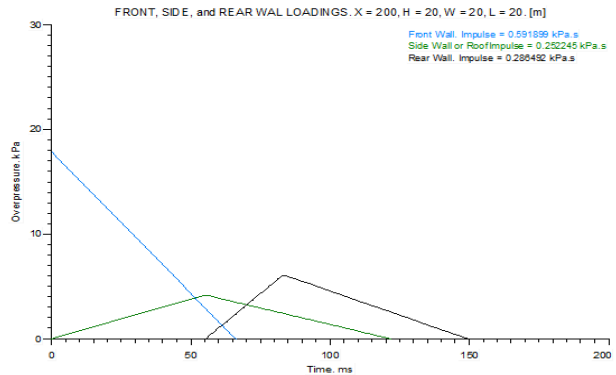
In addition to impulse tables and dynamic pressure profiles, SuperChems Expert™ provides overpressure and impulse information at user defined thresholds for the TNT equivalence method.

| Distance. m | Area. m2 | Overpressure. kPa | Impulse. kPa.s | Duration. ms |
|-------------|------------|-------------------|----------------|--------------|
| 236.343 | 175482.554 | 10.000 | 0.464 | 82.022 |
| 147.343 | 68203.722 | 20.000 | 0.742 | 66.790 |
| 116.650 | 42748.613 | 30.000 | 0.933 | 57.954 |
| 100.252 | 31574.606 | 40.000 | 1.079 | 52.164 |
| 89.701 | 25278.310 | 50.000 | 1.198 | 48.002 |
| 82.181 | 21217.445 | 60.000 | 1.300 | 44.818 |
| 74.071 | 17236.531 | 75.000 | 1.428 | 41.181 |

| Radial distance. m | Overpressure. kPa | Impulse. kPa.s | Duration. ms |
|--------------------|-------------------|----------------|--------------|
| 10.000 | 5369.034 | 3.105 | 2.574 |
| 20.000 | 1441.978 | 2.858 | 8.453 |
| 30.000 | 596.296 | 2.592 | 17.335 |
| 40.000 | 307.718 | 2.271 | 23.558 |
| 50.000 | 182.899 | 1.967 | 29.139 |
| 100.000 | 40.198 | 1.082 | 52.068 |
| 200.000 | 12.560 | 0.548 | 77.226 |
| 300.000 | 7.401 | 0.366 | 87.562 |
| 400.000 | 5.293 | 0.275 | 92.296 |
| 500.000 | 4.138 | 0.220 | 94.764 |

6.2 TNO Multi-energy Method

The TNO multi-energy method was used assuming a maximum charge strength and a total confined volume of 7800 m³ (52x50x3). The results are similar to those estimated using the TNT equivalence method although both methods differ fundamentally regarding the explosion mechanism. Overpressure vs. time loading on the front, side/roof, and rear walls of the building are shown graphically.



Impulse loading estimates using the TNO multi-energy method are also provided.

****BUILDING BLAST LOADING RESULTS**

| | |
|--------------------------------------|---------|
| Positive phase duration. s | 0.066 |
| Incident overpressure. kPa | 8.636 |
| Incident pressure. kPa | 109.961 |
| Front wall impulse. kPa.s | 0.592 |
| Side wall or roof impulse. kPa.s | 0.252 |
| Rear wall impulse. kPa.s | 0.286 |
| Air Cp/Cv ratio | 1.404 |
| Side wall Ce factor | 0.720 |
| Speed of sound in air. m/s | 346.402 |
| Shock velocity. m/s | 360.818 |
| Blast wind velocity. m/s | 22.303 |
| Blast wind dynamic overpressure. kPa | 0.295 |
| Blast wave length. m | 23.870 |

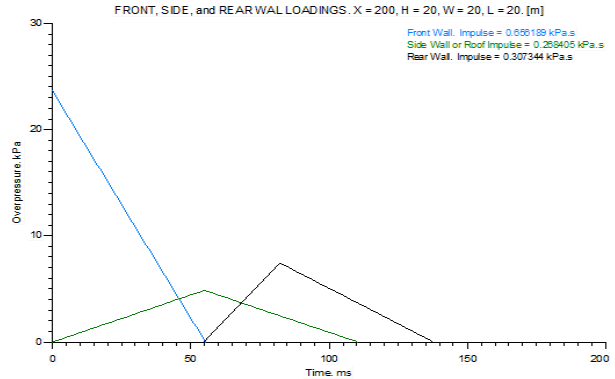
In addition to impulse tables and dynamic pressure profiles, SuperChems Expert™ provides overpressure and impulse information at user defined thresholds for the TNO Multi-energy method.

| Distance. m | Area. m2 | Overpressure. kPa | Impulse. kPa.s | Duration. ms |
|-------------|-----------|-------------------|----------------|--------------|
| 176.206 | 97541.379 | 10.000 | 0.313 | 62.679 |
| 107.190 | 36096.018 | 19.998 | 0.498 | 49.840 |
| 83.833 | 22079.091 | 29.997 | 0.666 | 44.381 |
| 71.381 | 16007.139 | 40.007 | 0.824 | 41.216 |
| 63.418 | 12635.153 | 49.993 | 0.978 | 39.112 |
| 57.781 | 10488.661 | 59.990 | 1.127 | 37.588 |
| 51.761 | 8416.798 | 74.988 | 1.348 | 35.940 |

| Radial distance. m | Overpressure. kPa | Impulse. kPa.s | Duration. ms |
|--------------------|-------------------|----------------|--------------|
| 10.000 | 2026.500 | 33.452 | 33.015 |
| 20.000 | 729.839 | 10.481 | 28.721 |
| 30.000 | 256.352 | 3.875 | 30.235 |
| 40.000 | 130.682 | 2.139 | 32.731 |
| 50.000 | 80.587 | 1.429 | 35.455 |
| 100.000 | 22.332 | 0.538 | 48.224 |
| 200.000 | 8.612 | 0.285 | 66.163 |
| 300.000 | 5.497 | 0.212 | 77.079 |
| 400.000 | 3.997 | 0.168 | 83.870 |
| 500.000 | 3.122 | 0.138 | 88.141 |

6.3 Baker-Strehlow Method

The Baker-Strehlow method was used assuming a stoichiometric mixture of butane-air (7,800 m³ or 650 kgs of butane), 2D flame geometry, high confinement level, and a medium chemical reactivity. The results are similar to those estimated using the TNT equivalence and TNO multi-energy methods. Overpressure vs. time loading on the front, side/roof, and rear walls of the building are shown graphically. The Baker-Strehlow method is widely used in the US.



Impulse loading estimates using the Baker-Strehlow method are also provided.

```

**BUILDING DATA
Distance from explosion. m           200.000
Building Height. m                   20.000
Building Width. m                    20.000
Building Length. m                   20.000

**BUILDING BLAST LOADING RESULTS

Positive phase duration. s           0.055
Incident overpressure. kPa           11.307
Incident pressure. kPa               112.632

Front wall impulse. kPa.s            0.656
Side wall or roof impulse. kPa.s     0.268
Rear wall impulse. kPa.s            0.307

Air Cp/Cv ratio                      1.404
Side wall Ce factor                  0.673
Speed of sound in air. m/s           346.402
Shock velocity. m/s                  364.572
Blast wind velocity. m/s             28.307
Blast wind dynamic overpressure. kPa 0.475
Blast wave length. m                 20.208
    
```

In addition to impulse tables and dynamic pressure profiles, SuperChems Expert™ provides overpressure and impulse information at user defined thresholds for the Baker-Strehlow method.

| Distance. m | Area. m2 | Overpressure. kPa | Impulse. kPa.s | Duration. ms |
|-------------|------------|-------------------|----------------|--------------|
| 221.860 | 154635.207 | 10.000 | 0.284 | 56.857 |
| 126.429 | 50216.008 | 20.000 | 0.482 | 48.204 |
| 91.186 | 26122.069 | 30.000 | 0.654 | 43.605 |
| 73.948 | 17178.988 | 40.000 | 0.810 | 40.500 |
| 64.953 | 13253.937 | 50.000 | 0.921 | 36.852 |
| 55.425 | 9650.883 | 60.000 | 1.071 | 35.687 |
| 48.781 | 7475.729 | 75.000 | 1.202 | 32.052 |

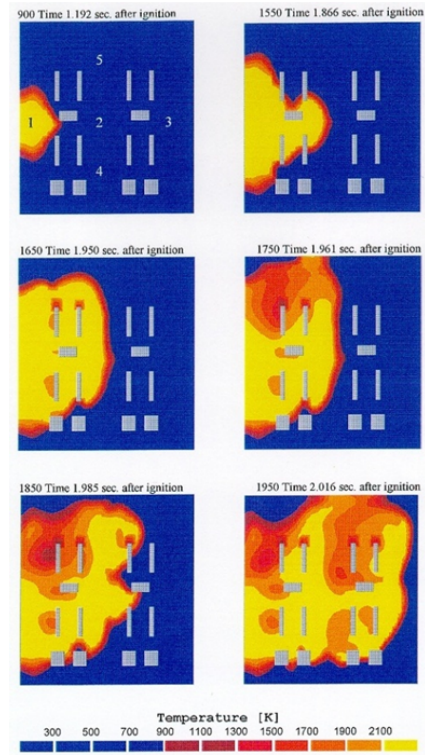
| Radial distance. m | Overpressure. kPa | Impulse. kPa.s | Duration. ms |
|--------------------|-------------------|----------------|--------------|
| 10.000 | 309.773 | 6.490 | 41.901 |
| 20.000 | 276.042 | 3.048 | 22.084 |
| 30.000 | 166.852 | 1.894 | 22.699 |
| 40.000 | 106.407 | 1.444 | 27.148 |
| 50.000 | 71.834 | 1.175 | 32.724 |
| 100.000 | 26.850 | 0.595 | 44.345 |
| 200.000 | 11.306 | 0.314 | 55.511 |
| 300.000 | 7.111 | 0.208 | 58.434 |
| 400.000 | 5.164 | 0.155 | 59.978 |
| 500.000 | 4.018 | 0.126 | 62.687 |

6.4 Computational Fluid Dynamics Method

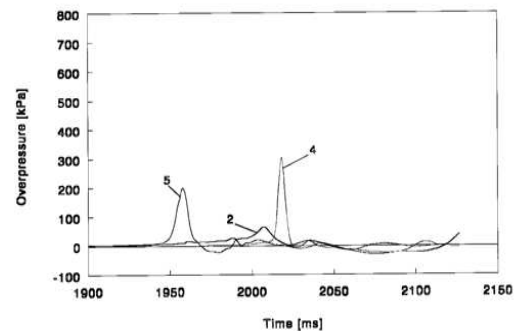
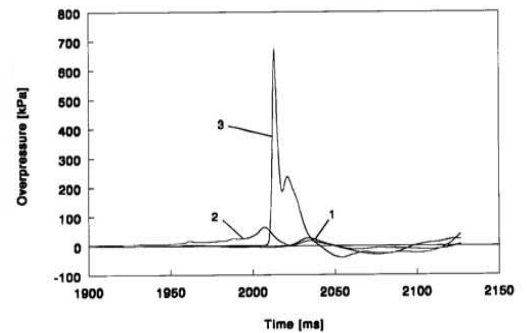
For critical infrastructure where the cost of building mitigation or relocation is excessive, more detailed explosion dynamics estimate can be used. 3D computational fluid dynamics (CFD) software such as AutoReaGas can be used. CFD explosion modeling is most useful in accident reconstruction and investigation.

The AutoReaGas estimate assumes a 10 kPa blast load with a 70 ms positive phase duration and is the most specific of the four methods outlined relative to this type of blast load.

CFD estimates provide insight into how the explosion develops over time, as well as the time histories of overpressure impact on buildings.



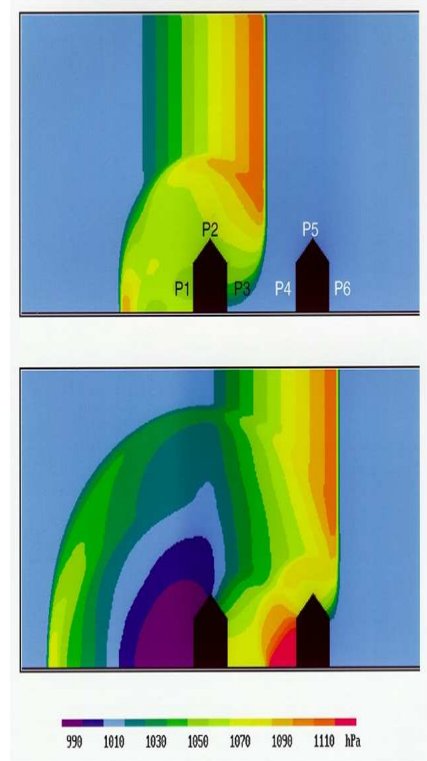
Note high pressures at locations 3, 4, and 5.
 Note two separate blasts near locations 3, 4, and 5
 Note low pressure at location 1



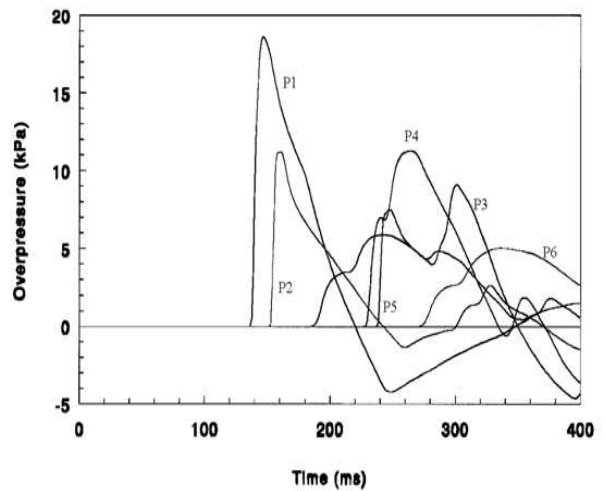
Detailed estimates of time histories of overpressure can be obtained. Also, the impact of building geometries and relative locations can be assessed.

For example, the first row of buildings exposed to overpressure might be subjected to higher reflected overpressure and more damage than the second row of buildings.

The AutoReaGas estimate assumes a 10 kPa blast load with a 70 ms positive phase duration. The time histories of overpressure can be used as input to structural dynamics codes to obtain more accurate estimates of potential bridling damage.



Note the reflected pressure of almost 20 kPa at the face of the building (x2).



7. Mitigation and Risk Reduction Measures

Explosion overpressure mitigation and risk reduction measures that can be implemented quickly include relocation of building occupants, provision of blast resistant modular buildings, windows hazard mitigation such as shatter proofing of glass, and securing of internal furniture and office equipment and fixtures. Longer term mitigation options include but are not limited to structural reinforcement, elimination of windows, construction of blast resistant external walls, etc.

Mitigation and risk reduction measures used for fire and toxicity risks include shelter in place and/or evacuation. Equipping buildings with instrumentation for the detection of flammable and/or toxic vapors, means to warn building occupants, and prevention of the ingress of smoke or hazardous fumes can reduce risks. Evacuation and/or shelter in place procedures must be developed, clearly communicated, and practiced regularly. Other common sense risk reduction measures include the provision of PPE for safe evacuation, provision of emergency communications equipment, designation of safe evacuation routes and assembly areas, implementation of proper head count procedures, etc.

8. Conclusions

Ultimately, facility siting is about risk reduction to occupants, infrastructure and physical assets, company reputation, and business interruption. Disciplined risk reduction requires a company to allocate resources and capital where portfolio risk is driven as low as reasonably practicable and where the most risk reduction is achieved per resource and capital allocation. That cannot be achieved without some understanding of likelihood of occurrence, even if semi-quantitative.

For companies that embrace QRA as a systematic method for risk evaluation and reduction, facility siting is simply a byproduct of a QRA study. For companies that do not, consequence-based facility siting may be the most practical approach but will not necessarily be the most optimal approach.

9. How can we help?

In addition to our deep experience in chemical reaction systems and the conduct of large-scale site wide relief systems evaluations by both static and dynamic methods, we understand the many non-technical and subtle aspects of compliance and legal requirements. When you work with ioMosaic you have a trusted partner that you can rely on for assistance and support with the lifecycle costs of relief systems to achieve optimal risk reduction and compliance that you can evergreen. We invite you to connect the dots with ioMosaic.

Figure 1.3: Connect the dots with ioMosaic



Appendices

Appendix A

Overview of Explosion Modeling for Facility Siting

An explosion is a fast energy-release process. Typical sources of explosion energy include:

- chemical,
- internal, and
- nuclear energy.

Chemical energy is usually associated with combustion or decomposition reaction for gases, liquids, dusts, and solids. High-pressure storage vessels containing gases or pressurized liquids possess significant amounts of internal energy which is released as pressure-volume or expansion energy following catastrophic vessel failure. Nuclear energy is associated with heats of reaction produced during fission or fusion.

Explosions can occur in a confined or partially confined containment, such as buildings or process vessels and pipings. Explosions that occur in the open as the result of a flammable cloud ignition are unconfined explosions.

For explosions where rapid combustion is the energy-release process, a given mass of fuel-oxidant has a fixed amount of chemical energy. This amount of energy is released at different rates depending on how fast combustion is proceeding. Once released, chemical energy is converted into internal energy. This usually yields an increase in both temperature and pressure. For an adiabatic, closed, constant-volume system, the final equilibrium state is independent of the rate of energy release, and is a function only of the total amount of energy released. Depending on how fast combustion is proceeding, i.e. flame speed, local overpressure is generated before reaching equilibrium conditions. A faster flame speed yields a faster local pressure rise and higher local overpressure. Flame speed is a key factor in the safety assessment of an explosion.

1. Deflagrations Vs. Detonations

Depending on the flame speed, explosions can be classified as deflagrations or detonations. Deflagrations are characterized by the release of thermal energy caused by subsonic combustion in the unburnt medium. Energy is released by a chemical reaction (combustion) initiated by heat transfer from the reaction zone to the unburnt material. Ignition energies required for initiation of deflagrations can be as small as 4 millijoules. A typical laminar burning velocity for hydrocarbon systems at 1 atm is about 0.3 m/s.

Detonations are characterized by a flame front traveling as a shock wave followed closely by a combustion wave. The flame front travels at sonic velocity in the burnt gases and at supersonic velocities in the unburnt gas medium. Energy is released by chemical reaction (combustion) initiated by compression of unburnt materials by the shock wave beyond their spontaneous ignition (autoignition) temperature. Deflagrations yield overpressures on the order of 8 to 10 times the initial pressure for most hydrocarbon-air mixtures. Higher overpressure have been observed in hydrocarbon-oxygen mixtures. Detonations yield overpressures on the order of 20 times the initial pressure. Typical detonations velocities are on the order of 2000 m/s. The peak pressure developed during a detonation can be estimated using the Chapman-Jouguet theory which combines thermodynamics and gas dynamics conservation equations across the detonation front.

Detonations can be produced by direct initiation or by deflagration which transit to detonations (DDT). The direct initiation of detonations requires a large amount of energy to deposited into the explosive medium in a very short time (on the order of microseconds). Existing low-pressure data indicate that the transition of a deflagration to a detonation is possible if:

- the deflagration is proceeding at a sufficiently large flame speed, i.e., 500 to 600 m/s;
- turbulence is enhanced by the presence of obstructions (grids, pipes, etc.), strong turbulent jets, confinement, or a long tube; and
- the detonation cell size is smaller than the minimum transverse dimension of the obstacles or tube.

There is a fundamental difference between deflagrations and detonations in enclosures. Since flames propagate at sub-sonic velocities in a deflagration, the resulting pressure increase during a deflagration occurs almost uniformly throughout the enclosure. Pressure pileup is possible when an explosion occurs in an enclosure or vessel that is connected to another enclosure or vessel. The pressure increase caused by a detonation occurs almost instantaneously and is highly nonuniform. This implies that explosion venting and suppression is not practical for detonations and structural loading caused by detonations require special consideration in estimating structural response and resistance.

2. Damage From Explosions

Hazards associated with explosions are classified as:

- overpressure (blast effects),
- cratering,
- ground shock,
- projectiles (missiles), and
- radiant thermal heat (fireballs).

Structural damage caused by overpressure involves:

- estimation of pressure-time profiles caused by the explosion,
- characterization of structural loading mechanisms,
- establishment of a structure failure criterion, and
- calculation of structural response.

Pressure-time histories caused by explosions may be non-uniform and subject to amplification because of secondary shocks and shock reflections. Current models can provide only one/two-dimensional histories at present. Failure modes are typically classified as:

- permanent deformation (plastic deformation/buckling),
- stable cracking (leak), and
- brittle fracture.

A failure criterion often used in the process industry is to use as allowable stress the value of dynamic yield strength instead of allowable stress values which tend to incorporate large safety factors on the ultimate and yield strength of construction material. The dynamic yield strength is approximately 1.33 times the static yield strength.

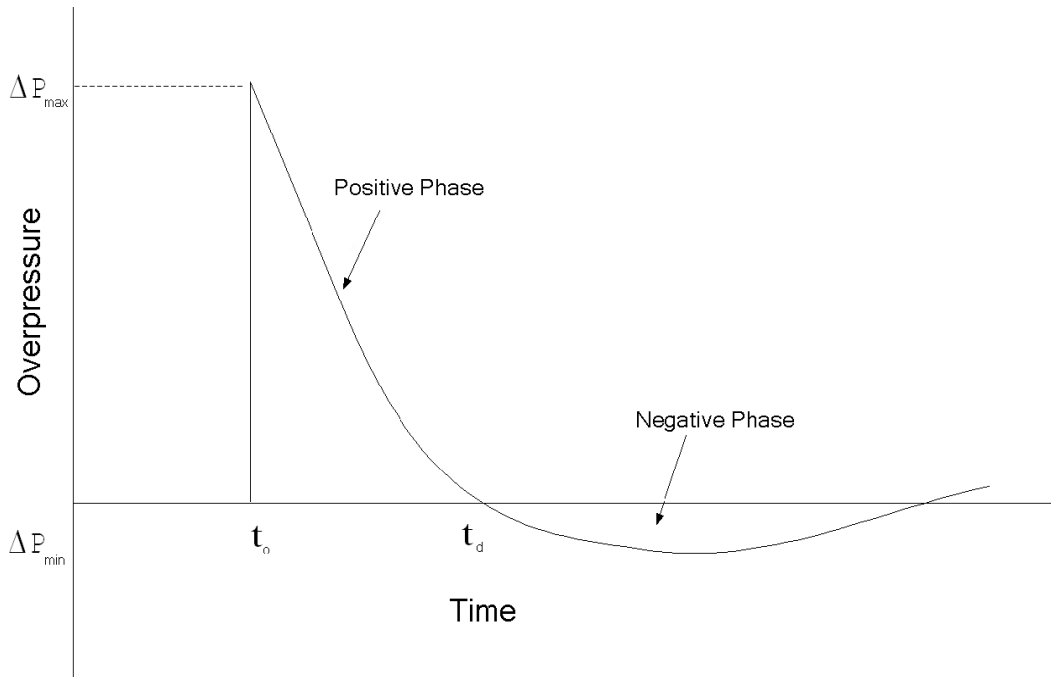
3. Blast Waves

From a damage view point, the most important consequence of a vapor cloud explosion is the development of a blast wave. Close to the center of the explosion, and particularly within the flammable vapor cloud, the deflagration will produce damage from the flame itself in addition to the blast overpressure; outside of this region, however, the effects of the blast wave will be the most damaging.

The blast wave produced by an explosion is termed a free-field blast wave, or free-field overpressure wave, until it interacts with objects or structures in its path. The blast wave from a catastrophic high pressure vessel burst and/or detonation - such as from *TNT* or other condensed phase explosions - has a very steep rise in pressure, to its maximum value (peak overpressure), followed by

an exponential-like decay to ambient pressure followed by a negative pressure phase to a negative pressure peak much smaller than the positive peak. An idealized time-history of a typical shock wave is illustrated in Figures A.1 and A.2.

Figure A.1: A Typical Condensed Phase Explosion or Vessel Burst Pressure History (Shock Wave)



During the positive phase duration, the pressure-history shown in Figure A.1 is often represented using a modified Friedlander equation:

$$\Delta P(t) = \Delta P_{max} \left(1 - \frac{t}{t_d}\right) \exp\left(-b \frac{t}{t_d}\right) \quad (\text{A.1})$$

where b is the waveform parameter, t is time, and t_d is the positive phase duration (assuming $t_o = 0$). The overpressure impulse can then be calculated by integrating the Friedlander equation:

$$I = \int_0^{t_d} \Delta P(t) dt = \frac{\Delta P_{max} t_d}{b^2} [b - 1 + \exp(-b)] \quad (\text{A.2})$$

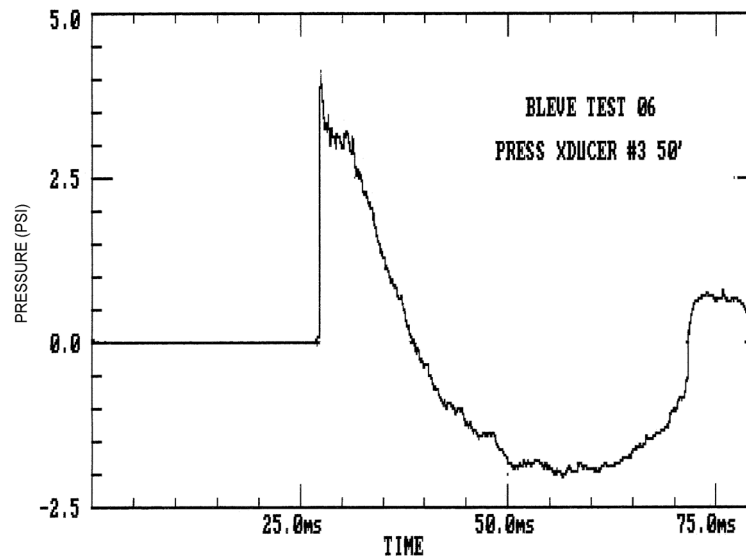
Typically reasonable values of ΔP_{max} , t_d , and I can be obtained from explosion models such as the TNT equivalence model. If the Friedlander equation is used to represent the time dependent decay of the the overpressure and impulse, the value of b has to be determined by solving Equation A.2 for b . The negative phase parameters are not as well understood as those for the positive phase. For these types of explosions δP_{min} is typically approximated as $\frac{1}{8} \Delta P_{max}$ and t_d^- is approximated as $\frac{1}{4} t_d$. Rigby et al. [7, 8] published and validated very useful guidance on how to estimate the negative phase impulse, peak underpressure, and duration. Their validation study shows that the cubic negative phase form discussed earlier produced high quality predictions when compared to their actual test data:

$$\Delta P(t) = \Delta P_{min} \frac{27}{4} \left(\frac{t}{t_d^-} \right) \left(1 - \frac{t}{t_d^-} \right)^2 \quad (\text{A.3})$$

Integration of Equation B.16 yield the following expression for negative phase impulse:

$$I^- = \frac{9}{16} \Delta P_{min} t_d^- \quad (\text{A.4})$$

Figure A.2: Measured Catastrophic Vessel Burst with BLEVE/UVCE Pressure History from Melhem [9]

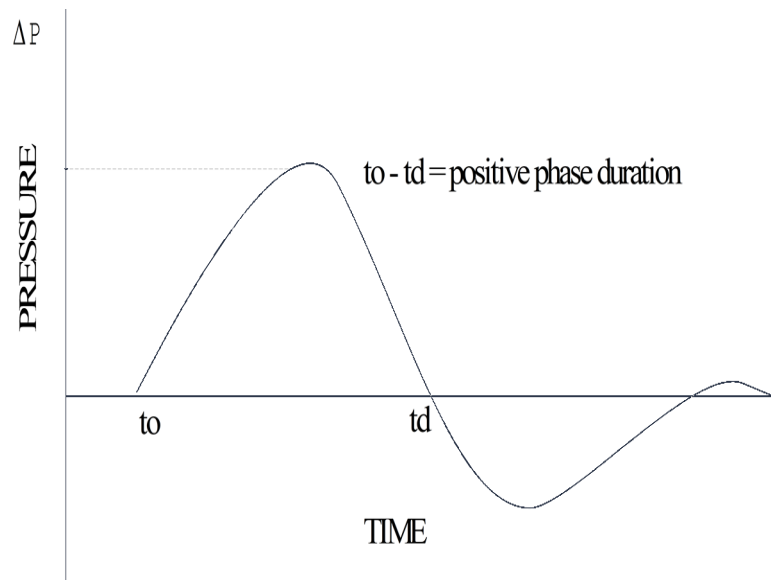


Shocks are not produced for slow vapor cloud deflagrations (flame speed less than 45 m/s) or vessel failures/bursts. In these cases the negative phase duration can be large and sometimes larger than the positive phase duration. This is well illustrated in Figure A.2 involving the actual failure of a 500 gallon propane tank. A second pressure wave is often observed after the negative phase duration as also shown in Figure A.2 for vessel failures when followed by flashing and/or a deflagration due to combustion.

The time-history of the blast wave from a vapor cloud explosion is not known. Based on theoretical studies on deflagrations, and on the characteristics of the accelerating flame front within the ignited cloud, it is generally agreed that the shape of the pressure wave is different from a shock wave. A commonly-held concept is that the pressure wave for these events consists of a slow rise, up to a peak overpressure, and a decay to ambient, followed by a negative phase to a negative pressure peak somewhat smaller than the positive peak. As shown in Figure A.3, this blast wave time-history appears more like a damped one-cycle sine wave.

The duration of the positive phase of an UVCE at a given level of overpressure, which is of interest in damage prediction, is thought by some investigators to be larger than that from a condensed phase explosion of equal yield. Note, however, that in the absence of more information, the HSE

Figure A.3: A Typical Deflagration Explosion Pressure History (Pressure Wave)



(Second Report) suggests that an estimate of 30 msec be used for vapor cloud explosions, independent of overpressure level. Although this may be a reasonable estimate at the edge of the cloud, in the vicinity of peak overpressure levels of 10 psi, it is likely to underestimate the duration at greater distances, since it is well established, for condensed phase explosives, that the duration increases (the overpressure time-history stretches out) as the peak overpressure decreases. The duration of the positive phase for condensed phase explosions increases by a factor of almost four as the peak overpressure decreases from 10 psi to 1 psi.

The most important characteristic of the blast wave is its peak overpressure level. Most damage studies and analysis correlate the extent of damage to the value of the peak overpressure of the free-field blast wave, even though it is recognized that the impulse of the blast wave can be of more significance for assessment to damage to some types of structures.

The impulse of an explosion is calculated by integrating the explosion overpressure over the positive phase duration of the explosion.

$$I = \int_0^{t_d} (P(t) - P_a) dt \quad (\text{A.5})$$

For a triangular overpressure pulse, I can be approximated as $I \simeq \frac{1}{2} \Delta P_o t_d$.

4. Blast Loading Mechanisms

Blast forces of interest in facility siting studies can be significantly larger than the live and dead loads often utilized in conventional engineering design practice. These loadings are in many cases transient and have a small probability of occurrence. Therefore, a structural dynamics estimate

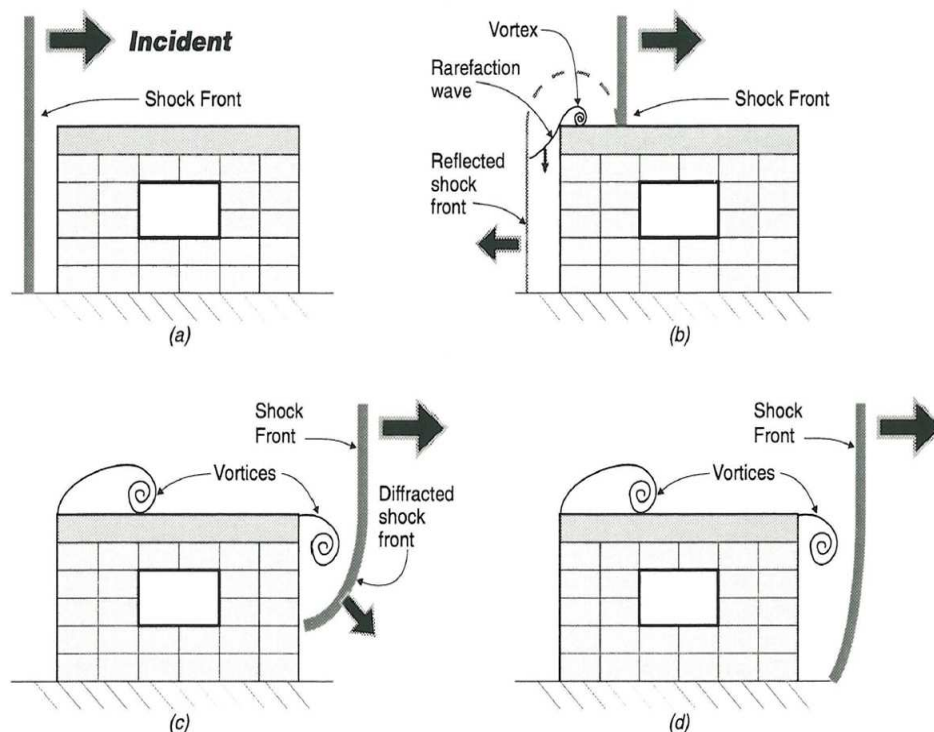
conducted using a single degree of freedom (SDOF) is typically sufficient. In addition, the adequacy of the structural design to blast loadings can be credibly assessed by some form of limit design criteria (for example, allowable stress value equals the dynamic yield strength of the structural material, generally taken to be equal to 1.33 times the static yield strength).

The loading patterns which develop on many types of conventional structures as a result of explosions can be broadly categorized into diffraction-type loadings and drag-type loadings.

4.1 Diffraction Loading

Diffraction loading forces on a structure result from the direct and reflected pressures associated with the air blast during the initial phases of the envelopment of the structure. As the blast wave traverses the structure, the pressure wave bends or "diffracts" around the structure such that the structure is eventually engulfed by the blast. When the diffraction process is complete, the structure is immersed in a pressure field with approximately equal pressure levels on all the elements of the structure (see Figure A.4, a - shock wave approaches structure, b- shock reflects from front surface and diffracts over structure, c- diffraction continues across rear surface, and d- diffraction is complete as shock front passes beyond the structure).

Figure A.4: Blast wave interaction with a rectangular building



When the leading edge of a blast wave strikes the surface of a structure the motion of the wave is momentarily stopped, i.e. the flow is arrested. The pressure on the surface of the structure builds up very rapidly to a pressure often called the peak reflected pressure. The peak reflected pressure

can be much larger than the "incident peak pressure" or "side-on pressure". This amplification will depend on the angle at which the blast wave strikes the structure, the shape of the structure and the absolute value of the incident peak pressure.

The side-on pressure is measured perpendicular to propagation direction of the wave. Side-on pressure is the static pressure behind the shock wave. The reflected pressure is measured when the wave hits an object like a wall head-on. Stagnation pressure is the pressure that a moving fluid would have if it was brought to rest. The stagnation pressure is the sum of the static and the dynamic pressures.

$$P_{dynamic} = \frac{1}{2}\rho u^2 \quad (A.6)$$

$$P_{stagnation} = P_{static} + P_{dynamic} \quad (A.7)$$

The difference in pressure between the front and rear walls of the structure gives rise to a force imbalance which tries to move the structure in the direction of travel of the blast wave. As the pressure wave bends around the structure it creates a crushing force. These translational and crushing forces taken together create a loading on the structure known as "diffraction loading". The local and differential forces acting on the structure during the period of time before envelopment is complete (i. e., during the time that a net pressure field exists) is defined as the diffraction loading.

The duration of the diffraction loading is typically very short; as the blast wave flows around the edges of the structure, the pressure on the front surface is relieved and drops rapidly to a level known as the stagnation pressure, which is the sum of the residual overpressure from the blast wave and the pressure exerted by the flowing "blast wind". The duration of the time that a diffraction load is imposed depends upon the shock velocity of propagation and the geometry and dimensions of the structure.

The "clearing time" t_c required before the reflected pressure levels are reduced to stagnation pressures levels is estimated from the dimensions of the structure and the shock velocity. For a rectangular structure, t_c is calculated as:

$$t_c = 3 \frac{\min\left(H, \frac{B}{2}\right)}{u_{shock}} \quad (A.8)$$

where H is the height of the structure, B is the width of the structure, and u_{shock} is the shock front velocity defined in Equation A.12.

The time-history of the loading on the top, sides and back wall of a rectangular structure will also depend on the length of the structure. For each of these surfaces, pressure-time histories can be developed; and net loadings then obtained for the translational forces.

The shock front velocity can be calculated from fluid flow equations developed earlier in this book:

$$P_o = \Delta P_o + P_a \quad (\text{A.9})$$

$$u_{shock} = u_a + u_{sonic,a} \sqrt{\frac{\gamma_a + 1}{2\gamma_a} \frac{P_o}{P_a} + \frac{\gamma_a - 1}{2\gamma_a}} \quad (\text{A.10})$$

$$= u_a + \sqrt{\frac{\gamma_a R_g T_a}{M_{w,a}}} \sqrt{\frac{\gamma_a + 1}{2\gamma_a} \frac{P_o}{P_a} + \frac{\gamma_a - 1}{2\gamma_a}} \quad (\text{A.11})$$

$$= u_a + 345.92 \sqrt{0.857 \frac{P_o}{P_a} + 0.142} \quad (\text{A.12})$$

where P_o is the peak side-on or incident pressure of the blast wave, u_a is the ambient wind speed, $u_{sonic,a}$ is the speed of sound in air, and γ_a is the heat capacity ratio of air which is equal to 1.4 at 1 bara and 298.15 K.

At any time, the propagating blast wave (as the shock/pressure front travels outward from the explosion) extends over a limited radial distance. The pressure is largest at the front and decreases to ambient pressure over a distance, L_w , called the blast wave length. Values of L_w for high energy explosives can be obtained from reference [10]:

$$L_w = 230 \text{ ft} \sqrt{\frac{100}{\Delta P_o \text{ psi}}} \left[\frac{W_{TNT}}{1MT} \right]^{\frac{1}{3}} \quad (\text{A.13})$$

$$W_{TNT} = \frac{\text{Explosion Energy in kJ}}{10^9 \times 1155 \times 4.184} \quad (\text{A.14})$$

$$1MT = 1 \text{ Mega Ton of TNT} \quad (\text{A.15})$$

where W_{TNT} is the explosion energy expressed in megatons of TNT. In the low pressure range, L_w can be approximated by (see [11]):

$$L_w = u_{shock} t_d \quad (\text{A.16})$$

4.2 Drag Loading

The drag loading is produced by the strong transient winds behind the shock front. Like the diffraction loading, the drag loading is equivalent to translational force acting upon the structure. The duration of the drag loading, however, is equal (approximately) to the duration of the positive phase of the air blast wave and is not a time function of the dimensions of the structure.

The blast wind, which is created by and travels behind the blast wave, gives rise to a "dynamic pressure" which exerts a "drag loading" on the structure. The extent of any structural damage caused by diffraction and drag loading will vary with building design. Buildings of curtain-wall construction (i.e. buildings which incorporate areas of cladding on external panels which are not load bearing the cladding may consist of such materials as glass, plastics or sheet metal) will be more easily damaged than traditional brick-built buildings.

Steel-framed buildings may simply flex in the blast wave and, for a given level of loading, sustain less damage than buildings of traditional construction. Once a building has been breached by a blast wave, the flowing blast wind may do considerable damage on washing through the in-between spaces in the building. The extent of the damage caused by this effect could again be dependent on building design. The level of loading itself can be significantly influenced by local topographical features, for example, blast waves may be reflected from adjacent buildings or even adjacent parts of the same structure.

The velocity of the blast wind can also be calculated from fluid flow equations developed earlier in this book:

$$u_{bw} = u_a + u_{sonic,a} \left(\frac{P_o}{P_a} - 1 \right) \sqrt{\frac{2}{\gamma_a(\gamma_a - 1)} \left(\frac{\gamma_a + 1}{\gamma_a - 1} \frac{P_o}{P_a} + 1 \right)^{-1}} \quad (\text{A.17})$$

$$u_{bw} = u_a + 345.92 \sqrt{\frac{3.571}{6 \frac{P_o}{P_a} + 1}} \quad (\text{A.18})$$

The dynamic pressure, q is then calculated from the density of air behind the blast wave and the square of the velocity of the blast wind:

$$q_o = \frac{1}{2} \rho_a u_{bw}^2 = 0.5927 u_{bw}^2 \quad (\text{A.19})$$

Table A.1 shows typical values of shock and blast wind velocities at different levels of overpressure assuming an ambient wind speed of zero, and ambient temperature of 298.15 K and an ambient pressure of 1 bara. Newmark [12] provides a simpler equation for q_o which relates the dynamic pressure to side-on overpressure:

$$q_o = \left(\frac{5}{2} \right) \frac{\Delta P_o^2}{7 P_a + \Delta P_o} \quad (\text{A.20})$$

The net dynamic pressure on a structure is the product of the dynamic pressure and a drag coefficient, C_d . The drag coefficient depends on the shape and orientation of the obstructing surface. For a rectangular building, the drag coefficient may be taken as +1.0 for the front wall, and -0.4 for the side and rear walls, and roof. The dynamic pressure exerts the dominant blast effect on open frame structures, framed structures with frangible cladding, and on small structures or components such as poles, stacks, etc. The dynamic pressure also influences, but to a lesser extent, the net blast loads on the walls and roof of an enclosed building.

4.3 Peak Reflected Pressure Ratios

The magnitude of the reflected pressure is usually determined as an amplifying ratio of the peak incident or side-on pressure. This factor is typically equal to 2. Note that many explosion models already account for initial overpressure reflection by multiplying the explosion energy level by 2

Table A.1: Typical values of shock front and blast wind velocities from Equations A.12 and A.18

| $P_o - P_a$, psi | $P_o - P_a$, Pa | $P_o - P_a$, bara | P_o/P_a | u_{shock} , m/s | u_{bw} , m/s | q , Pa | q , bara |
|-------------------|------------------|--------------------|-----------|-------------------|----------------|----------|------------|
| 0.5 | 3448 | 0.03 | 1.034 | 350.82 | 8.40 | 42 | 0.000 |
| 1 | 6897 | 0.07 | 1.069 | 355.83 | 16.56 | 162 | 0.002 |
| 2 | 13793 | 0.14 | 1.138 | 365.63 | 32.23 | 616 | 0.006 |
| 3 | 20690 | 0.21 | 1.207 | 375.18 | 47.11 | 1315 | 0.013 |
| 4 | 27586 | 0.28 | 1.276 | 384.49 | 61.29 | 2227 | 0.022 |
| 5 | 34483 | 0.34 | 1.345 | 393.58 | 74.85 | 3321 | 0.033 |
| 6 | 41379 | 0.41 | 1.414 | 402.46 | 87.84 | 4573 | 0.046 |
| 7 | 48276 | 0.48 | 1.483 | 411.15 | 100.31 | 5964 | 0.060 |
| 8 | 55172 | 0.55 | 1.552 | 419.67 | 112.32 | 7477 | 0.075 |
| 9 | 62069 | 0.62 | 1.621 | 428.01 | 123.90 | 9098 | 0.091 |
| 10 | 68966 | 0.69 | 1.690 | 436.19 | 135.08 | 10815 | 0.108 |
| 11 | 75862 | 0.76 | 1.759 | 444.23 | 145.91 | 12618 | 0.126 |
| 12 | 82759 | 0.83 | 1.828 | 452.12 | 156.39 | 14497 | 0.145 |
| 13 | 89655 | 0.90 | 1.897 | 459.87 | 166.57 | 16445 | 0.164 |
| 14 | 96552 | 0.97 | 1.966 | 467.50 | 176.46 | 18455 | 0.185 |
| 15 | 103448 | 1.03 | 2.034 | 475.00 | 186.08 | 20522 | 0.205 |
| 30 | 206897 | 2.07 | 3.069 | 575.94 | 306.95 | 55843 | 0.558 |
| 45 | 310345 | 3.10 | 4.103 | 661.66 | 400.79 | 95208 | 0.952 |
| 50 | 344828 | 3.45 | 4.448 | 687.87 | 428.36 | 108758 | 1.088 |
| 100 | 689655 | 6.90 | 7.897 | 909.27 | 648.15 | 248989 | 2.490 |
| 150 | 1034483 | 10.34 | 11.345 | 1086.46 | 813.68 | 392410 | 3.924 |
| 200 | 1379310 | 13.79 | 14.793 | 1238.55 | 951.69 | 536814 | 5.368 |
| 250 | 1724138 | 17.24 | 18.241 | 1373.91 | 1072.42 | 681650 | 6.816 |
| 300 | 2068966 | 20.69 | 21.690 | 1497.08 | 1181.03 | 826712 | 8.267 |

if the source is close to ground or a reflecting surface. The peak reflected pressure for a normally incident shock wave is given by:

$$\frac{\Delta P_{r,o}}{P_a} = 2 \frac{\Delta P_o}{P_a} + \frac{(\gamma + 1) \left(\frac{\Delta P_o}{P_a} \right)^2}{(\gamma - 1) \left(\frac{\Delta P_o}{P_a} \right) + 2\gamma} \quad (\text{A.21})$$

Equation A.21 is based on the Rankine-Hugoniot equation derived for an ideal gas (see [12]). At pressures less than 60 psi, a simpler expression is proposed by Newmark [12]:

$$\frac{\Delta P_{r,o}}{\Delta P_o} = 2 + 6 \frac{dP_o}{7P_a + dP_o} \quad (\text{A.22})$$

For peak pressures up to 20 psi, we can further simplify the equation to:

$$\frac{\Delta P_{r,o}}{\Delta P_o} = C_r = 2 + 0.73 \Delta P_o \quad (\text{A.23})$$

Figure A.5: Blast wave reflection coefficient for a shock

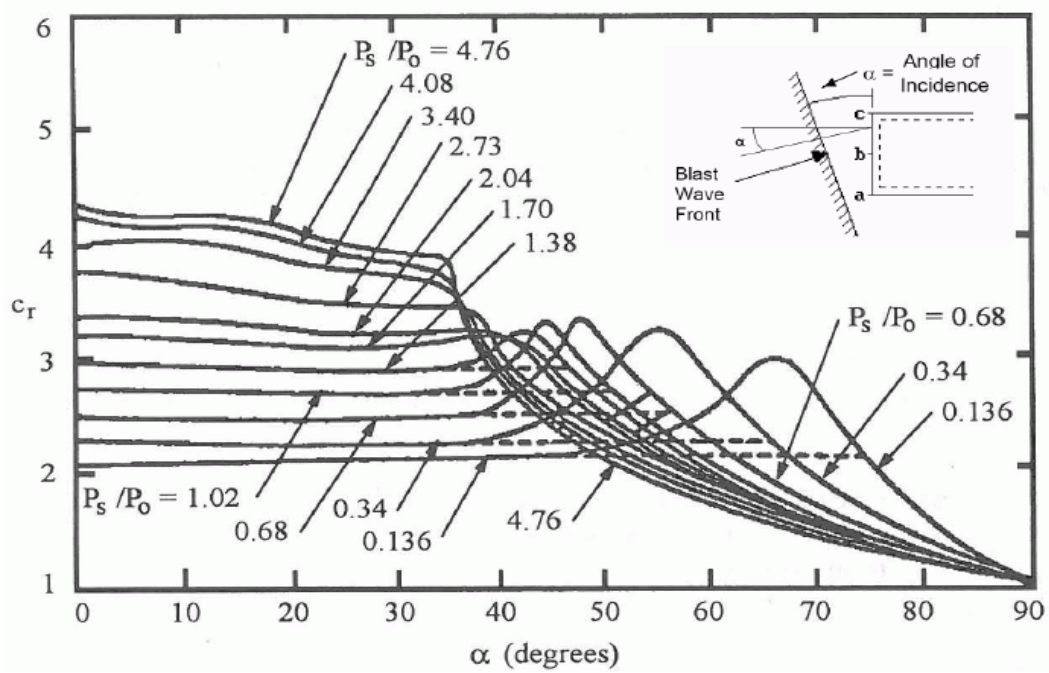
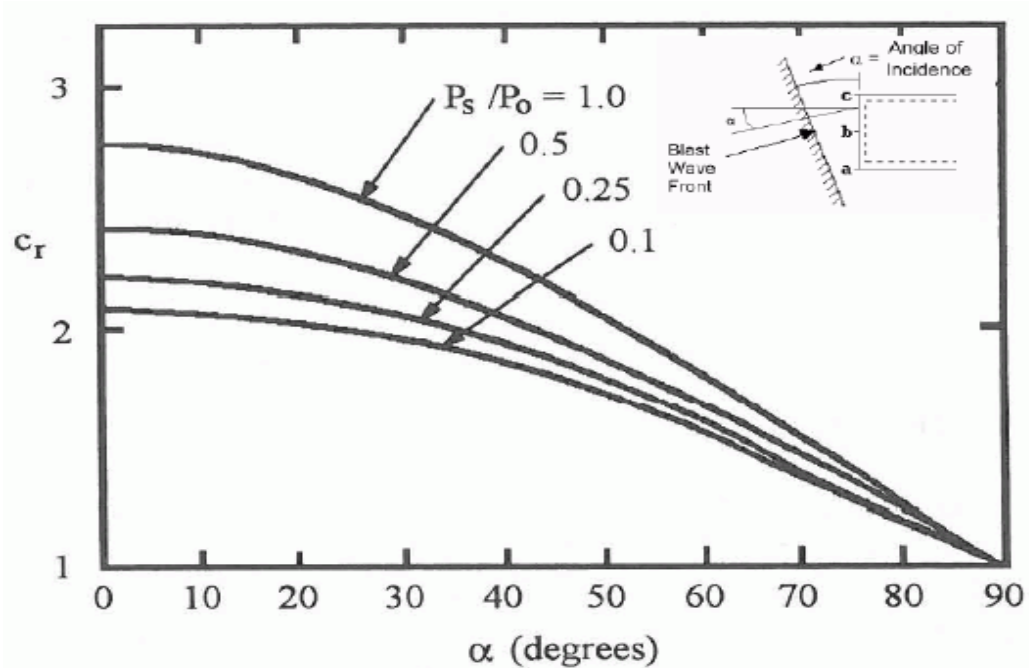


Figure A.6: Blast wave reflection coefficient for a pressure wave



As mentioned earlier, the reflection coefficient, C_r , depends on the peak overpressure, the angle of incidence of the wave front relative to the reflecting surface, and on the type of blast wave. The curves in Figures A.5 and A.6 show reflection coefficients for shock waves and pressure waves, for angles of incidence varying from zero degrees (wave front parallel to surface) to ninety degrees (wave front perpendicular to surface), and for peak overpressures up to five times atmospheric pressure.

The duration of the reflected pressure depends on the dimensions of the reflecting surface, up to a maximum time approximately equal to the positive phase duration of the incident blast wave. This upper limit corresponds to the total reflection of the entire blast wave without any diffraction around the edges of the reflecting surface.

5. Building Blast Loading

The interaction of blast waves with plant structures and buildings is a complex process. There are a multitude of scenarios in a typical chemical processing plant that can lead to loss of containment, subsequent dispersion, and ignition leading to an explosion. These scenarios can range from a small leak to a catastrophic vessel failure. The severity of the resulting explosion is influenced by the chemical reactivity, release phase and conditions, confinement and release geometry, atmospheric wind speed and stability, etc. Because of all the uncertainties associated with modeling the release and explosion process, we often make simplifying but prudent assumptions when developing the pressure-time histories used for building blast loading.

5.1 Front Wall Loading

The walls facing the explosion source will experience a reflected overpressure. The reflected overpressure magnitude will depend on the angle of incidence and on the rise-time of the side-on overpressure. It is typically assumed that the shock will strike the building face head on and that the pressure rise time is instantaneous. Note that in some cases oblique reflection (from 30 to 60 degrees) may be more important to the overall building because the full reflected overpressure could load two adjacent sides of the building. The reflected overpressure decays to the stagnation pressure, ΔP_s in the clearing time, t_c :

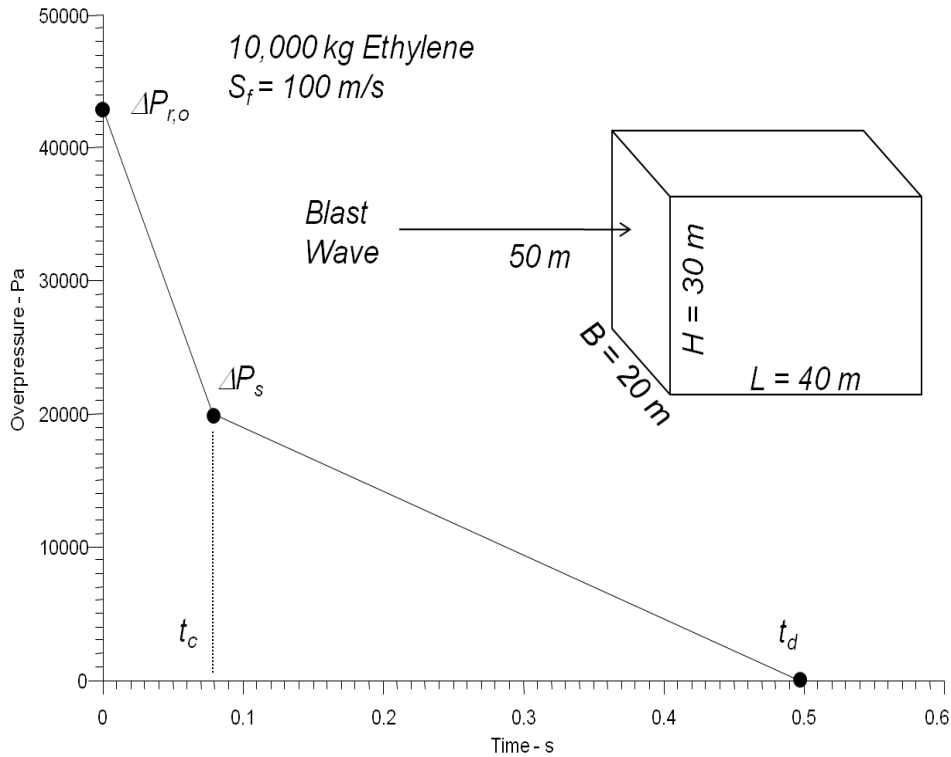
$$\Delta P_s = \Delta P_o + C_d q_o \quad (\text{A.24})$$

where t_c and q_o are defined by Equations A.8 and A.19. The associated impulse is then calculated from:

$$I \simeq \frac{1}{2} (\Delta P_{r,o} - \Delta P_s) t_c + \frac{1}{2} \Delta P_s t_d \quad (\text{A.25})$$

Figure A.7 illustrates the front wall loading history obtained from SuperChems Expert for a 10,000 kgs ethylene explosion with a flame speed of 100 m/s using the Baker-Strehlow explosion model. Note that the rectangular building is situated 50 meters away from the explosion. The calculated dynamic pressure from the blast wind is 1287 Pascals.

Figure A.7: An Example of Front Wall Loading



5.2 Side Walls and Roof Loading

Side walls will typically experience less overpressure loading than the front wall. This is caused by lack of overpressure reflection and by attenuation of the blast wave with distance from the explosion source. As a blast wave travels along the length of a structural element, the peak side-on overpressure will not be applied uniformly. It varies with both time and distance. If the length of the side wall (L) equals the length of the blast wave (L_w) when the peak side-on overpressure reaches the far end of the wall, the overpressure at the near end has already returned to ambient.

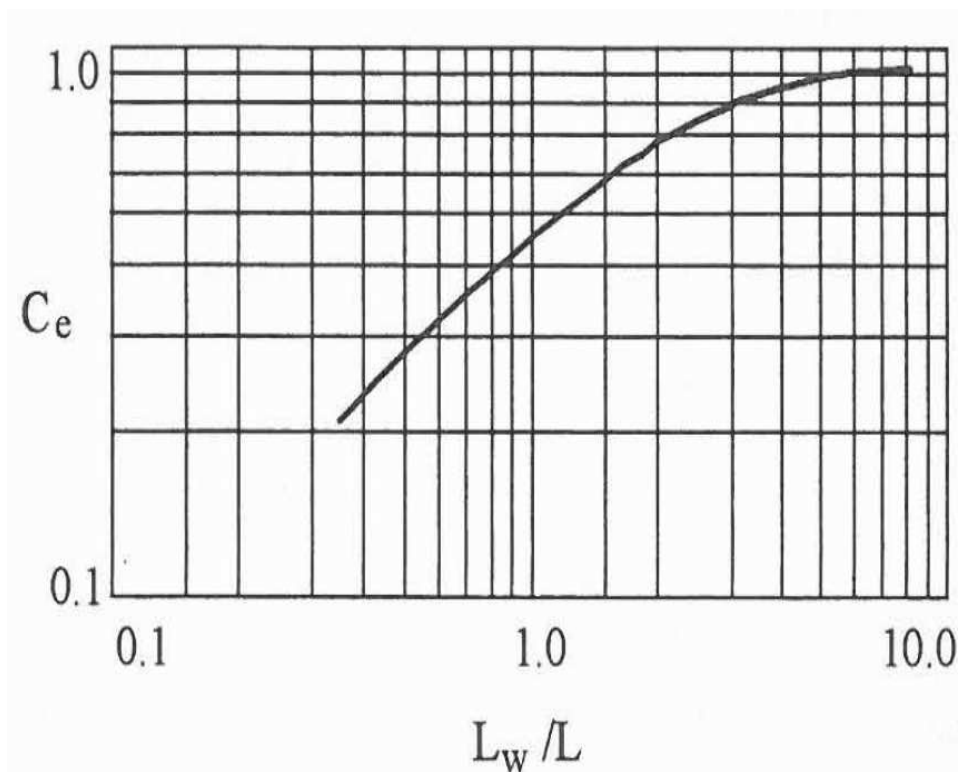
A reduction factor, C_e , is used to account for this effect in the evaluation of the building. Values for C_e are dependent on the length of the structural element, L , in the direction of the traveling blast wave. If the blast wave is traveling perpendicular to the span, then L should be equal to a nominal unit width of the element.

$$\Delta P_s = C_e \Delta P_o + C_d q_o \tag{A.26}$$

where C_d is the drag coefficient and is equal to -0.4 for q_o values between 0 and 25 psi, -0.3 for $25 < q_o < 50$ psi and -0.2 for $50 < q_o < 130$. C_e is estimated from Figure A.8.

The side wall load has a rise time, t_r , equal to the time it takes for the blast wave to travel across the element being considered. The overall duration is equal to this rise time plus the duration of

Figure A.8: Effective Overpressure Values for Side Walls Loading



the free-field side-on overpressure:

$$t_r = \frac{L}{u_{shock}} \quad (\text{A.27})$$

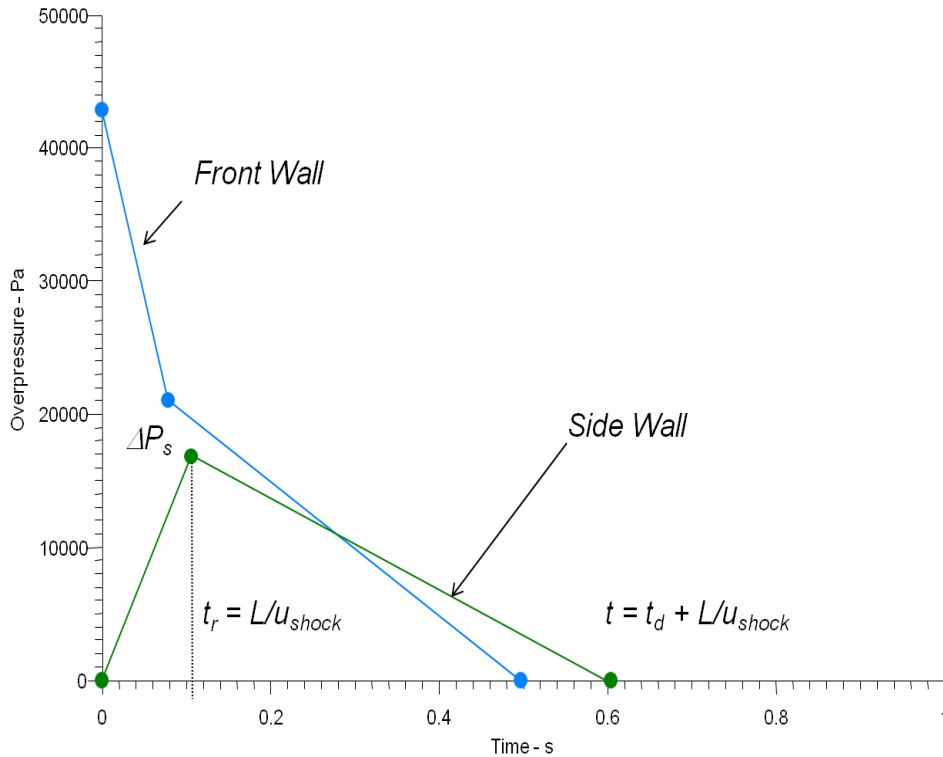
$$t = t_r + t_d = \frac{L}{u_{shock}} \quad (\text{A.28})$$

For buildings with flat roofs (pitch less than 10 degrees) it is normally assumed that reflection does not occur when the blast wave travels horizontally. A building roof will then experience the same side-on overpressure combined with the dynamic wind pressure as a side wall.

The dynamic wind force on the roof acts in the opposite direction to the overpressure (upward). Note that the blast wave will change with distance and time as it travels across a roof element. The resulting roof loading depends on the ratio of blast wave length to the span of the roof element and on its orientation relative to the direction of the blast wave. The effective peak overpressure for the roof elements are calculated in a similar fashion to the side wall.

The side wall loading for the ethylene explosion considered earlier is shown in Figure A.9. This profile was also calculated by SuperChems Expert using the Baker-Strehlow explosion model.

Figure A.9: An Example of Side Wall and/or Roof Loading



5.3 Rear Wall Loading

Rear wall loads can be conservatively neglected since a rear wall load is opposite in direction to the front wall load. Including the rear wall load in the analysis will reduce the overall building lateral blast force. Rear wall loading is normally used only to determine the net overall frame loading. The shape of the rear wall loading is similar to that for side and roof loads.

The rise time and duration are not well understood and are influenced by a pressure/shock wave spillover from the roof and side walls and from ground reflection effects.

The rear wall blast load lags that for the front wall by L/u_{shock} , the time required for the blast wave to travel the length, L , of the building. The effective peak overpressure is similar to that for side walls and is calculated using Equation A.26:

$$\Delta P_s = C_e \Delta P_o + C_d q_o \tag{A.29}$$

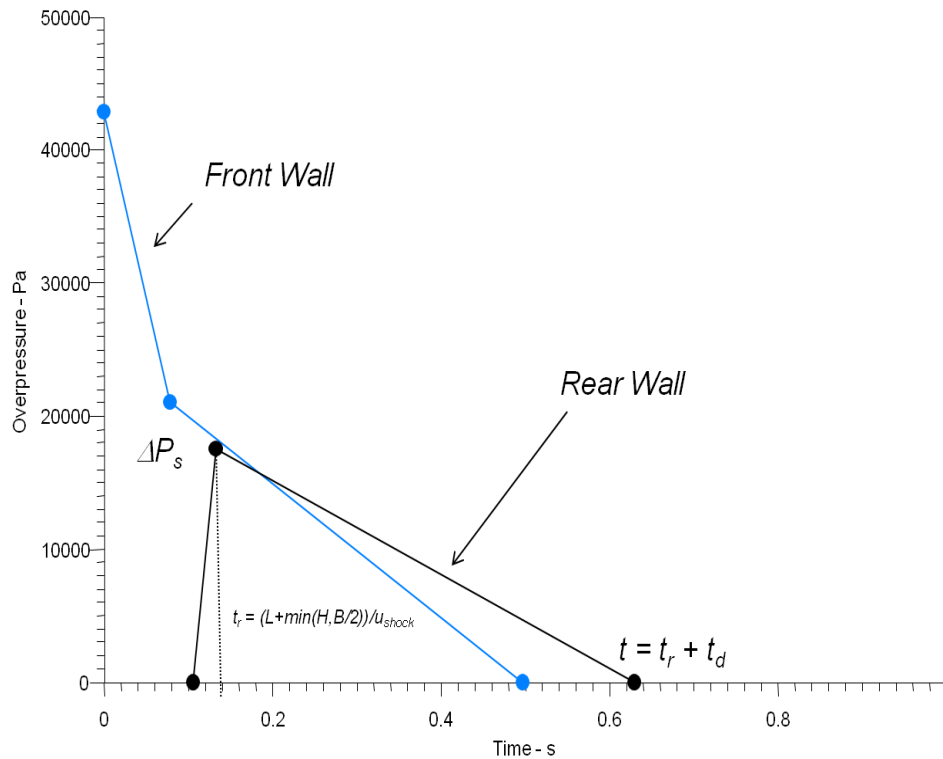
The rise time for the rear-wall load is calculated using the following equation:

$$t_r = \frac{L}{u_{shock}} + \frac{\min(H, B/2)}{u_{shock}} \tag{A.30}$$

The overall duration is equal to the rise time plus the positive phase duration:

$$t = t_r + t_d = \frac{L}{u_{shock}} + \frac{\min(H, B/2)}{u_{shock}} + t_d \tag{A.31}$$

Figure A.10: An Example of Side Wall and/or Roof Loading



The rear wall loading for the ethylene explosion considered earlier is shown in Figure A.10. This profile was also calculated by SuperChems Expert using the Baker-Strehlow explosion model.

5.4 Frame Loading

In addition to the roof loading, the framing system for the building will experience the diffraction loading which is the net loading on the front and rear walls taking into account the time phasing. During the time, L/u_{shock} , that it takes the blast wave to travel from the front to the back of the building the structural framing will be subjected to the large horizontal unbalanced pressure on the front wall. After that time the front wall loading is partially offset by the rear wall loading.

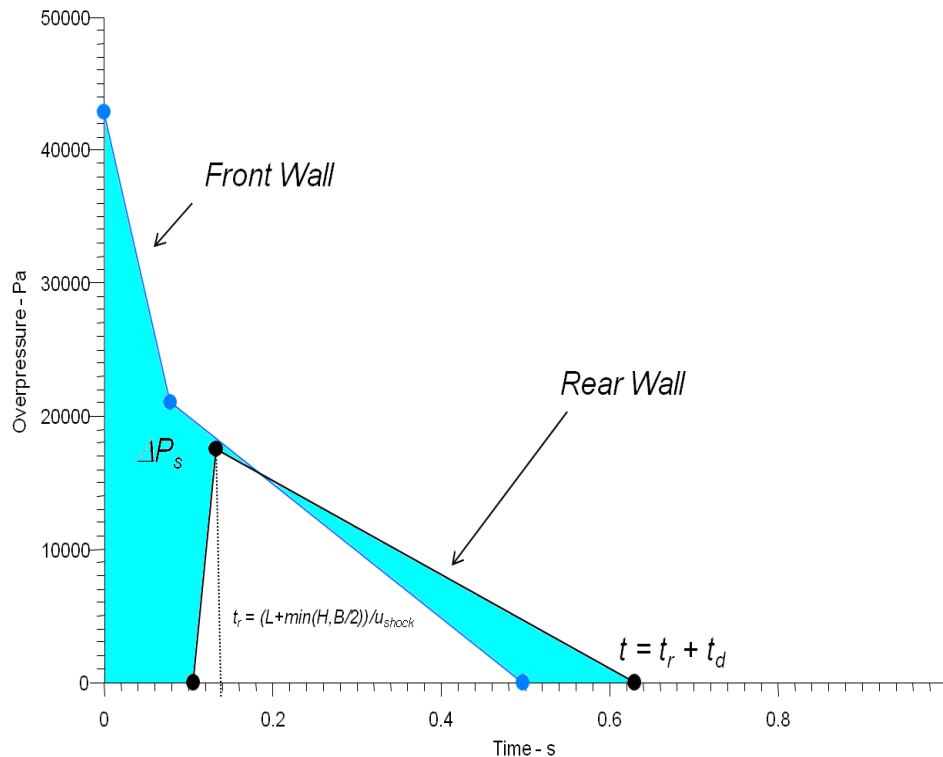
The frame loading for the ethylene explosion considered earlier is shown in Figure A.11. The colored area is the net difference between the front wall and rear wall loadings.

5.5 Negative Pressure and Rebound Loading

In most explosion dynamics studies, only the positive phase duration properties are used, mainly the peak reflected overpressure and impulse. The negative pressure forces are generally ignored since they are relatively small and are not easily quantified for vapor cloud explosions.

The inclusion of negative phase pressure is important for low stiffness structures. These structures

Figure A.11: An Example of Side Wall and/or Roof Loading



often have a long response time relative to the explosion positive phase duration. In these cases, the negative phase duration can be experienced by the structure before the structure reaches its maximum deflection from the positive phase portion of the explosion.

The components of a building will also experience blast load effects, opposite in direction to the primary blast load effects, due to the negative phase (suction) of the blast wave, together with the rebound of the structural components from the inertial effects of the overpressure loading.

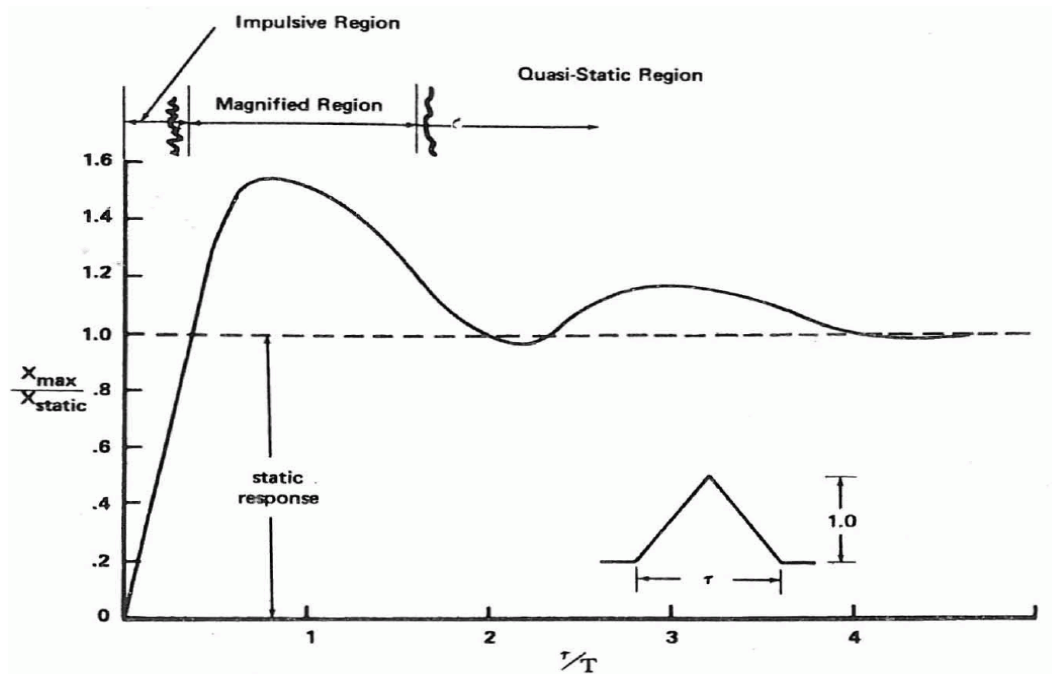
The structural components of the building should be adequately detailed to perform satisfactorily for the rebound effects. These effects can be quantified from the time history dynamic analysis of the building structural components.

6. Structural Dynamics

Structural loading mechanisms can be classified as diffraction or drag-type loadings. Diffraction-type loadings result from direct and reflected pressures during initial envelopment of the structure. As the pressure traverses the structure, it bends or "diffracts" around it so the structure is eventually engulfed by the pressure wave. The duration of diffraction loading is a function of:

- shock velocity of propagation, and
- structural element geometry.

Figure A.12: Structural response spectrum for a triangular load



Drag-type loading is caused by the strong winds behind the shock front. Its duration is approximately equal to the positive phase duration of the pressure wave and does not depend on the geometry of the structure.

Structural response combines the transient loading with the dynamic response characteristics of the structure. The dynamic structural response can be expressed as an infinite series of natural modes of vibration with time-dependent coefficients. One mode is usually considered for reasonable estimates of structural integrity. Pressure pulse duration and dynamic characteristics of structural elements are essential for integrity estimates.

Let us define τ as the ratio of the duration of explosion pressure load on a given structure over the natural period of vibration of the structure. The magnitude of τ will in general determine how the structure reacts to the pressure load (see Figure A.12):

- $\tau > 1$ The structural loading is equivalent to a static load of a magnitude equal to the explosion peak overpressure.
- $\tau = 1$ The structural loading is equivalent to a static load of a magnitude greater than the explosion peak overpressure which can be as large as $\pi/2$ times the peak overpressure.
- $\tau < 1$ The structural loading is equivalent to a static load of a magnitude lower than the explosion peak overpressure, i.e, the structure can withstand a higher dynamic pressure than the static load required to cause failure.

Natural modes of vibration depend on many factors such as materials of construction, the size of components, etc. For example, the natural period of vibration of concrete ranges from 10 to 30 ms.

Tables A.2 and A.3 (see references [13] and [14]) describe expected overpressure damage estimates for humans, structural elements, and process equipment.

In addition to the composition, temperature, pressure, phase, and flammability limits, the following parameters should be considered:

- time of ignition,
- mass within the flammable limits,
- presence of obstacles,
- venting,
- ignition source strength,
- laminar burning velocity and flame acceleration, and
- fuel sensitivity.

Table A.2: Explosion overpressure damage estimates

| Overpressure (psi) | Expected damage |
|--------------------|---|
| 0.03 | occasional breaking of large windows already under stress |
| 0.04 | loud noise (143 dB) |
| | sonic boom glass failure |
| 0.1 | breakage of small windows under strain |
| 0.15 | typical pressure for glass failure |
| 0.3 | some damage to house ceilings |
| | 10 % window glass breakage |
| 0.4 | limited minor structural damage |
| 0.5 - 1 | windows usually shattered with some window frame damage |
| 0.7 | minor damage to home structures |
| 1 | partial demolition of houses which are made uninhabitable |
| 1 - 2 | corrugated metal panels fail and buckle |
| | housing wood panels blown in |
| 1 - 8 | range for slight to serious injuries due to skin lacerations from flying glass and other missiles |
| 1.3 | steel frame of clad building slightly distorted |
| 2 | partial collapse of walls and roofs of houses |
| 2 - 3 | Non-reinforced concrete or cinder block walls shattered |
| 2.3 | lower limit of serious structural damage |
| 2.4 - 12.2 | range for 1 to 90 % eardrum rupture among exposed population |
| 2.5 | 50 percent destruction of brickwork |
| 3 | steel frame building distorted and pulled away from foundation |
| 3 - 4 | frameless steel panel building ruined |
| 4 | cladding of light industrial buildings ruptured |
| 5 | wooded utility poles snapped |
| 5 - 7 | nearly complete destruction of houses |
| 7 | loaded train wagons overturned |
| 7 - 8 | 8-12 in. thick non-reinforced brick fail by shearing of flexure |
| 9 | loaded train box cars demolished |
| 10 | Probable total building destruction |
| 15.5 - 29 | Range for 1 to 99 percent fatalities among exposed population due to direct blast effects |

Table A.3: Explosion overpressure damage estimates

| Equipment | Overpressure PSI | | | | | | | | | | | | | | | | | | | | | | | | | | | | | | | |
|---------------------------------|------------------|-----|-----|-----|-----|-----|-----|-----|-----|-----|-----|-----|-----|-----|-----|-----|-----|-----|-----|------|------|------|------|------|------|------|---|---|---|---|---|---|
| | 0.5 | 1.0 | 1.5 | 2.0 | 2.5 | 3.0 | 3.5 | 4.0 | 4.5 | 5.0 | 5.5 | 6.0 | 6.5 | 7.0 | 7.5 | 8.0 | 8.5 | 9.0 | 9.5 | 10.0 | 12.0 | 14.0 | 16.0 | 18.0 | 20.0 | 20.0 | | | | | | |
| Control house steel roof | a | c | d | | | | n | | | | | | | | | | | | | | | | | | | | | | | | | |
| Control house concrete roof | a | e | p | d | | | n | | | | | | | | | | | | | | | | | | | | | | | | | |
| Cooling tower | b | | f | | | | o | | | | | | | | | | | | | | | | | | | | | | | | | |
| Tank: cone roof | d | | | | | k | | | | | | | | | | | | | | | | | | | | | u | | | | | |
| Instrument cubicle | | a | | | | i | m | | | | | | | | | | | | | | | | | | | | t | | | | | |
| Fired heater | | | | g | | | | | | | | | | | | | | | | | | | | | | | t | | | | | |
| Reactor: chemical | | | | a | | | | | | | | | | | | | | | | | | | | | | | p | t | | | | |
| Filter | | | | h | | | | | | | | | | | | | | | | | | | | | | | f | v | t | | | |
| Regenerator | | | | | | | i | | | | | | | | | | | | | | | | | | | | i | p | t | | | |
| Tank: floating roof | | | | | | | k | | | | | | | | | | | | | | | | | | | | | u | d | | | |
| Reactor: cracking | | | | | | | i | | | | | | | | | | | | | | | | | | | | | i | t | | | |
| Pipe supports | | | | | | | p | | | | | | | | | | | | | | | | | | | | | s | o | | | |
| Utilities: gas meter | | | | | | | | | | | | | | | | | | | | | | | | | | | | q | | | | |
| Utilities: electric transformer | | | | | | | | | | | | | | | | | | | | | | | | | | | | h | i | t | | |
| Electric motor | | | | | | | | | | | | | | | | | | | | | | | | | | | | h | i | v | | |
| Blower | | | | | | | | | | | | | | | | | | | | | | | | | | | | q | t | | | |
| Fractionation column | | | | | | | | | | | | | | | | | | | | | | | | | | | | r | t | | | |
| Pressure vessel horizontal | | | | | | | | | | | | | | | | | | | | | | | | | | | | p | i | t | | |
| Utilities: gas regulator | | | | | | | | | | | | | | | | | | | | | | | | | | | | i | m | q | | |
| Extraction column | | | | | | | | | | | | | | | | | | | | | | | | | | | | i | v | t | | |
| Steam turbine | | | | | | | | | | | | | | | | | | | | | | | | | | | | | i | m | s | v |
| Heat exchanger | | | | | | | | | | | | | | | | | | | | | | | | | | | | | i | t | | |
| Tank sphere | | | | | | | | | | | | | | | | | | | | | | | | | | | | | i | t | | |
| Pressure vessel: Vertical | | | | | | | | | | | | | | | | | | | | | | | | | | | | | i | t | | |
| Pump | | | | | | | | | | | | | | | | | | | | | | | | | | | | | i | y | | |

Code

- a. Windows and gauges break
- b. Louvers fall at 0.3-0.5 psi
- c. Switchgear is damaged from roof collapse
- d. Root collapses
- e. Instruments are damaged
- f. Inner parts are damaged
- g. Brick cracks
- h. Debris-missile damage occurs
- i. Unit moves and pipes break
- j. Bracing fails
- k. Unit uplifts (half-filled)
- l. Power lines are severed
- m. Controls are damaged
- n. Block walls fail
- o. Frame collapses
- p. Frame deforms
- q. Case is damaged
- r. Frame cracks
- s. Piping breaks
- t. Unit overturns or is destroyed
- u. Unit uplifts (0.9 filled)
- v. Unit moves on foundation

Source:
 Stephens, M.M., *Minimizing Damage To Refineries*, U.S. Dept. of the Interior, Office of Oil & Gas, Feb. 1970

Appendix B

Vapor Cloud Explosion Modeling

1. Introduction

When a large amount of a combustible hydrocarbon or other combustible material is accidentally released into the atmosphere, one of four results will occur:

- the release may mix with the air and disperse harmlessly to low levels of concentration (below the lower flammable limit) without ignition
- it may be ignited immediately, near the point of release, producing a fire but no explosive (blast wave) effects
- it may disperse over a wide area before being ignited, resulting in a large fire
- or it may disperse over a wide area, ignite, and under conditions conducive to a rapid acceleration of the flame front, produce an explosive blast wave.

The occurrence of such unconfined vapor-cloud explosions, or UVCEs, has increased over the years - over 50 ignited vapor clouds were reported for the 1975-1980 time period, over one half of which developed blast waves. Current estimates of eight ignited vapor cloud accidents worldwide per year are consistent with this frequency.

Most UVCE events reported in the literature have been "momentum-dominated gas jets" released from storage vessels or from pressurized process systems.

The process involved in the development of a blast wave from an ignited vapor cloud are not well understood. Much of the research and analysis on this matter have focused on the acceleration of the flame speed of the flame front. The flame speed is equal to the sum of the burning velocity and the velocity of the bulk motion of the burnt and unburnt gases at and near the flame front.

Burning velocities for ignited vapor clouds of combustible gases are typically of the order of 1 m/sec under laminar flow conditions, and of the order of 10 m/sec under turbulent flow conditions. The development of a blast wave requires much higher flame speeds - of the order of 250-300 m/sec, or close to sonic velocities. The acceleration of the flame front to these speeds requires a

turbulent condition within the vapor cloud near the front. Turbulence will develop due to obstacles (piping, structures, process vessels, etc.), or according to some investigators, can develop from the mixing of the burnt and unburnt gases at the front itself. It should be noted, however, that all major recorded UVCE events have occurred under conditions in which turbulence from obstacles within and close to the vapor cloud could be expected. Such "semi-confined" conditions within the cloud are considered, therefore, to be an important, and perhaps necessary, condition for an explosion to occur.

If the flame front must accelerate substantially to develop an explosive blast front, then it is reasonable to ask whether a minimum amount of combustible material in the vapor cloud is required, or more generally, to what degree does the size of the release influence the possibility of an explosion. From historical data, Wiekema (1984) concludes that a spill of 100 to 1000 kg is needed for a UVCE to occur. The 100 kg is probably reasonable for highly energetic materials such as hydrogen (and perhaps ethylene), while one tonne is probably a reasonable minimum size for most hydrocarbons. Above these limits, the amount of material apparently has no significant influence on whether or not a blast wave will develop after ignition - other factors, such as the presence of turbulence generators, meteorological conditions, delay before ignition, etc. are of more importance than the mass of material.

With that brief background, this chapter attempts to present in summary form the current status of thinking on UVCEs. Little is understood about UVCEs: how they develop from ignited vapor clouds; how flame fronts accelerate to the velocities needed for blast waves to occur; and what the time-history of the resulting blast wave is like; and particularly how it compares to the known characteristics of blast waves from condensed phase explosions.

2. Characteristics of Condensed Phase Explosions

The properties of an explosive source which contribute to its effects include its total energy (heat of detonation, heat of combustion), its energy density, and the rate of energy release upon initiation of the explosion. So-called "ideal" explosions would have very high (infinite) energy densities and release rates so that the resulting blast wave would be correlated entirely by the value of the total energy. The four types of explosives which approximate "ideal" characteristics are point-source, nuclear, laser spark, and condensed phase explosions (discussion in Baker). Of these, the condensed phase explosions, which include all "high explosives" materials such as *TNT*, dynamite, RDX, etc., are of particular interest because most experimental data on explosive blast waves have been obtained from detonation of such explosives.

The total energy of an explosive is the product of the weight of the explosive and the energy weight density (sometimes referred to as the "specific" energy or the "heat of detonation") of the explosive. This rather obvious statement is necessary because even *TNT* can vary in energy density, obtained either experimentally or calculated from thermodynamic properties, as much as 10 percent or more dependent on its packed density. An average value for *TNT* is about 4500 kJ/kg, or about 1.5×10^6 ft-lbs/lb.

The specific energies of other types of high explosives (see Baker) vary from 1540 kJ/kg for lead

azide to as high as 7540 for Torpez, a mixture of *TNT*, RDX and aluminum.

Condensed phase explosions will result in a blast wave whose properties at any distance is dependent only upon the total energy of the explosive material. This characteristic results in similitude parameters known as Sachs scaling which relate the distance, total energy (in the form of charge weight), and propagation medium properties to the blast wave pressure, impulse and time. For peak overpressure, the relationship is:

$$\frac{\Delta P}{P_0} = f \left(\frac{RP_0^{1/3}}{W^{1/3}} \right) \quad (\text{B.1})$$

where ΔP is overpressure, P_0 is the ambient pressure, R is distance, and W is the heat of detonation of the explosive charge, usually expressed as equivalent weight of a standard (*TNT*) explosive.

A special case of Sachs scaling, known as Hopkinson scaling, is used for invariant ambient conditions, which would be the case for explosions at or near the ground surface. In such cases, the relationship is:

$$\Delta P = f \left(\frac{R}{W^{1/3}} \right) = f(\lambda) \quad (\text{B.2})$$

where λ is the scaled distance parameter. This is the form commonly seen in Lees, the HSE reports, and Kingery and Pannill, and is of particular interest in risk and hazard studies. The functional form usually chosen for correlation purposes is:

$$\Delta P = C\lambda^{-\alpha} \quad (\text{B.3})$$

Various investigations have developed analytical or empirical models for *TNT* and/or nuclear explosives at sea level conditions and have found fits to this functional equation as follows (from Pater). These expressions are in English units, with ΔP in (psi) and λ in (ft/lbs^{1/3}):

$$\text{NOL: } \Delta P = 36.8\lambda^{-1.09} \text{ for } \lambda > 130 \quad (\text{B.4})$$

$$\text{Swisdak: } \Delta P = 108\lambda^{-1.28} \text{ for } \lambda > 10 \quad (\text{B.5})$$

$$\text{Reed: } \Delta P = 56.8\lambda^{-1.1} \text{ for all } \lambda \quad (\text{B.6})$$

$$\text{BRL: } \Delta P = 227\lambda^{-1.41} \text{ for } 40 < \lambda < 1000 \quad (\text{B.7})$$

The following should be noted:

- For a free-air spherical expansion of a wave, without non-spreading attenuation, $\alpha = -1$. This represents the case for so-called "spherical-spreading" of an acoustic wave. This is approximately the situation for an explosive blast wave at low overpressures, probably less than 0.1 psi. Since α is, in all of the equations, less than -1.0, the excess amount represents attenuation of the blast wave due to the thermodynamic energy losses and mass transfer associated with shock fronts.

- Any equation with $\alpha = \text{constant}$ represents a straight line on log-log paper. Since the well-established *TNT* curves in common use are curved (see Figures B.3 and B.4), the non-linearity implies that $\alpha = f(\lambda)$. In any case, it is more reasonable to use such curves directly, or tabulations of ΔP vs. λ rather than any of the equations given above.
- Many of the *TNT* curves and the fitted equations are based on free-air spherical blast waves. For use in risk and hazard studies, where in almost all cases the explosive material is on or near the ground surface, the equivalent weight, W , should be increased to reflect hemispherical radiation. This implies a doubling of the equivalent weight. Some investigations have suggested an increase of 1.8 instead of 2.0 to account for cratering (if any) and ground attenuation effects.
- It is not always clearly stated in the literature whether a given ΔP vs. λ curve is for spherical or hemispherical radiation of the blast wave. Kingery and Pannill, and the HSE curves in the Second Report are definitely hemispherical; the curves in Lees is most likely spherical radiation. Obviously, hemispherical radiation produces a higher overpressure at a given distance for a given charge.
- Some blast wave curves are plotted with both parameters normalized in terms of P_0 , the ambient pressure, thus,

$$\frac{\Delta P}{P_0} = f\left(\frac{R}{(W/P_0)^{1/3}}\right) \quad (\text{B.8})$$

in keeping with the more universal Sachs scaling. Such curves are shown in Baker. Note, also, that the large fold out blast curves in the rear of the Baker book are for spherical radiation.

3. UVCE Incident Histories

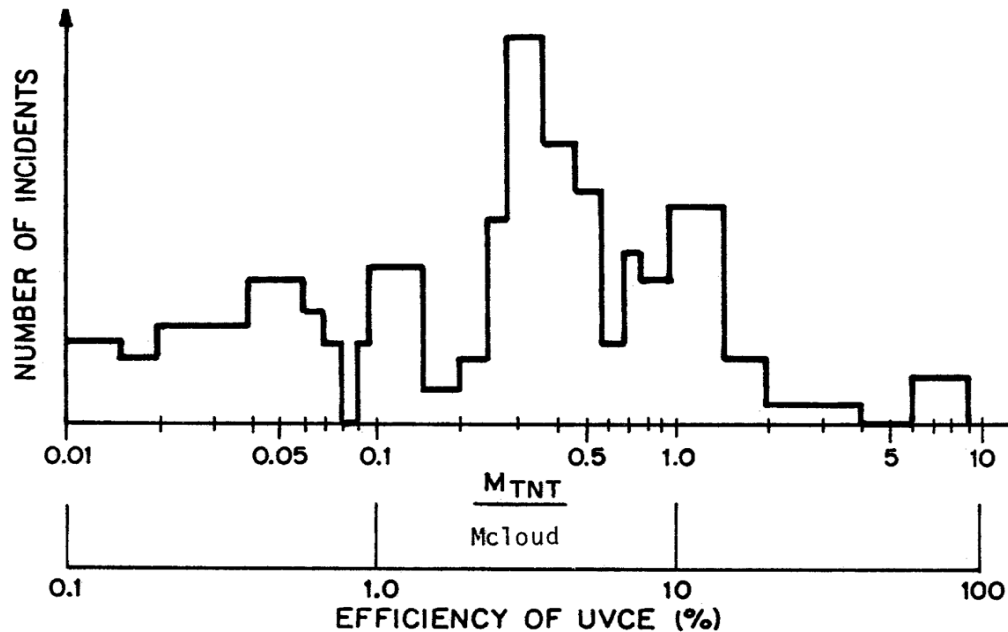
Summaries of UVCE incidents are presented in Davenport (1977), Slater (1978), Gugan (1979), Lewis (1980), and an update by Davenport (1983). These listings generally include dates, type and weight of material released, and damage descriptions. Davenport (1977) includes 43 incidents in which a blast wave (overpressure) occurred out of a total of 59 incidents through 1976, noting that the occurrence of unignited vapor clouds, or ignited vapor clouds which do not result in a blast wave are likely to be under reported. Based on his surveys, Davenport suggests that an efficiency of 2 percent for vapor cloud explosives is reasonable.

Slater lists 47 vapor cloud incidents from the period 1921 through 1975, including BLEVEs and non-blast wave producing incidents.

Gugan's book includes both fireballs and UVCEs and lists 100 incidents from 1921 through 1977, with half of these occurring since 1965. Blast effects were produced in 56 of the 100 incidents. Gugan also provides some analyses involving explosive efficiencies as a function of quantity released and of flammability parameters. Note that some of the high efficiency explosions are improperly calculated - *TNT* equivalent and efficiency are misrepresented. (Discussed later).

Figure B.1: *TNT* equivalent of unconfined vapor cloud explosions

(See [15])



Lewis includes descriptive accounts of 20 UVCE incidents in industrial sites, and 17 incidents occurring in storage installations, during transport, or at other open non-industrial sites, all within the 1921-1977 time period.

Davenport (1980) expanded his previous paper to study "several hundred" incidents extending from 1921 through 1983, and updated his 1977 paper to include 71 UVCE events. Of these, 51 occurred within hydrocarbon processing plants, 16 were transport incidents, and 4 occurred in other sites.

4. Theoretical and Experimental UVCE Studies

The majority of explosion related research efforts during the last decade focused on the following areas:

- Flame acceleration mechanisms
- Deflagration to detonation transitions
- Direct initiation of detonations
- Overpressure levels within the combustion zone

- Effects of pressure rise time dependency on structures vs. *TNT* curves
- Minimum amount of mass sufficient to sustain a UVCE
- Explosion efficiencies

The original attempt at understanding the properties and characteristics of UVCE's was presented in 1946 by G. I. Taylor. Taylor's combustion model used a piston concept (an infinitely extensible spherical piston) to displace the vapor cloud, thereby compressing it and simultaneously imparting a velocity to it to establish a shocked condition.

This concept, which is based on the similarity of such a piston movement and the exothermic reaction during the flame propagation of an ignited vapor cloud, has been widely used and modified by subsequent investigators.

Many subsequent modeling studies, according to Zalosh [16], have been based on simplified, and perhaps unrealistic, assumptions of cloud formation and ignition - such as a centralized ignition of a homogeneous hemispherical cloud.

The quantitative evaluation of the decay properties of the shock front, which begins to decay when the combustion process is complete and the flame has consumed all of the flammable vapor, has not been resolved satisfactorily. These decay properties are, of course, of particular importance in damage analysis or in risk analysis, as they would define the differences between UVCEs and *TNT*-like explosions.

Gugan [17] presents a general discussion of the fundamentals of combustion as they relate to the development of unconfined vapor clouds upon ignition. In Appendices, Gugan also provides a theoretical treatment of the formation of vapor clouds and of the blast waves developed after ignition.

Wiekema [18] develops a model to estimate the blast overpressure and positive phase duration on the basis of the sensitivity to flame acceleration of the combustible mixture.

Lee and Moen [19] present a scholarly experimental/theoretical study of the transition mechanisms from deflagration to detonations in UVCEs. Their principal conclusion is that this transition requires flame acceleration by large-scale turbulence during all stages of the combustion process.

Marshall [20] conducted theoretical studies of the size of flammable clouds in terms of the mechanisms controlling dispersion, momentum, buoyancy, and atmospheric turbulence.

Geiger [21] discusses several areas of investigation of UVCEs in Germany, with particular emphasis on detonation-like explosive modes.

Strehlow [22] presents a survey paper on ideal and non-ideal blast waves from accidental explosions. Most accidental explosions will produce non-ideal blast characteristics because of the way that energy is added to or is initially distributed in the source region, and by implication, the degree to which the burning flame accelerates; this acceleration is required for the explosion to develop a blast wave similar to that produced by a condensed phase explosion.

According to Strehlow, when the flame subsequently decelerates to a velocity of less than about 1/16th of the velocity of sound, then the lead shock wave is reduced to a simple compression

wave propagating away from the source region. This is an important concept, which provides a sound explanation for reduction in the decay of overpressure in the far field (relative to *TNT*-type explosions), or, subsequently, the transformation of the shock-like overpressure wave to an acoustic wave.

Phillips ([23] and [24]) discusses research in the U.K. on the mechanism of vapor cloud explosions, and on the dispersion of the cloud. In particular, mechanisms for the acceleration of the flame front by turbulence, by semi-confinement of the cloud, and by a postulated two-fluid model for burnt and unburnt gases moving at different velocities are considered.

Hasegawa and Sato [25] studied the development of the blast wave from UCVEs in deflagration using both theoretical and small-scale experimental methods. The theoretical approach was based on a piston analogy, and provided a reasonable comparison with the experimental results.

Koch, et al. [26] present an excellent summary of previous theoretical and experimental studies in UVCE explosions, with particular emphasis on the likelihood and requirements for transition of a deflagration to a detonation. The conclusions reached in the study are that detonation may occur in cases of jet ignition, but otherwise detonation need not be postulated in safety studies.

Wingerden and Berg [27] evaluated three blast wave simulation codes: a low flame speed (≤ 100 m/s) Piston model and two gasdynamic-equation-based codes which are applicable for higher flame speeds. Each of these models are based on a spherical symmetric blast wave, although the piston model was investigated for applicability to pancake-shaped vapor clouds. Comparison to small-scale experiments included reasonable simulation of the shape of the blast wave, but only fair prediction of the decay of the blast wave.

Some analytical work has been done on the effects of the shape and symmetry of the vapor cloud, prior to its ignition, on the subsequent characteristics of the blast wave. Geiger [21] compares the pancake-shape of dense vapor releases with the more normal acceptance of a hemispherical cloud shape and concludes that the decay of overpressure beyond the cloud edge is more rapid for a pancake-shaped cloud than for a hemispheric cloud. (Other investigators have also reached this conclusion - see Pickles and Bittleston below). As discussed subsequently, this is not consistent with damage analyses.

Pickles and Bittleston [28] have analyzed the asymmetric blast wave from an elongated (ellipsoidal) cloud ignited at one end, and, using a numerical procedure based on an acoustic theory approximation, concluded that the asymmetry of the blast wave can be pronounced, with overpressures in the direction of flame propagation being four times greater than in the reverse direction, even at long range. They also concluded that the overpressure levels in any direction would be less than those from a hemispherical cloud of the same volume. Again, this is not consistent with damage analyses in the far field.

Taylor [29] showed that the Pickles and Bittleston results for an elongated cloud with edge ignition could be developed in analytic form.

It seems fair to conclude, as Strehlow [22] does, that "the acoustic theory for high aspect ratio source regions shows conclusively that deflagrative combustion as such cannot produce the damaging blast waves that have been observed as the result of UVCES."

This implies that very high-speed deflagrations or detonations must occur within vapor clouds that result in large blast pressures. For this reason, recent research on UVCEs has focused on mechanisms for the production of high-speed or accelerated flames and the possibility of deflagration-to-detonation transition (DDT) occurring in unconfined or partially confined clouds. While this research has been very productive, there are many outstanding problems such as how to scale up experiments done in the laboratory, and developing numerical predictions of DDT that can be used for hazard assessment. Due to these unresolved issues, large-scale experiments have been and will continue to play a very important role in assessing hazards.

5. Obstacles and Confinement Effects

The ¹ two main issues addressed in experiments and models have been the role of confinement and obstacles in accelerating flames and causing DDT. One key observation from experiments on unconfined flames (spherical or hemispherical clouds with central ignition) is that transition to detonation is exceedingly difficult for completely unconfined configurations. Only with the addition of grids or screens in the path of the flame was DDT produced in sensitive fuel-oxygen mixtures (Wagner et al. [30]). Even with large-scale (10 m diameter) clouds, merely low speed (20-50 m/s) flames were produced in completely unconfined fuel-air mixtures (Brossard et al. [31]). There appear to be two significant factors contributing to the ineffectiveness of flame acceleration for completely unconfined flames. First, the natural instability mechanisms of flames only cause a moderate growth in the flame surface area. Second, the lack of confinement results in a substantial decoupling between the upstream fluid motion and the flame motion. This corresponds to rapid decay ($1/r^2$) of the velocity and pressure fields in spherical source flows.

Another key fact is that the addition of obstacles to confined flames produced dramatic accelerations (flame speeds up to 400 m/s) within a short distance for both tubes (Wagner [32]) and cylindrical (pancake) geometries (Moen et al. [33], Moen et al. [34]). While initial studies were with sensitive fuel-oxygen mixtures in small-scale, large-scale experiments (Moen et al. [35]) demonstrated that similar effects could be obtained with insensitive fuel-air mixtures if the scale was increased sufficiently. Using periodic obstacles (orifice plates) or spirals within a tube, (Lee et al. [36]) were able to obtain sufficient flame acceleration to produce DDT in H₂-air and C₂H₂-air mixtures and flame speeds of up to 800 m/s in methane-air mixtures within 5-10 tube diameters of the igniter.

The flame speeds produced in confined clouds, i.e., within tubes, suggests that such processes might be possible in unconfined clouds. A number of studies have been directed towards this possibility over the past decade. Many of these tests have emphasized complex geometries combining partial confinement and obstructions. While these situations are clearly not just simple unconfined vapor clouds, many industrial accidents involving fuel-air explosions do occur near or within process equipment and structures, and these studies are relevant to these common situations.

Work in small-scale by Chan et al. [37] and Urtiew et al. [38] demonstrated the significance of confinement for producing substantial accelerations and also showed the importance of the flame-

¹A portion of this section was contributed by Professor Joseph Shepherd, Department of Mechanical Engineering, RPI, Troy, New York

vortex interactions. Experiments have also been performed with pancaked-shaped fuel-air mixtures at various scales through "forests" of obstacles (van Wingerden and Zeeuwen [39]). Ultimate flame velocities were increased by a factor of up to 8 by confining the flame to a cylindrical channel but only moderate terminal velocities (50 m/s) were achieved. These experiments demonstrated that the early stages of flame acceleration in hydrocarbon-air mixtures could be scaled on the basis of a single parameter, the laminar flame speed.

Later work at large scale showed the possibility of acceleration leading to DDT for H₂-air mixtures in partially-obstructed and vented channels, (Sherman et al. [40] Sherman et al. [41], Tieszen et al. [42]). These tests demonstrate that venting can have both a negative and positive effect on flame acceleration. With a small amount of venting from the top of a channel confined on the remaining three sides, the flows induced by venting contributed to flame acceleration. Increasing the venting (percentage of open area) results in the eventual reduction of the flame acceleration and inhibits transition to detonation completely if the venting is large enough. Moen et al. [43] demonstrated DDT in C₂H₂-air mixtures in a channel, vented on the top and filled with an array of pipe obstructions. The flame speed just prior to transition was 400 m/s. Flame speeds up to 200 m/s were observed in propane-air mixtures and a quasi-steady-state propagation rate was achieved within several meters of the ignition source.

It is important to note that in the large-scale experiments of Moen et al. DDT was observed in only the most sensitive mixtures. These experiments were essentially unconfined but highly-obstructed, designed to simulate an accident within a pipe-rack or a portion of a processing plant. The failure to produce DDT or substantial flame acceleration in less sensitive mixtures reinforces the notion that it is extremely difficult to obtain detonation in completely unconfined vapor cloud explosions, even when numerous obstructions are present.

6. Jet Ignition Effects

It has been known for a decade that it is possible to initiate detonation by high-speed turbulent flame-jets or combustion product jets. The first demonstration by Knystautas et al. [44] of this important mechanism for shockless initiation of detonation was in small scale with sensitive fuel-oxygen mixtures. Later studies by Schildknecht et al. [45], Moen et al. [46], and Mackay et al. [47] have concentrated on the initiation of sensitive fuel-air mixtures at large (1-10 m) scales. These experiments have demonstrated that transition to detonation can be induced in essentially unconfined fuel-air mixtures of moderate sensitivity (H₂ and C₂H₂). Such tests are a dramatic confirmation of the modern notions that the absolute dimensions and method of ignition play a key role in determining the ability to initiate detonations. Even though detonation was not produced in less sensitive fuel-air mixtures such as ethylene and propane, substantial overpressures (1-6 bar) were produced by these explosions. This indicates the hazardous nature of flame-jet ignition, a common scenario in industrial accident analysis. Criteria for jet initiation of detonations are less clear but the absolute velocity of the jet and the jet turbulence parameters appear to be the most important factors.

7. TNT Equivalence Analysis

The basic *TNT* curve relating the peak overpressure of the blast wave from a condensed phase *TNT* explosion to the scaled distance parameter, in accordance with the Hopkinson scaling, is shown in both Figures B.3 and B.4. These curves are based on a series of experiments and weapons tests carried out over many years, and represents the peak overpressure, for a *TNT* explosion on the ground surface, which generates an overpressure blast wave which radiates into a hemispherical space.

Although the characteristics of the blast wave from a vapor cloud explosion are known to differ substantially from those resulting from a *TNT* explosion, it is common in explosion investigations to establish an "equivalent *TNT* yield" for the vapor cloud explosion. The principal reason for this is that the characteristics of *TNT* explosions, including the blast effects and the relation of the overpressure wave to the distance from the center of the explosion and to the charge weight of *TNT* have been well established from extensive experiments and weapons tests. These *TNT* data can be used, therefore, to estimate the quantity of explosive material involved in the accidental release, or the effective source strength of the vapor cloud explosion.

The equivalent *TNT* yield is based on two factors: first, the ratio of the heat of combustion of the combustible gases in the vapor cloud to the heat of detonation of *TNT*; and, second, the efficiency of the vapor cloud explosion.

An equivalent mass of *TNT* is calculated using the following equation:

$$M_{TNT} = \frac{\Delta H_c}{1155} \times E_f \times M_{cloud} \quad (\text{B.9})$$

where M_{TNT} is the *TNT* equivalent mass in (kg), ΔH_c is the lower heat of combustion in (kcal/kg), M_{cloud} is the total mass in the cloud in (kg), and E_f is the explosion efficiency.

The distance to a given overpressure is then calculated from the equation:

$$X = 0.3967 \times M_{TNT}^{1/3} \exp [3.5031 - 0.7241 \ln(\Delta P) + 0.0398(\ln \Delta P)^2] \quad (\text{B.10})$$

where X is the distance to given overpressure in meters and ΔP is the peak overpressure in (psi). If ΔP is expressed in Pa, then:

$$X = 0.3967 \times M_{TNT}^{1/3} \exp [13.0121 - 1.4276 \ln(\Delta P) + 0.0398(\ln \Delta P)^2] \quad (\text{B.11})$$

$\frac{\Delta H_c}{1155}$ is the ratio of the total energy available per unit mass of material. For most hydrocarbon materials, this ratio is about ten. Thus, on a mass basis, a hydrocarbon release has ten times as much potential explosive energy as *TNT*.

E_f relates to how well or efficiently the vapor cloud behaves as an explosive material upon ignition. The efficiency is dependent upon several conditions, including the quantity released, the rate of release, the direction of release, wind and atmospheric stability at the time of the release, the time between the initial release and ignition of the cloud, and degree of confinement and turbulent mixing of the released vapor with air.

Kinney and Graham [14] report another simple expression for estimating the maximum peak overpressure, impulse, and duration from a *TNT* explosion as a function of scaled distance λ :

$$\lambda = \frac{X}{M_{TNT}^{1/3}} \quad (\text{B.12})$$

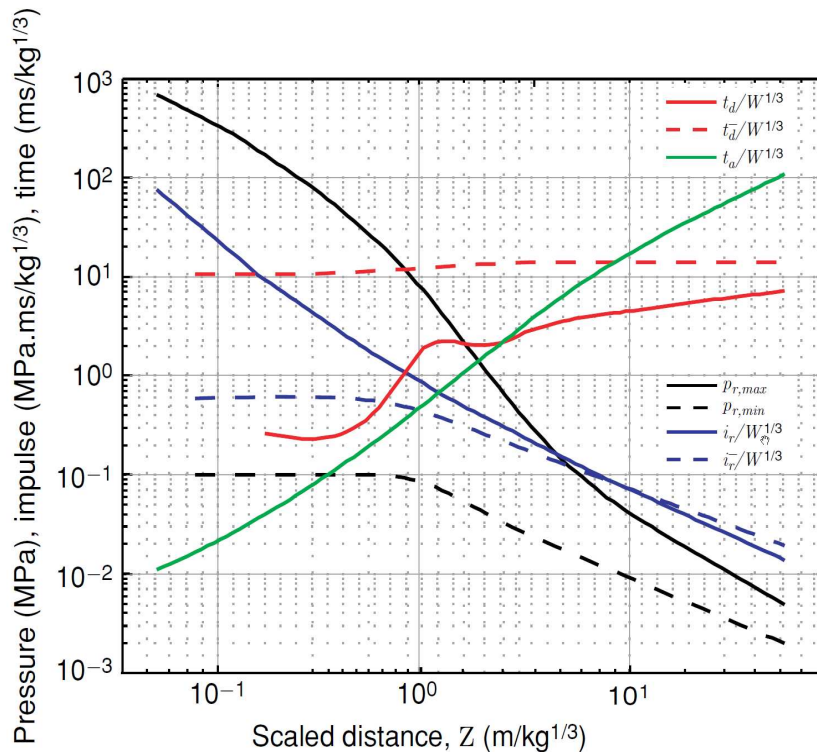
$$\Delta P_{max}(\lambda) = P_s \frac{808 \left[1 + \left(\frac{\lambda}{4.50} \right)^2 \right]}{\sqrt{\left[1 + \left(\frac{\lambda}{0.048} \right)^2 \right] \left[1 + \left(\frac{\lambda}{0.32} \right)^2 \right] \left[1 + \left(\frac{\lambda}{1.35} \right)^2 \right]}} \quad (\text{B.13})$$

$$I(\lambda) = M_{TNT}^{1/3} \frac{6.7 \sqrt{1 + \left(\frac{\lambda}{0.23} \right)^4}}{\lambda^2 \left[1 + \left(\frac{\lambda}{1.55} \right)^3 \right]^{1/3}} \quad (\text{B.14})$$

$$t_d(\lambda) = M_{TNT}^{1/3} \frac{0.98 \left[1 + \left(\frac{\lambda}{0.54} \right)^{10} \right]}{\left[1 + \left(\frac{\lambda}{0.02} \right)^3 \right] \left[1 + \left(\frac{\lambda}{0.74} \right)^6 \right] \sqrt{1 + \left(\frac{\lambda}{6.9} \right)^2}} \quad (\text{B.15})$$

where P_s is the ambient/surroundings pressure in Pa, I is the impulse in Pa.s, and t_d is the duration in s. For a triangular overpressure pulse, I can be approximated as $I \simeq \frac{1}{2} \Delta P t_d$.

Figure B.2: TNT Equivalence Negative Phase Scaled Parameters



Although the negative phase duration is less understood, Rigby et al. [7, 8] (also see SBEDS [48]) published and validated very useful guidance on how to estimate the negative phase impulse, peak

underpressure, and duration. Their validation study shows that the cubic negative phase form discussed earlier produced high quality predictions when compared to their actual test data:

$$\Delta P(t) = \Delta P_{min} \frac{27}{4} \left(\frac{t}{t_d^-} \right) \left(1 - \frac{t}{t_d^-} \right)^2 \quad (\text{B.16})$$

Integration of Equation B.16 yield the following expression for negative phase impulse:

$$I^- = \frac{9}{16} \Delta P_{min} t_d^- \quad (\text{B.17})$$

The values of ΔP_{min} in Pa and I^- in Pa.s can be obtained from the following curve fits of the data shown in Figure B.2. For small scaled distances, the peak under-pressure and negative phase impulse are very small relative to those for the positive phase. The negative phase impulse approaches the positive phase impulse for larger scaled distances and eventually exceeds it at values of Z greater than 8.

$$\frac{\Delta P_{min}(\lambda)}{1000} = 101 \text{ for } 0.071 < \lambda \leq 0.668 \quad (\text{B.18})$$

$$= 106 + 13.0\lambda - 32.9\lambda^2 \text{ for } 0.668 < \lambda \leq 1.270 \quad (\text{B.19})$$

$$= \frac{93}{\lambda^{1.22}} \text{ for } 1.270 < \lambda \leq 2.78 \quad (\text{B.20})$$

$$= \frac{73}{\lambda^{0.978}} \text{ for } 2.780 < \lambda \leq 37.6 \quad (\text{B.21})$$

$$\frac{I^-(\lambda)}{M_{TNT}^{1/3}} = 553 + 445\lambda - 724\lambda^2 \text{ for } 0.071 < \lambda \leq 0.580 \quad (\text{B.22})$$

$$= 752 - 315\lambda + 11.4\lambda^2 \text{ for } 0.580 < \lambda \leq 1.19 \quad (\text{B.23})$$

$$= \frac{462}{\lambda^{0.88}} \text{ for } 1.19 < \lambda \leq 5.25 \quad (\text{B.24})$$

$$= \frac{434}{\lambda^{0.842}} \text{ for } 5.25 < \lambda \leq 37.6 \quad (\text{B.25})$$

Given the values of ΔP_{min} and I^- , the negative phase duration can be calculated to conserve the negative phase impulse:

$$t_d^-(\lambda) = \frac{16}{9} \frac{I^-(\lambda)}{\Delta P_{min}(\lambda)} \quad (\text{B.26})$$

Unlike TNT or other high explosives which are designed specifically to produce a highly efficient explosion, the dispersed vapor cloud even under the most favorable conditions will be relatively inefficient. A study of over one hundred vapor cloud explosions which have occurred in recent years led to the graph shown on Figure B.1, which indicates the relative frequency of occurrence of values of the efficiency (and the TNT equivalent, assuming an energy ratio equal to 10) of these explosive events. As the Figure indicates, efficiencies of three to four percent are most

common, while an efficiency range of one to ten percent accounts for a significant percentage of the explosions studied.

Another important factor in defining the efficiency and the equivalent yield parameters is related to the percentage of the total released material which should be included in the calculation. If the vapor cloud is dispersed extensively before ignition occurs, then some of the vapor is diluted below the lower flammable limit, and some, near the source of the release, may be above the upper flammable limits. Therefore, only that portion of the vapor cloud within these limits will be within the flammable range.

Historically, the estimates of UVCE efficiencies, such as those shown on the figure, have been based on the total mass released. Obviously, for most, if not all, of these events, the calculated efficiency would increase if the mass of the flammable cloud were used in the calculation, and it is likely the wide scatter of efficiency values shown in Figure B.1 is at least partly explained by the wide ratio of the actual flammable mass to the total released mass of these events.

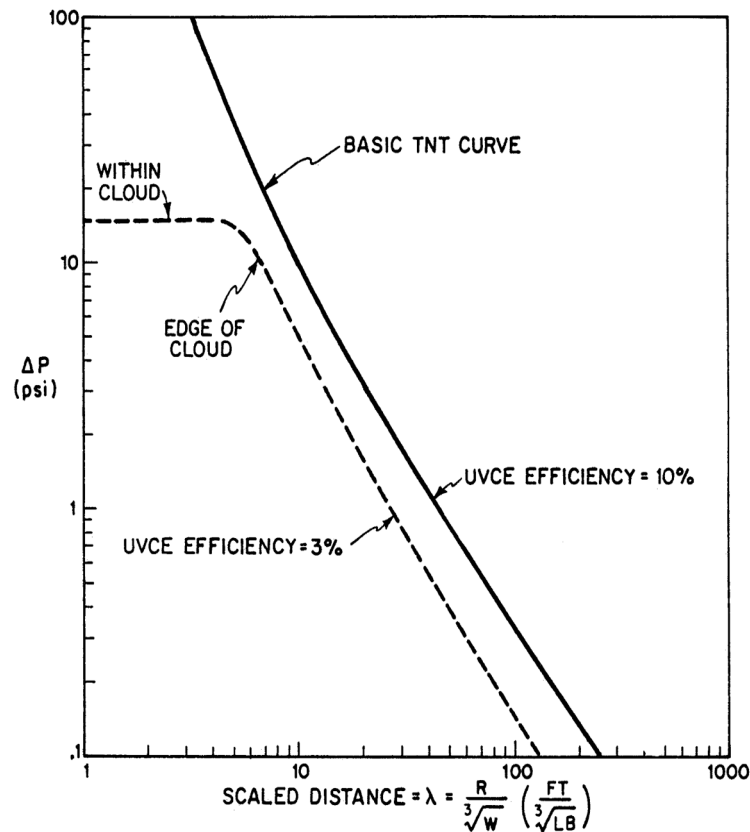
Although it would be preferable to estimate explosion efficiencies on the basis of the flammable mass, such a process introduces still another assumption into the calculations, since for most accidental releases, the total amount released is more readily estimated than the amount in the flammable range.

As the methods and models available for dispersion analyses improve, and thus the estimation of the flammable mass of a hydrocarbon release becomes more accurate, then consideration should be given to developing estimates of the UVCE efficiency on the flammable mass.

The basic *TNT* curve relating the peak overpressure of the blast wave from a *TNT* explosion to the scaled distance parameter, in accordance with the Hopkinson scaling, is shown on both Figures B.3 and B.4. This curve is based on a series of experiments and weapons tests carried out over many years, and represents the peak overpressure, for a *TNT* explosion on the ground surface, which generates an overpressure blast wave which radiates into a hemispherical space.

Little is known about the peak overpressure (or, of the entire time-history) resulting from vapor cloud explosions. Based on explosion damage analyses together with some small-scale experiments and theoretical analysis, it is thought that the corresponding curve for vapor cloud explosions is approximately similar to the basic *TNT* curve with the following exceptions:

1. Within the vapor cloud, it is considered likely by many investigators that the peak overpressure does not exceed 15 psi. At the edge of the cloud, the overpressure is likely to be 10 psi or somewhat less.
2. Outside the cloud, the decay in overpressure is assumed to follow generally the trend indicated for the basic *TNT* curve. On Figure B.3, a decay curve is shown for a vapor cloud efficiency of three percent, a value frequently assumed for design and analysis. On Figure B.4, a curve for ten percent efficiency is shown; this curve is superimposed on the *TNT* curve, on the basis that the ratio of the total energies of the hydrocarbon vapor cloud and an equal weight of *TNT* is ten.
3. In the far-field, with peak overpressures of, say, 0.5 psi or less, it is considered likely that the vapor cloud overpressures decay less rapidly than the *TNT* overpressures. In this region,

Figure B.3: Free-field overpressure vs. scaled distance: *TNT* and UVCE explosions

the vapor cloud overpressure blast wave behaves more like an acoustic wave, thus decaying by geometric spreading only. The consequence of this is that higher values of overpressures occur from vapor cloud explosions than from *TNT* explosions of equivalent weight at far locations.

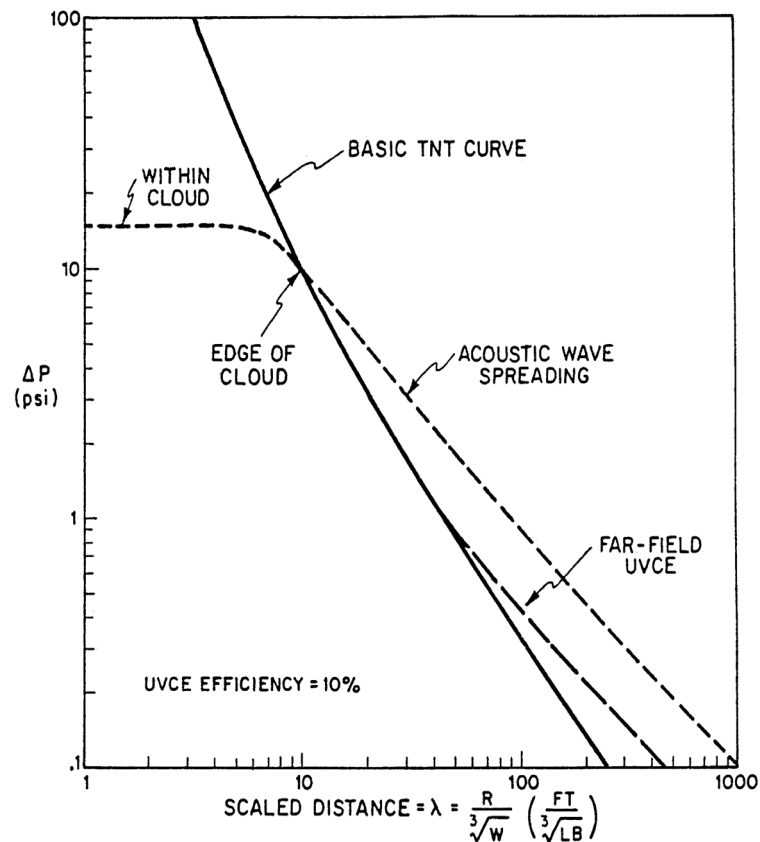
On Figure B.4, acoustic wave spreading is shown for the far-field assumption, for all distances beyond the 1.0 psi overpressure, and, for comparative purposes, for the case where the overpressure decay is only due to acoustic-type spreading losses at all locations outside the cloud itself.

The difference between *TNT* curve decay and acoustic-type decay in the far-field is significant in damage analyses. For example, a 0.2 psi damage estimate (say, by window damage analysis) at a range of 5000 feet implies a equivalent charge of 20 tons if the *TNT* curve is used, and an equivalent charge of less than 5 tons if the acoustic decay curve is used.

Thus the manner in which the peak overpressure of the blast wave from a UVCE decays with distance, particularly in the far-field, is important when far-field locations are used in damage analyses.

Unfortunately, the decay characteristics are not well understood in this region, and the usual analysis methodology is to assume that the *TNT* curve applies. As indicated by the examples, however, this approach can significantly underestimate damage in the far-field, or, alternatively, lead to ex-

Figure B.4: Free field overpressure vs. scaled distance for different spreading assumptions



cessive estimates of equivalent yields from specific damage.

With the substantial uncertainties of the characteristics of the peak overpressure from a vapor cloud explosion both at close-in ranges (greater than 10 psi) and at far-field ranges (less than 0.5 psi), the most useful comparison of vapor cloud explosions and *TNT* explosions are at mid distances, corresponding to, 0.5 psi up to 10 psi with the least uncertainty in the narrower range of about 0.5 psi to 3 psi. It is in this range that damage analysis is considered most appropriate for estimating the source strength of a vapor cloud explosion.

8. *TNO's* Shock Wave Model

Another simple model for the estimation of overpressure for unconfined vapor cloud explosions is the model proposed by Wiekema [18]. The cloud is assumed to hemispherical, homogenous in composition and centrally ignited. The formation of the shock wave is caused by expansion of the cloud following due the energy addition by combustion. The energy addition rate, i.e. the expansion rate, is a function of the flame speed. Wiekema [18] proposes a relationship for the peak

Table B.1: Constants for Wiekema's explosion model

| Flame Speed (m/s) | $c_0 \times 10^2$ | c_1 |
|-------------------|-------------------|-------|
| 40 | 2 | -1 |
| 80 | 6 | -1 |
| 160 | 15 | -1 |

overpressure as a function of flame speed:

$$\frac{\Delta P}{P_0} = c_0 \left[\frac{r}{L_0} \right]^{c_1} \quad (\text{B.27})$$

where, r is the distance from the center of the cloud, and L_0 is a characteristic explosion length given by:

$$L_0 = \left[\frac{V_0 E_c}{P_0} \right]^{1/3} \quad (\text{B.28})$$

E_c is combustion energy per unit volume. Table B.1 summarizes the values of the constants c_0 and c_1 for deflagrations.

For detonations similar semi-empirical equations are proposed:

$$\frac{\Delta P}{P_0} = 0.518 \left[\frac{r}{L_0} \right]^{-1.7} \quad \text{for } 0.29 < \frac{r}{L_0} < 1.088 \quad (\text{B.29})$$

and for $\frac{r}{L_0} \geq 1.088$

$$\frac{\Delta P}{P_0} = 0.2177 \left[\frac{r}{L_0} \right]^{-1} + 0.1841 \left[\frac{r}{L_0} \right]^{-2} + 0.1194 \left[\frac{r}{L_0} \right]^{-3} \quad (\text{B.30})$$

9. TNO Multi-Energy

[49] Despite many fundamental objections [50], *TNT*-equivalency methods are widely used for simple vapor cloud explosion blast modeling. Presently, however, almost 15 years after its formulation, the *TNO* Multi-Energy method is increasingly accepted as a more reasonable alternative [51]. The Multi-Energy concept is based on the starting point that, assuming deflagrative combustion, the explosive potential of a vapor cloud is primarily determined by only the obstructed and/or partially confined areas in the cloud. Separate areas produce separate blasts. So, contradictory to more conventional methods, in which a vapor cloud explosion is regarded as an entity, according to the Multi-Energy concept a vapor cloud explosion is rather defined as a number of sub-explosions corresponding with the various partially confined, obstructed areas in the cloud.

The Multi-Energy concept, derived by simple reasoning, was confirmed by experimental observations (see [52, 53, 49, 54]).

Applying the Multi-Energy method, a blast should be modeled by the specification of an equivalent hemi-spherical fuel-air charge, which has two characteristics, namely:

- A charge size, which is directly related to the heat of combustion of the flammable mixture actually contributing to the blast, and
- A charge strength which is defined as the maximum explosion overpressure produced.

According to *TNO* recommendations, the charge characteristics can be specified following a simple safe and conservative approach, namely:

- The charge energy should be taken equal to the full heat of combustion of the flammable mixture present within the partially confined, obstructed area in the cloud, assuming that the fuel is stoichiometrically mixed with air.
- The charge strength is assumed to be maximum.
- If the assumption of maximum strength results in unacceptable overestimates of blast effects, the approach may be refined on the basis of correlation with experimental data. To this end, a data base is being developed in the form of graphs (see [55]). The data base is accessible through evaluating a combination of parameters. This parameter combination characterizes the major initial and boundary conditions which largely determine the development of gas explosions.

Having specified the fuel-air charge energy and strength, the blast wave's side-on overpressure and duration at any distance from the charge can be read from fuel-air blast charts shown in Figures B.5 and B.6.

The charts are fully non-dimensionalized with atmospheric overpressure P_o , the charge heat of combustion E and the ambient speed of sound c_o . The blast charts have been compiled for a heat of combustion $H_c = 3.5 \text{ MJ/m}^3$, which is an average value which approximately holds for the most common stoichiometric hydrocarbon-air mixtures.

10. The Baker-Strehlow Method

The original form of the Baker-Strehlow method was published by Baker et al. in 1983 [56]. Baker, et al. developed a method for utilizing a series of curves generated by Strehlow [57] during numerical studies to analyze the structure of blast waves generated by both constant-velocity and accelerating flames propagating in a spherical geometry [58]. Baker's work included a comparison of Strehlow's curves to available experimental data.

The curves published by Strehlow in 1979 relating scaled overpressure and scaled impulse to scaled distance are shown in Figures B.7 and B.8.

Figure B.5: Dimensionless positive phase duration vs. combustion energy scaled distance

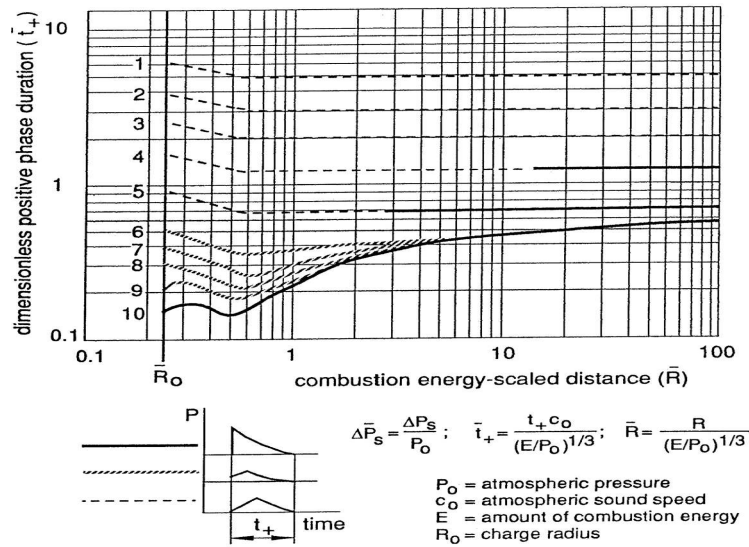


Figure B.6: Dimensionless maximum "side on" overpressure as a function of combustion energy scaled distance

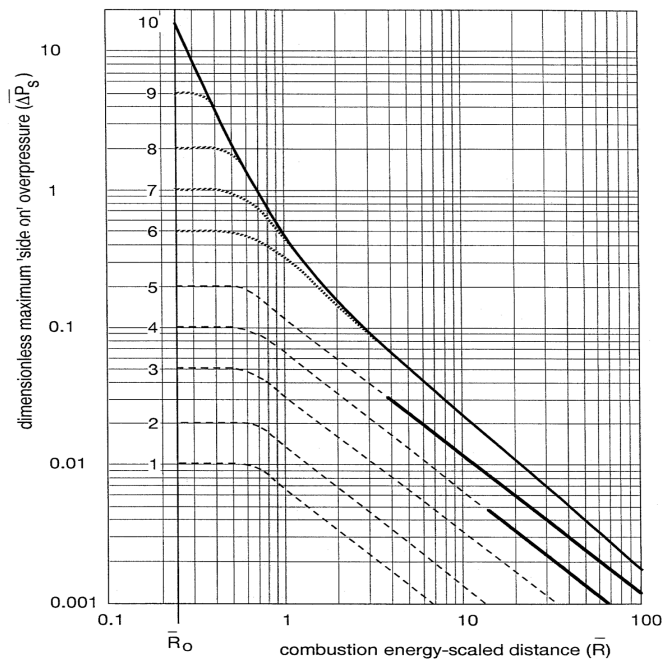
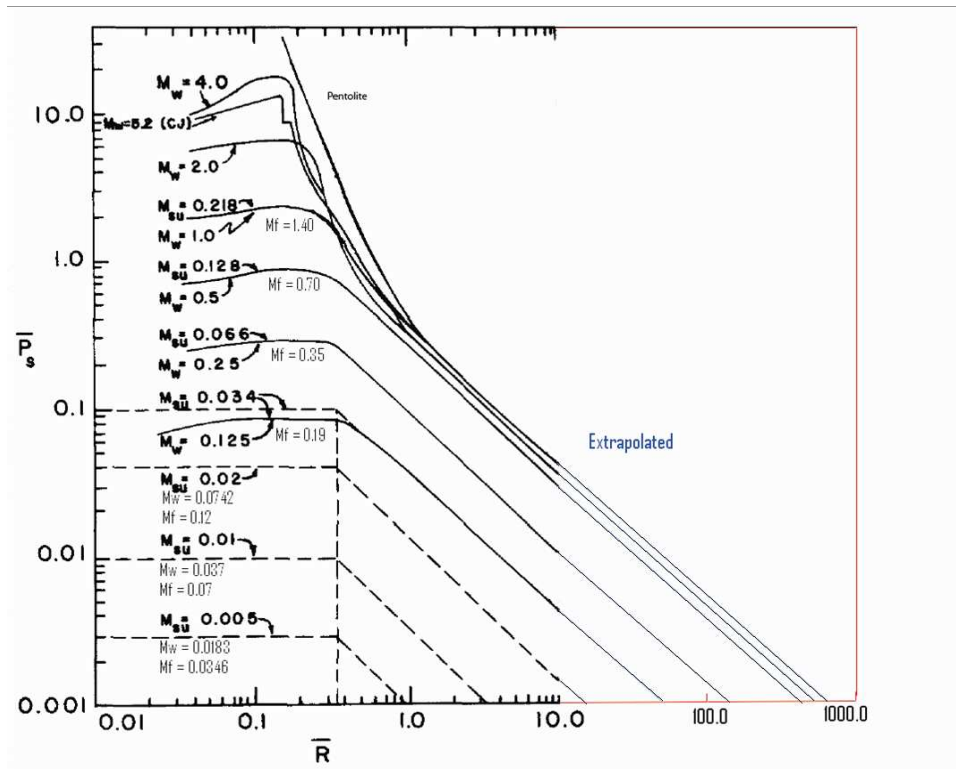


Figure B.7: Original Strehlow Curves of Scaled Overpressure vs. Scaled Distance



The scaled overpressure, P_s , is defined as:

$$\bar{P}_s = \frac{P_{max} - P_o}{P_o}$$

P_o is the ambient atmospheric pressure in Pascal, and P_{max} is the maximum value of explosion pressure (in Pascal) observed in the field at a specific scaled distance R . The scaled distance R is given by the following formula:

$$\bar{R} = \frac{r P_o^{1/3}}{E^{1/3}}$$

Note that r is the radial distance from a specific receptor to the center of vapor cloud (m), and E is the total explosion combustion energy given by:

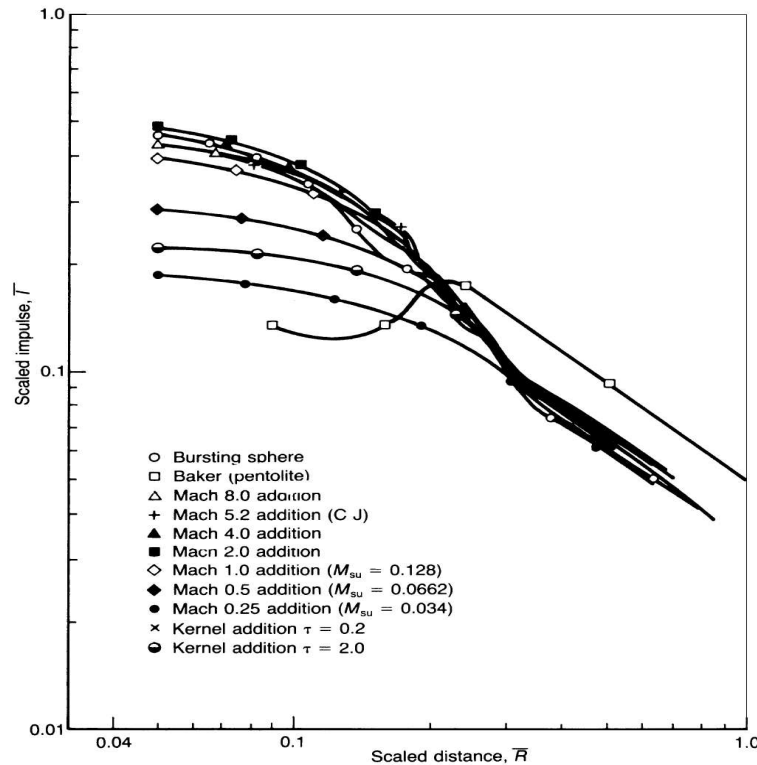
$$E = m_{expl} h_f$$

m_{expl} is the mass of fuel above the lower flammable limits. m_{expl} includes mass above the upper flammable limit which is assumed to be diluted to within the flammable limits by the explosion and then consumed.

The dimensionless scaled impulse is given by

$$\bar{i}_s = \frac{i a_o}{P_o^{2/3} E^{1/3}}$$

Figure B.8: Original Strehlow Curves of Scaled Impulse vs. Scaled Distance



I is the incident impulse (Pa.s), and a_0 is the speed of sound in air at ambient conditions (m/s).

The original Baker-Strehlow curves were labeled in terms of M_{su} and M_w (See Figure B.7). M_{su} is the flame Mach number relative to the moving gas ahead of the flame. M_w refers to the velocity of heat addition in Strehlow's numerical calculations in a Lagrangian coordinate system. It is more practical and less confusing to label the curves in terms of M_f , the apparent flame Mach number relative to a fixed observer, i.e. the actual flame speed S_f (see Tang and Baker).

$$M_f = \frac{S_f}{a_0}$$

For supersonic combustion, $M_f = M_w$. For subsonic combustion M_f , M_{su} , and M_w are related using the following expression:

$$M_f = \frac{\rho_u}{\rho_b} M_{su} = \left[\frac{\rho_u}{\rho_b} \right]^{1/3} M_w \quad (\text{B.31})$$

$$M_{su} = \left[\frac{\rho_u}{\rho_b} \right]^{2/3} M_w \quad (\text{B.32})$$

Where ρ_b is the fuel density behind the flame (burnt) and ρ_u is the fuel density ahead of the flame (unburnt). The ratio of burnt to unburnt fuel densities ρ_b/ρ_u is referred to as the expansion ratio.

The maximum flame speed S_f (m/s) that can be attained in the given vapor cloud explosion is a critical input into any analysis using the Baker-Strehlow method.

Experimental work has demonstrated that flame speed and turbulence are strongly dependent upon, among other factors, fuel reactivity, fuel composition, the presence and distribution of obstacles to flow, and confinement configuration.

Baker et al. [59, 5, 60] established the following guidelines to relate fuel reactivity, release geometry, and obstacle density and confinement to the maximum explosion flame speed for soft ignition sources (see Table B.2).

Table B.2: Guidelines for Establishing Apparent Flame Mach number M_f

| 1D Flame Expansion Case | | Obstacle Density | | |
|---------------------------|--------|------------------|--------|-------|
| | | High | Medium | Low |
| Reactivity | High | 5.2 | 5.2 | 5.2 |
| | Medium | 2.27 | 1.77 | 1.03 |
| | Low | 2.27 | 1.03 | 0.294 |
| 2D Flame Expansion Case | | Obstacle Density | | |
| | | High | Medium | Low |
| Reactivity | High | DDT ^a | DDT | 0.59 |
| | Medium | 1.6 | 0.66 | 0.47 |
| | Low | 0.66 | 0.47 | 0.079 |
| 2.5D Flame Expansion Case | | Obstacle Density | | |
| | | High | Medium | Low |
| Reactivity | High | DDT | DDT | 0.47 |
| | Medium | 1.0 | 0.55 | 0.29 |
| | Low | 0.50 | 0.35 | 0.053 |
| 3D Flame Expansion Case | | Obstacle Density | | |
| | | High | Medium | Low |
| Reactivity | High | DDT | DDT | 0.36 |
| | Medium | 0.50 | 0.44 | 0.11 |
| | Low | 0.34 | 0.23 | 0.026 |


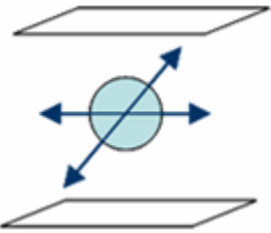
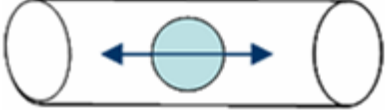
^aDDT = Deflagration to detonation transition

For a 3D symmetry (see Table B.2), the flame is free to expand spherically from a point ignition source. The overall flame surface increases with the square of the distance from the point ignition source. The flame induced flow field can decay freely in three directions. Therefore, flow velocities are low, and the flow field disturbances by obstacles are small.

In 2D symmetry, that is, a cylindrical flame between two plates, the overall flame surface area is proportional to the distance from the ignition point. Consequently, wrinkling of the flame surface will have a stronger effect than in the point-symmetry case.

The 2.5D symmetry was adopted for situations in which there is some form of confinement (see Table B.2) that is more restrictive than 3D but does not merit a 2D rating. A common situation where this applies is a light weight or low strength roof that creates 2D confinement, but the roof blows off during the explosion creating a vent. It is very common to find compressor shelters with a

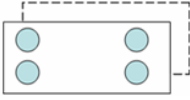
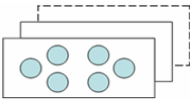
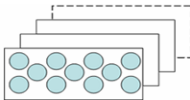
Table B.3: Guidelines for Establishing Flame Geometry

| Dimension | Description | Geometry |
|-----------|---|--|
| 3D | “Unconfined volume,” almost completely free expansion |  |
| 2.5D | Compressor shelters with lightweight roofs; dense pipe racks | Between 3-D and 2-D |
| 2D | Platforms carrying process equipment; space beneath cars; open-sided multistory buildings |  |
| 1D | Tunnels, corridors, or sewage systems |  |

light roof that provides weather protection for maintenance. Another situation where 2.5D applies is a plane of very high congestion or a plane with partial 2D confinement. An example of this situation is a pipe rack with such a dense layer of pipes that 3D confinement is not conservative.

1D configuration is rarely encountered in actual plants. In 1D symmetry, for example, a planar flame in a tube, the projected flame surface area is constant. There is hardly any flow field decay, and flame deformation has a very strong effect on flame acceleration.

Table B.4: Guidelines for Establishing Confinement Level

| Type | Obstacle Blockage Ratio per Plane | Pitch for Obstacle Layers | Geometry |
|--------|-----------------------------------|---|---|
| Low | Less than 10% | One or two layers of obstacles |  |
| Medium | Between 10% and 40% | Two to three layers of obstacles |  |
| High | Greater than 40% | Three or more fairly closely spaced obstacle layers |  |

Reactivity is classified as low, medium, and high (see *TNO* shock wave model). Methane and carbon monoxide are the only materials defined to have low reactivity. Hydrogen, acetylene, ethylene, ethylene oxide, propylene oxide are defined to have high reactivity.

Materials burning in oxygen enriched atmospheres should be classified as highly reactive unless proven otherwise by actual measurements.

It has been suggested by others that the chemical reactivity classification should be based on the value of the fundamental laminar burning velocity (see Table B.5). Note that the laminar burning velocity will be much larger in oxygen atmosphere than air for a typical hydrocarbon. The burning velocity data in Table B.5 is obtained from NFPA-68. The laminar burning velocity of a mixture can be obtained from the following equation:

$$\frac{1}{S_{l,mix}} = \sum_i \frac{y_i}{S_{l,i}} \quad (\text{B.33})$$

where y_i is the volume or mole fraction of component i in the mixture.

Table B.5: Explosion chemical reactivity classification based on fundamental laminar burning velocity

| Chemical | CAS | S_L , m/s | Reactivity |
|------------------------------|----------|-------------|------------|
| HYDROGEN | 1333740 | 3.12 | High |
| ACETYLENE | 74862 | 1.66 | High |
| ETHYLENE OXIDE | 75218 | 1.08 | High |
| VINYLACETYLENE | 689974 | 0.89 | High |
| PROPADIENE | 463490 | 0.87 | High |
| 1-PROPYNE | 74997 | 0.82 | High |
| PROPYLENE OXIDE | 75569 | 0.82 | High |
| ETHYLENE | 74851 | 0.8 | High |
| SPIROPENTANE | 157404 | 0.71 | Medium |
| ETHYLACETYLENE | 107006 | 0.68 | Medium |
| 1,2-BUTADIENE | 590192 | 0.68 | Medium |
| CYCLOBUTANE | 287230 | 0.67 | Medium |
| ACROLEIN | 107028 | 0.66 | Medium |
| 1,3-BUTADIENE | 106990 | 0.64 | Medium |
| 1-PENTYNE | 627190 | 0.63 | Medium |
| METHYLENE | 2465567 | 0.61 | Medium |
| DIMETHYLACETYLENE | 503173 | 0.61 | Medium |
| 1,2-PENTADIENE | 591957 | 0.61 | Medium |
| 2-PENTYNE | 627214 | 0.61 | Medium |
| 2,3-PENTADIENE | 591968 | 0.6 | Medium |
| n-PROPIONALDEHYDE | 123386 | 0.58 | Medium |
| METHYLCYCLOPROPANE | 594116 | 0.58 | Medium |
| CARBON DISULFIDE | 75150 | 0.58 | Medium |
| 1-HEXYNE | 693027 | 0.57 | Medium |
| ETHYLCYCLOPROPANE | 1191964 | 0.56 | Medium |
| METHANOL | 67561 | 0.56 | Medium |
| CYCLOPROPANE | 75194 | 0.56 | Medium |
| 3,3-DIMETHYL-1-BUTYNE | 917920 | 0.56 | Medium |
| cis-1,3-PENTADIENE | 1574410 | 0.55 | Medium |
| cis-1,2-DIMETHYLCYCLOPROPANE | 2402064 | 0.55 | Medium |
| 1,4-PENTADIENE | 591935 | 0.55 | Medium |
| ISOPRENE | 78795 | 0.55 | Medium |
| cis-1,2-DIMETHYLCYCLOPROPANE | 930187 | 0.55 | Medium |
| DIMETHYL ETHER | 115106 | 0.54 | Medium |
| trans-1,3-PENTADIENE | 2004708 | 0.54 | Medium |
| 4-METHYL-2-PENTYNE | 21020279 | 0.54 | Medium |
| ACETONE | 67641 | 0.54 | Medium |
| ETHYLCYCLOBUTANE | 4806615 | 0.53 | Medium |
| 4-METHYL-1-PENTYNE | 7154758 | 0.53 | Medium |
| 3-HEXYNE | 928494 | 0.53 | Medium |

Table B.5: Explosion chemical reactivity classification based on fundamental laminar burning velocity (continued)

| Chemical | CAS | S_L , m/s | Reactivity |
|-----------------------------|---------|-------------|------------|
| 1,1,2-TRIMETHYLCYCLOPROPANE | 4127451 | 0.52 | Medium |
| 2,3-DIMETHYL-1,3-BUTADIENE | 513815 | 0.52 | Medium |
| 1,5-HEXADIENE | 592427 | 0.52 | Medium |
| METHYLCYCLOBUTANE | 598618 | 0.52 | Medium |
| 1-BUTENE | 106989 | 0.51 | Medium |
| cis-2-PENTENE | 627203 | 0.51 | Medium |
| ACRYLONITRILE | 107131 | 0.5 | Medium |
| 1-PENTENE | 109671 | 0.5 | Medium |
| 2-CYCLOPROPYL-PROPANE | 3638355 | 0.5 | Medium |
| 1-HEXENE | 592416 | 0.5 | Medium |
| 3-METHYL-1-BUTENE | 563451 | 0.49 | Medium |
| TETRAHYDROPYRAN | 142687 | 0.48 | Medium |
| 4-METHYL-1-PENTENE | 691372 | 0.48 | Medium |
| BENZENE | 71432 | 0.48 | Medium |
| DIETHYL ETHER | 60297 | 0.47 | Medium |
| ETHANE | 74840 | 0.47 | Medium |
| 2-METHYL-1-PENTENE | 763291 | 0.47 | Medium |
| n-PENTANE | 109660 | 0.46 | Medium |
| n-HEXANE | 110543 | 0.46 | Medium |
| CYCLOHEXANE | 110827 | 0.46 | Medium |
| 2-METHYL-1,3-PENTADIENE | 1118587 | 0.46 | Medium |
| n-HEPTANE | 142825 | 0.46 | Medium |
| ETHYLENEIMINE | 151564 | 0.46 | Medium |
| CYCLOPENTADIENE | 542927 | 0.46 | Medium |
| 2-METHYL-1-BUTENE | 563462 | 0.46 | Medium |
| 2,3-DIMETHYL-1-BUTENE | 563780 | 0.46 | Medium |
| CARBON MONOXIDE | 630080 | 0.46 | Medium |
| PROPANE | 74986 | 0.46 | Medium |
| 2-ETHYL-1-BUTENE | 760214 | 0.46 | Medium |
| ISOPROPYLCYCLOBUTANE | 872560 | 0.46 | Medium |
| n-BUTANE | 106978 | 0.45 | Medium |
| METHYLCYCLOHEXANE | 108872 | 0.44 | Low |
| CYCLOPENTANE | 287923 | 0.44 | Low |
| n-HEXADECANE | 544763 | 0.44 | Low |
| 2,3-DIMETHYL-2-BUTENE | 563791 | 0.44 | Low |
| 1-DECENE | 872059 | 0.44 | Low |
| 2-METHYLPENTANE | 107835 | 0.43 | Low |
| n-DECANE | 124185 | 0.43 | Low |
| 2,3-DIMETHYLPENTANE | 565593 | 0.43 | Low |
| 2-METHYLBUTANE | 78784 | 0.43 | Low |
| 2,3-DIMETHYLBUTANE | 79298 | 0.43 | Low |

Table B.5: Explosion chemical reactivity classification based on fundamental laminar burning velocity (continued)

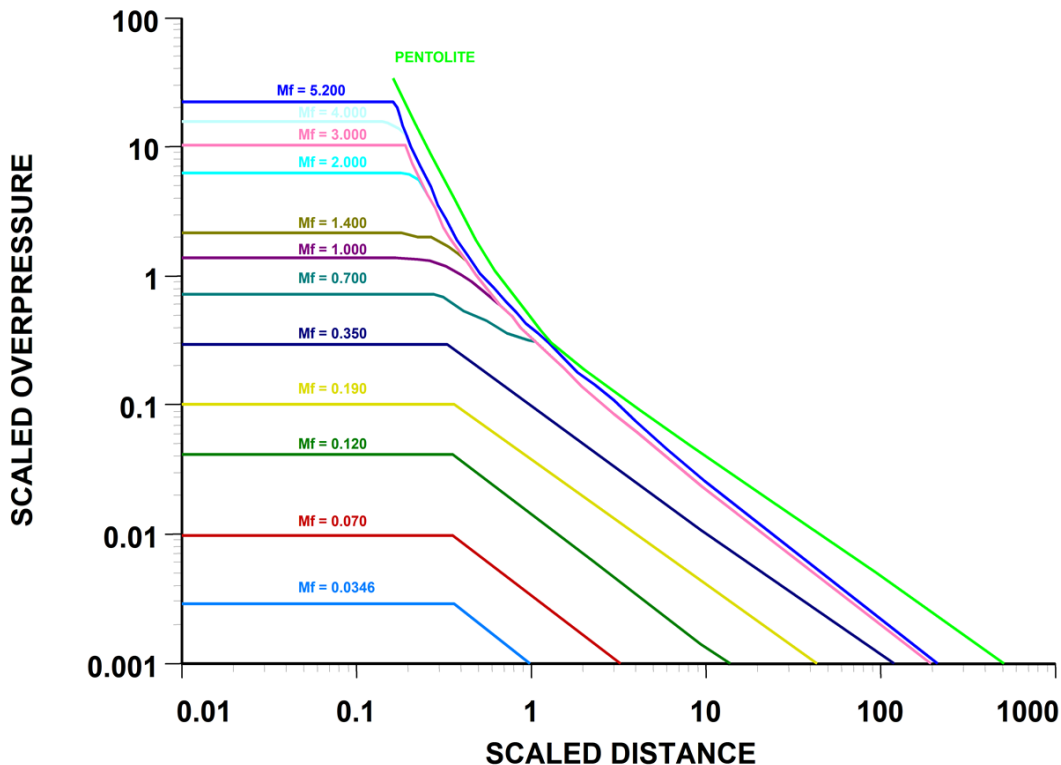
| Chemical | CAS | S_L , m/s | Reactivity |
|------------------------|--------|-------------|------------|
| 3-METHYLPENTANE | 96140 | 0.43 | Low |
| 2,4-DIMETHYLPENTANE | 108087 | 0.42 | Low |
| 2,2,3-TRIMETHYLBUTANE | 464062 | 0.42 | Low |
| 2,2-DIMETHYLBUTANE | 75832 | 0.42 | Low |
| BUTANONE | 78933 | 0.42 | Low |
| METHYLCYCLOPENTANE | 96377 | 0.42 | Low |
| TOLUENE | 108883 | 0.41 | Low |
| 2,2,4-TRIMETHYLPENTANE | 540841 | 0.41 | Low |
| 2,2-DIMETHYLPENTANE | 590352 | 0.41 | Low |
| ISOPROPANOL | 67630 | 0.41 | Low |
| 2-METHYLPROPANE | 75285 | 0.41 | Low |
| n-OCTANE | 111659 | 0.4 | Low |
| METHANE | 74828 | 0.4 | Low |
| TETRALIN | 119642 | 0.39 | Low |
| 2,2-DIMETHYLPROPANE | 463821 | 0.39 | Low |
| 1,2,4-TRIMETHYLBENZENE | 95636 | 0.39 | Low |
| tert-BUTYLBENZENE | 98066 | 0.39 | Low |
| ETHYL ACETATE | 141786 | 0.38 | Low |
| n-BUTYLBENZENE | 104518 | 0.37 | Low |
| 1,2-DIMETHYLBENZENE | 95476 | 0.37 | Low |
| trans-DECALIN | 493027 | 0.36 | Low |
| DIPHENYLMETHANE | 101815 | 0.35 | Low |
| ISOPROPYLAMINE | 75310 | 0.31 | Low |
| 1,1-DIFLUOROETHANE | 75376 | 0.236 | Low |
| 1,1,2-TRIFLUOROETHANE | 430660 | 0.131 | Low |
| 1,1,1-TRIFLUOROETHANE | 420462 | 0.071 | Low |
| DIFLUOROMETHANE | 75105 | 0.067 | Low |

The work of Strehlow, upon which the scaled curves shown in Figure B.7 and Figure B.8 were derived, considered flame speeds ranging from low velocity deflagrations to detonations. Furthermore the numerical calculations were carried out for durations extending long beyond the time at which the flame had extinguished and yielded blast parameters in the far field from the explosion source. Therefore it is reasonable to apply the Baker-Strehlow method in the near field, i.e., inside the combustion zone as well as in the far field or well beyond the detonation site. This versatility offers a marked advantage over the *TNT*-equivalency method in which gas explosions or far-field blast overpressure waves are poorly modeled. Note that the curves were established for typical hydrocarbons with a density expansion ratio around 7 and a heat capacity ratio of 1.4. The Baker-Strehlow method is very similar in concept to the *TNO* multi energy method.

Tang et al. proposed an update of the original Strehlow curves where they changed the slope of the blast pressure decay curves. These modifications are shown in Figures B.9 and B.10. The Tang et

al. modifications result in significant hazard zones reductions for supersonic flames in the far field. These modifications are adopted in the Baker-Strehlow model used in SuperChems Expert.

Figure B.9: Scaled Overpressure vs. Scaled Distance Curves Used in SuperChems Expert



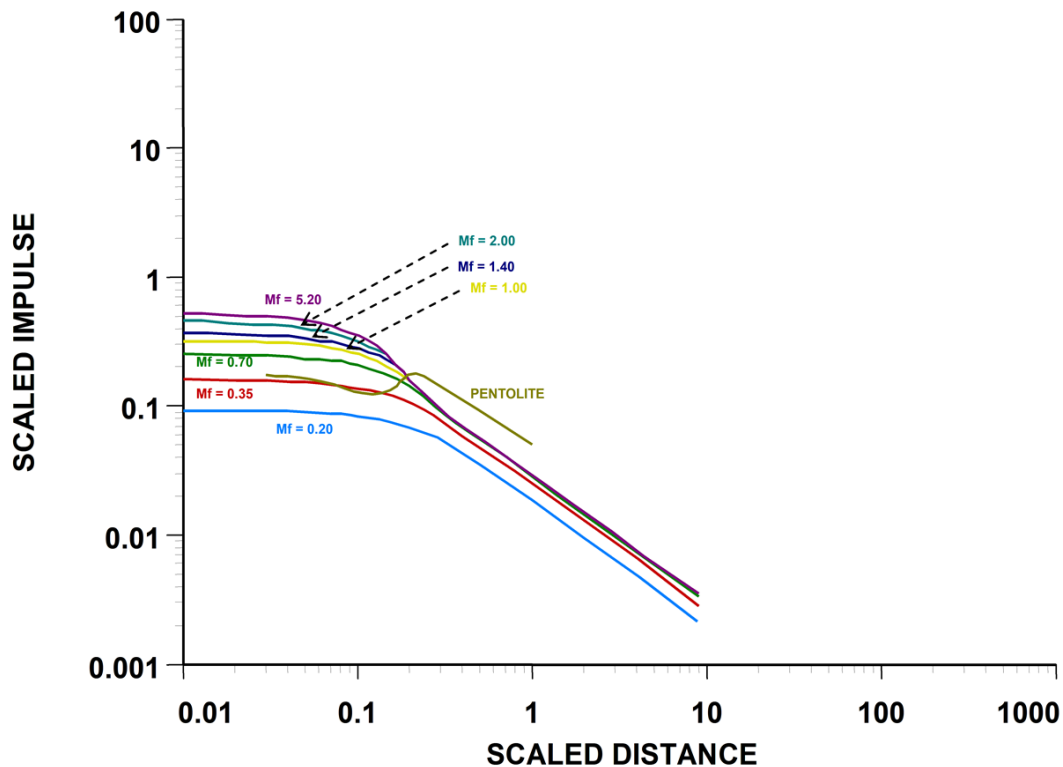
One disadvantage of the Baker-Strehlow method in contrast to other methods for the estimation of explosion overpressure is that accurate results depend on obtaining good estimates of the flame propagation speed for a particular combination of confinement, obstacles, fuel reactivity, and ignition sources.

Although some useful guidelines now exist (see Table B.2), it is to be expected that in many cases it will be difficult to assess an appropriate value of the flame speed without the aid of sophisticated computational techniques (which obviates the usefulness of a simple model such as Baker-Strehlow).

Furthermore, there is some subjectivity involved when calculating the energy term E representing the sensible heat released by the portion of a vapor cloud that undergoes detonation. The CCPS guidelines handbook (1994), for instance, describes 3 alternative methods for determining E based on the level of confinements and the characteristics of the vapor release. Each of these methods will likely yield significantly different values for E in most cases.

In general, we recommend the use of the Baker-Strehlow method for the estimation of overpressure in both the near and far field for vapor cloud explosions.

Figure B.10: Scaled Impulse vs. Scaled Distance Curves Used in SuperChems Expert



11. Detonation Analysis

Detonation is the most hazardous type of UVCE. A detonation in a stoichiometric gas-phase fuel-air mixture is a supersonic wave propagating with a detonation velocity between 1800-2400 m/s. The velocity depends on the exact composition (see Table B.6), and is experimentally observed to be between 90 and 100 % of the classical value predicted by the Chapman-Jouguet (CJ) theory. The peak (CJ) pressure behind the detonation is approximately 20-30 bars and an expansion wave directly follows the detonation, reducing the pressure to near atmospheric in a time comparable to the sound wave transit time through the burned gas, typically about 1 ms per meter of cloud thickness.

In the far field, the blast wave produced by a detonating vapor cloud has been experimentally demonstrated (Moen et al. [61]) to be identical to that produced by the equivalent mass of high explosive. In the near field, particularly within the cloud, the peak overpressure is lower for the vapor cloud but the pressure pulse duration is much longer than for an equivalent energy high explosive blast. The differences in near field characteristics of vapor cloud and high explosive detonation result in a failure of the energy equivalence concept for near field damage. In particular, the near field positive-phase impulse is much larger for a vapor cloud detonation than the equivalent high explosive blast. This leads to much larger near field damage than would be predicted on the basis of the energy deduced from far field observations.

Table B.6: Detonation Parameters of Common Fuels-Air Systems

| Chemical | % (volume) at $\phi = 1$ | P_{CJ} (bar) | U_{CJ} (m/s) | Δ (mm) | λ (mm) | E_c (kJ) |
|--------------------------------|-----------------------------|-------------------|-------------------|------------------|-------------------|---------------|
| H ₂ | 29.60 | 15.6 | 1968 | 0.29 | 15 | 5.28 |
| CH ₄ | 9.48 | 17.2 | 1801 | 24.00 | 300 | 19.2-105.6 MJ |
| C ₂ H ₂ | 7.75 | 19.1 | 1864 | 0.27 | 6 | 5.76 |
| C ₂ H ₄ | 6.54 | 18.4 | 1822 | 2.60 | 27 | 48-72 |
| C ₂ H ₆ | 5.66 | 18.0 | 1825 | 4.60 | 55 | 144-192 |
| C ₃ H ₆ | 4.46 | 18.5 | 1809 | – | 52 | 216-250 |
| C ₃ H ₈ | 4.03 | 18.3 | 1798 | 4.10 | 55 | 240-384 |
| C ₄ H ₁₀ | 3.13 | 18.4 | 1796 | – | 60 | 240-384 |

12. Reaction Zone Length

A detonation can be idealized as a nonreactive shock wave followed by chemical reaction zone. The high temperatures and densities produced by the strong shock initiates the reaction between fuel and oxygen. Reactions for typical hydrocarbon fuels require many intermediate steps (several hundred) and species (20-50) before the final products of combustion, CO₂ and H₂O are produced. The time or distance required to achieve complete reaction is an indication of the detonation sensitivity of the fuel-air system. A key parameter is the thickness of the reaction zone, Δ , which can be used to rank the sensitivity of many fuels to detonation. The more sensitive the fuel, the smaller Δ . These reaction zone thicknesses can be computed (Westbrook and Urtiew [62]) using detailed chemical reaction network model for many common fuels, some values for common hydrocarbons are listed in Table B.6 together with other important detonation parameters. Note that many of the higher hydrocarbons have similar reaction zone thicknesses and would be expected to have comparable detonation sensitivity. Methane is an exceptional compound and does not follow this rule, it is among the most insensitive of hydrocarbons but can be detonated if sufficient energy is used.

13. Cell Size

Experimentally, the shock wave and reaction zone structure is observed (Lee [63]) to be unstable, resulting in transverse instability waves moving across the detonation wave. The instability waves are quasi-periodic and have a characteristic spacing λ known as the cell size, after the cellular appearance of the spatial structure of the instability wave pattern. The cell size λ and the reaction zone thickness Δ are closely related, for common fuel-air mixtures λ is about 20-50 times Δ (Westbrook and Urtiew [62] Shepherd [64] and [65]). The cell size is also a convenient measure of detonation sensitivity and has the advantage of being experimentally measurable in laboratory-type experiments. Cell sizes have been obtained for many common fuel-air mixtures and are also given in Table B.6.

14. Critical Energy

Extensive experimentation in the last decade, review by Lee [63], has shown that the behavior of detonations can be directly related to the sensitivity to the mixture, as characterized either by Δ or λ . One of the most important relationships for UVCEs is the minimum or critical energy E_c required for direct initiation of detonation. It is found that (Lee [66]) in order to directly initiate detonation, i.e., without a flame acceleration and DDT process occurring, that a large amount of energy must be rapidly (within microseconds) deposited directly within the vapor cloud. Only very rapid energy releases such as from sparks, exploding wires, or high explosives are effective in causing direct initiation. It has been experimentally observed (Bach et al. [67]) that if less than a critical amount of energy is used, detonation will not occur and only a high speed flame will result. The overpressures may be substantial, as in turbulent jet initiation, but a detonation does not occur. Critical energies for direct initiation depend on the fuel type and equivalence ratio and have been experimentally measured for many common fuels. Critical energy values are conventionally given in terms of the equivalent mass of the high explosive tetryl (1 kg of tetryl is equivalent to 4.8 MJ), some data are given for stoichiometric mixtures in Table B.6. Note that for the higher hydrocarbons (except methane), the minimum critical energies are all similar and are of the order of 50 - 80 g of explosive. This magnitude of rapid energy release is essentially impossible to obtain in an accident situation and emphasizes how unlikely direct initiation of detonation is for most UVCEs.

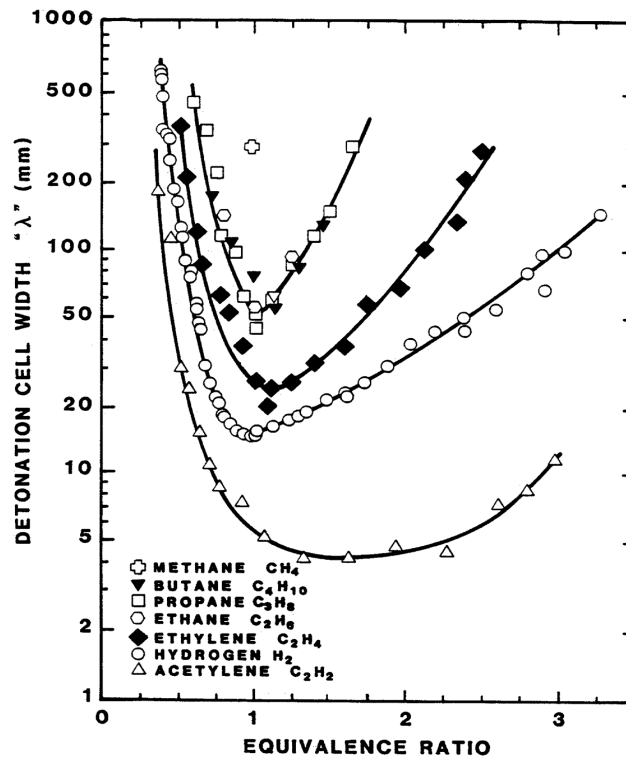
Benedick et al. [68] have shown a direct link between the cell size λ and the minimum critical energy E_c :

$$E_c = 490\rho_0 U_{CJ}^2 \lambda^3 \quad (\text{B.34})$$

where the quantities are E_c (Joules), initial fuel-air density ρ_0 (kg/m^3), the detonation velocity U_{CJ} (m/s), and detonation cell size λ (m). This relation is very useful in predicting E_c values from laboratory measurements of the cell size. The observed proportionality between cell size and reaction zone length enables predictions or extrapolation of E_c values for fuel-air systems in which the chemical kinetics are well understood.

As the equivalence ratio of the mixture departs from stoichiometric, any given mixture will become much more insensitive. This is due to the lower energy release of off-stoichiometric mixtures resulting in lower post-shock temperatures and densities and longer reaction times. The Arrhenius dependence of reaction rate on temperatures and the large effective activation energies of common fuel-air reactions causes a sharp increase in reaction time and reaction zone length as the mixtures varies from stoichiometric. This dependence is reflected in the "U-shaped curves" measured for the dependence of detonation cell size on reaction zone length, shown in Figure B.11. As a consequence, nonuniformity within the vapor cloud and the natural concentration gradient that exists due to the mixing processes during the release make direct initiation of detonation even more difficult. Only that portion of the cloud which is within a concentration range that yields modest increases in cell size over the stoichiometric value will be capable of detonation.

Figure B.11: Fuel-air detonation cell sizes



15. Flame Acceleration Mechanisms and DDT

When flames propagate in obstacle-filled region, the acceleration mechanism is due to the flame-generated flow pulling the flame through the narrow region (throat) at the obstacle locations and the flame is then wrapped up in the vortices shed from the downstream side of the obstacle. The flame shoots out ahead since it is pushed from behind as the pockets of reactants between the obstacles are burned out. In turn, the increase in burning area results in a greater volume flow rate out of the burned region. This pushes the unburned reactants over the obstacles faster, producing more vorticity and setting up a positive feedback mechanism between fluid motion and the flame motion. This is particularly effective in closed tubes (Lee [63]) but will also result in flame acceleration in unconfined but obstructed regions, as discussed previously in the literature review. If the flame speeds and fluctuating velocities become large enough ahead of the flame, then significant pressure fluctuations can occur. These pressure fluctuations will also feed back in the flame propagation process and provide another mechanism for acceleration.

If the flame acceleration process proceeds to a sufficiently high level, it is possible for a sudden transition to detonation to occur. The ability to promote flame acceleration and the tendency for DDT is a function of the several factors (Lee [34]): the reaction and transport rates in the mixture; confinement; obstacle geometry. The following parameters are found to be important:

1. laminar flame propagation velocity,

2. detonation cell size (reaction zone thickness,
3. obstructed area ratio, and
4. minimum transverse dimension of the obstacles or tube.

These factors appear to be significant for both confined and unconfined explosions. The onset of DDT has been observed to be correlated with the sensitivity of the mixture and the minimum size of the orifices within the tube.

Transition to detonation is found (Knystatus et al. [69], Peraldi et al. [70]) to be possible if the detonation cell size λ is less than the minimum transverse dimension in the system D_m . In the case of an unconfined cloud, this dimension is the minimum thickness of the cloud. While the data are inconclusive, a thickness of 3-6 λ appears to be required.

Numerical modeling of DDT has been directed at understanding the flame acceleration portion of the process. No method has been developed yet that is capable of accurately predicting a complete flame acceleration and transition to detonation event. Hazard assessment for DDT events therefore proceeds by a combination of experiment, partial numerical modeling, and judgment. Two principal types of numerical models have been applied to this problem: inviscid, incompressible vortex dynamics and flame front tracking (Barr [71], Cattolica et al. [72], Barr [73], Lee et al. [63]); finite-difference, compressible flow with k - ϵ turbulence models and mixing-rate limited chemistry (Hjertager [74], Hjertager [75], Marx [76]). Each scheme has its peculiar merits and deficiencies. Comparisons with experiments indicate that the initial stages of flame acceleration can be predicted successfully by either model. Details of the flame-vortex interaction process are well resolved by the vortex dynamics technique. The compressible flow models are successful in predicting the pressure waves produced by high-speed flames in partially confined and obstructed tubes. However, the actual onset of detonation can not be treated by the present models. This problem is due in large measure to the practical limitations on spatial and temporal resolution in multidimensional computations. However, in current models, a key difficulty also lies in the combustion submodel: it is simply not possible to simulate details of reaction zones (needed for detonation onset modeling) with the current subgrid-scale models of turbulent combustion.

16. Detonation Potential of UVCE's

Completely unconfined and unobstructed vapor clouds ignited by low-energy sources burn through a low-speed turbulent flame mechanism that results in small blast pressures. In order to produce substantial blast waves and associated far-field damage, high-speed deflagrations or detonations must occur. High-speed deflagrations can be produced if the cloud is partially obstructed by obstacles such as pipe racks. Turbulent jet initiation and partial confinement can result in higher flame speeds and blast overpressures. Structural damage from vapor cloud explosions involving high-speed flames can be as severe as those involving actual detonations.

Direct initiation of detonation requires the rapid deposition of substantial amounts of energy (i.e., high explosive detonation) and is an extremely unlikely mode of accidental initiation for almost

all common fuel-air mixtures. If detonation does occur in a UVCE, it is most likely the result of accelerated flames or turbulent jet initiation leading to DDT.

At least some degree of confinement, partial obstruction of the flow paths, or a high-speed jet ignition source is required to produce DDT. The less sensitive the explosive (the larger the detonation cell size), the larger the scale and the greater the degree of confinement or obstruction is required to produce DDT. If turbulent flame-jet ignition is used, the velocity and geometric scales must be appropriately large to obtain DDT. Both confinement and obstructions provide a means of feedback between the flame-produced mean flow and the flame itself. Production of vorticity and the reflection of pressure waves are the physical mechanisms by which the feedback occurs.

The sensitivity of a given fuel-air system to direct detonation initiation and DDT can be partially assessed by laboratory measurement of the detonation cell size or computations of the detonation reaction zone length. If necessary, large scale experiments can be used to confirm these predictions of detonability. Although tentative criteria for DDT and turbulent jet initiation have been identified, more research is needed to quantify the conditions under which DDT occurs in UVCEs.

17. Tank Overpressurization

Explosion hazard zones can result from the violent rupture of an overpressurized container without combustion taking place. The energy that produces the overpressure field comes from the volume and internal pressure of the vapor space in the container. Thus, a nearly empty pressurized container of gas can be a more severe explosion hazard than a container nearly full of liquid that ruptures at the same pressure.

This section outlines the algorithm of a model that assumes a vessel ruptures in manner in which the blast wave propagates omni-directionally (See Baker [77]). It assumes a ground level, hemispherical field and yields ground level hazard zones. If the ruptured container is elevated, calculated hazard zone distances should be reduced by a factor of 1.26 to yield the radial hazard zone from the center of the explosion.

The algorithm proceeds as follows:

1. Calculate the ratio P_i/P_a where P_a is the absolute ambient pressure and P_i is the absolute internal gas pressure at which the tank is expected to rupture.
2. Compute the ratio T_i/T_a where T_a is the absolute ambient air temperature and T_i is the absolute temperature of the gas in the tank.
3. Determine the initial overpressure ratio, P_{so} , by solving the following equation by trial and error:

$$\begin{aligned}
 f &= 0 \\
 &= \ln(P_i/P_a) - \ln(1 + P_{so}) \\
 &\quad - \frac{2\gamma_i}{1 - \gamma_i} \ln \left[1 - \frac{(\gamma_i - 1)P_{so}}{2\sqrt{T_i/T_a}\sqrt{\gamma_a^2 + 0.5\gamma_a(\gamma_a + 1)P_{so}}} \right]
 \end{aligned}$$

where, γ is the ratio of specific heat at constant pressure to that at constant volume.

4. Compute the nondimensional starting distance R_o from:

$$R_o = \frac{1}{\left[\frac{\frac{4\pi}{3} \left(\frac{P_i}{P_a} - 1 \right)}{\gamma_i - 1} \right]^{1/3}} \quad (\text{B.35})$$

5. compute the value of R from:

$$R = \frac{r}{\left[\frac{V \left(\frac{P_i}{P_a} - 1 \right)}{\gamma_i - 1} \right]^{1/3}} \quad (\text{B.36})$$

where,

V = Volume of the gas in the tank

r = Distance from the center of the tank at which the side-on overpressure is desired ².

6. Locate the point associated with P_{so} and R_o on Figure B.12. This is the starting point.
7. Follow the nearest curve for P_s vs. R to the R value computed in step 5. Read the P_s value associated with this R value. If the gas vessel is on the ground and/or close to a reflecting surface, increase P_s by 100 % for R less than 1 and by 10 % for R greater than 1.
8. The side-on overpressure is determined by multiplying the above resultant value of P_s by the absolute value ambient atmospheric pressure P_a .

If the volume of the gas in the bursting tank is better represented by a cylinder ³ than a sphere, adjust the above result for side-on overpressure as follows:

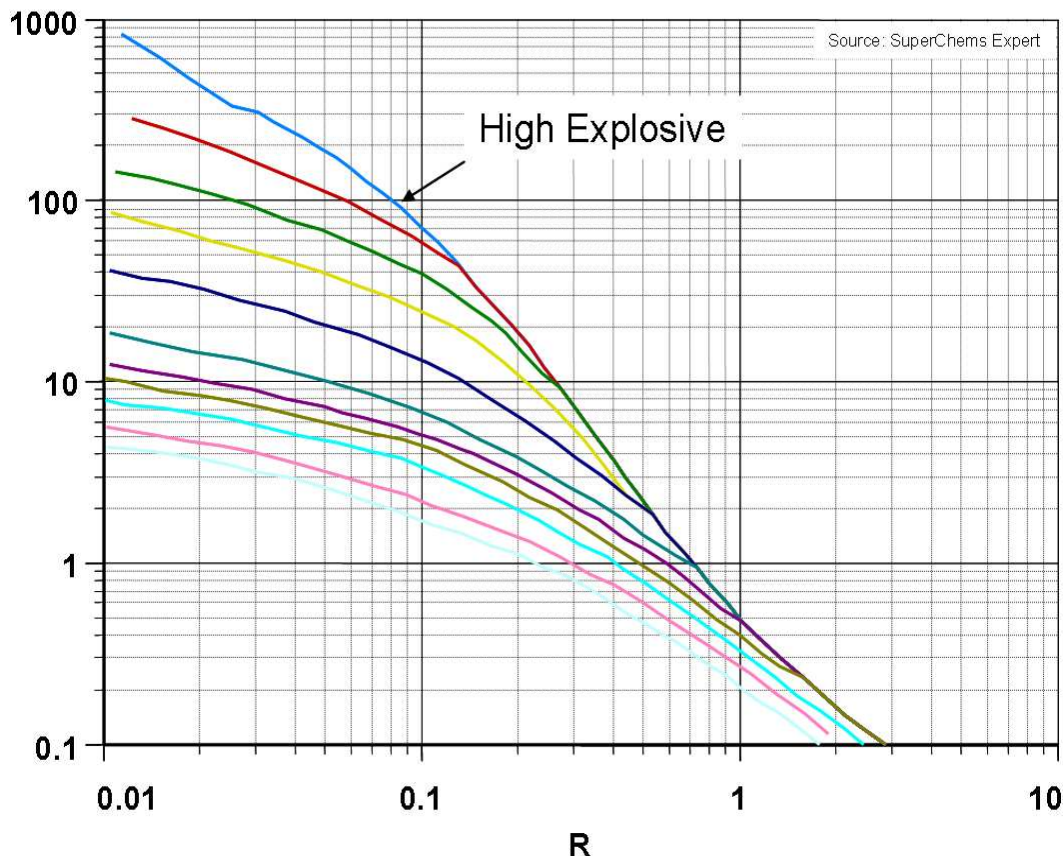
- For R less than 0.3, the calculated overpressure should be multiplied by a factor of 4 or 5.
- For R near 1.0, multiply the answer by a factor of 1.6.
- for R greater than about 3.5, multiply the answer by a factor of 1.4.

Note that the difference between spherical and cylindrical vessel bursts is only known qualitatively. Therefore, the corrections are very crude.

²The above equation is for gas vessel bursts far from reflecting surfaces. If the gas vessel is on ground, multiply V above by a factor of 2

³Although not discussed with respect to this estimation procedure, NASA workbooks typically assume cylinders have a length to diameter ratio of 10 while spheres have a ratio of one.

Figure B.12: Ps vs. R for Overpressure Calculations



18. Gas Dynamics

18.1 Example: Shock tube problem

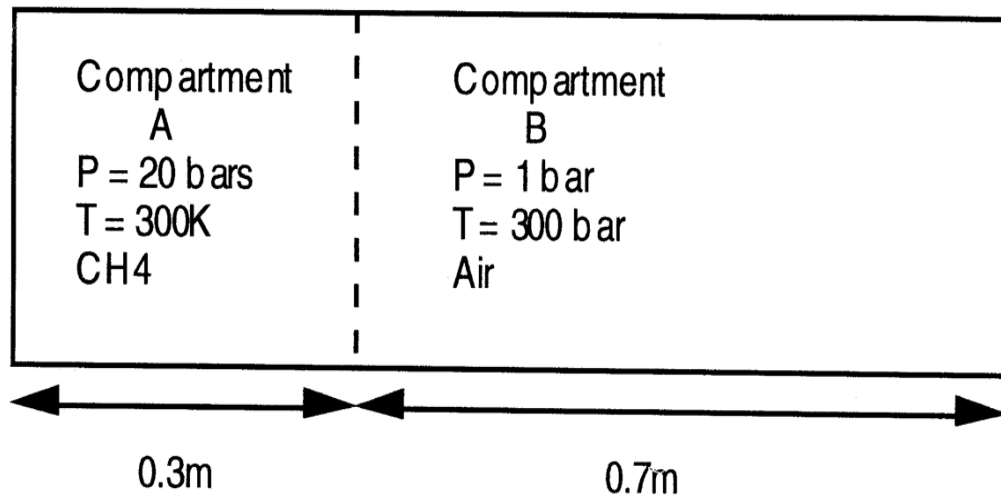
Consider a constant area horizontal hollow tube closed at both ends. The tube is separated into two compartments, A and B, using a divider. Compartment A contains natural gas at 300 K and 20 bars. Compartment B contains air at 300 K and 1 bar (see Figure B.13). The tube is at equilibrium under these conditions, and no mass or heat transfer is taking place between the tube and its surroundings or between the two compartments. If the divider is removed at time 0, calculate the time and spatial histories of pressure, velocity, and temperature. Assume the tube is frictionless. Tube length is 1 m. Compartment A is 30 percent of total volume.

18.2 Solution

Using the ideal gas assumption, the expression for energy per unit volume is rewritten as:

$$E = \frac{P}{\gamma - 1} + \frac{1}{2}\rho u^2 \quad (\text{B.37})$$

Figure B.13: Shock tube problem



In order to simplify the solution of the conservation equations, let m be defined as:

$$m = \rho u \quad (\text{B.38})$$

The conservation equations of mass, momentum, and energy become:

Continuity:

$$\frac{\partial \rho}{\partial t} + \frac{\partial m}{\partial x} = 0 \quad (\text{B.39})$$

Momentum:

$$\frac{\partial m}{\partial t} + \frac{\partial}{\partial x} \left[\frac{m^2}{\rho} \right] = - \frac{\partial P}{\partial x} \quad (\text{B.40})$$

Energy:

$$\frac{\partial E}{\partial t} + \frac{\partial}{\partial x} \left[\frac{Em}{\rho} \right] = - \frac{\partial}{\partial x} \left[\frac{Pm}{\rho} \right] \quad (\text{B.41})$$

The solution of these equations consists of a rarefaction wave traveling to the left, a contact discontinuity traveling slowly to the right of a shock traveling at a faster speed to the right. The shock reflects at the edge and collides with the contact discontinuity. Numerical solution of the resulting partial differential equations can be made easier by using proper scaling. Let x_o be defined as a

unit grid spacing. We define the following scaled variables:

$$\begin{aligned} c_o &= \sqrt{\frac{P_o}{\rho_o}} \\ t_o &= \frac{x_o}{c_o} \\ \tilde{\rho} &= \frac{\rho}{\rho_o} \\ \tilde{P} &= \frac{P}{P_o} \\ \tilde{u} &= \frac{u}{c_o} \\ \tilde{E} &= \frac{E}{P_o} \\ \tilde{Q} &= \frac{Qt_o}{P_o} \\ \tilde{t} &= \frac{t}{t_o} \\ \tilde{x} &= \frac{x}{x_o} \end{aligned}$$

Even with proper scaling, numerical difficulties are still encountered when using standard methods such as the method of lines to solve the resulting partial differential equations. Artificial dissipation is required to stabilize to solution. Let ν be the amount of artificial dissipation required to stabilize the solution. The gas dynamics equations become:

$$\frac{\partial \tilde{\rho}}{\partial \tilde{t}} + \frac{\partial \tilde{m}}{\partial \tilde{x}} = \nu \frac{\partial^2 \tilde{\rho}}{\partial \tilde{x}^2} \quad (\text{B.42})$$

$$\frac{\partial \tilde{m}}{\partial \tilde{t}} + \frac{\partial}{\partial \tilde{x}} [\tilde{m}\tilde{u}] = -\frac{\partial \tilde{P}}{\partial \tilde{x}} + \nu \frac{\partial^2 \tilde{m}}{\partial \tilde{x}^2} \quad (\text{B.43})$$

$$\frac{\partial \tilde{E}}{\partial \tilde{t}} + \frac{\partial}{\partial \tilde{x}} [\tilde{E}\tilde{u}] = -\frac{\partial}{\partial \tilde{x}} [\tilde{P}\tilde{u}] + \nu \frac{\partial^2 \tilde{P}}{\partial \tilde{x}^2} \quad (\text{B.44})$$

The amount of artificial dissipation needed decreases as the number of grid points is increased. The optimal value is found by trial and error. A similar solution to this problem is reported in Hyman.

There are different methods that are better suited for the solution of the gas dynamics equations. These methods include flux corrected transport, and remort solvers (see boris et. al).

Initial values of \tilde{E} , \tilde{m} , and $\tilde{\rho}$ are required at time 0. The density of methane at 300 K and 20 bars is calculated using the ideal gas equation of state:

$$\rho = \frac{M_w P}{R_g T} = \frac{16 \times 20 \times 10^5}{8314 \times 300} = 12.83 \text{kg/m}^3 \quad (\text{B.45})$$

The density of air is 1.163 kg/m^3 . The computation is further simplified by assuming that both methane and air have the same heat capacity ratio, i.e., $\gamma = 1.3$.

Using these values and the new scaled variables definitions, the initial conditions at $x \leq 0.3\text{m}$:

$$\begin{aligned}\tilde{\rho} &= 1 \\ \tilde{E} &= \frac{1}{\gamma - 1} = 3.33 \\ \tilde{m} &= 0\end{aligned}$$

and at $x > 0.3\text{m}$:

$$\begin{aligned}\tilde{\rho} &= 0.0906 \\ \tilde{E} &= \frac{1/20}{\gamma - 1} = 0.1667 \\ \tilde{m} &= 0\end{aligned}$$

Boundary values are required at $\tilde{x} = 0$ and $\tilde{x} = 1$. These conditions can be represented mathematically as follows:

$$\frac{\partial \tilde{\rho}}{\partial \tilde{x}} = 0 \tag{B.46}$$

$$\frac{\partial \tilde{E}}{\partial \tilde{x}} = 0 \tag{B.47}$$

$$\tilde{m} = 0 \tag{B.48}$$

The interface between fluids may be tracked using additional partial differential equations for conservation of species. Let b_i be the mass fraction of species i :

$$\frac{\partial \rho b_i}{\partial t} + \frac{1}{A} \frac{\partial}{\partial x} [\rho b_i u A] = 0 \tag{B.49}$$

The variable b_i does not require scaling, its value ranges between 0 and 1.

The interface between methane and air is tracked using one partial differential equation for methane:

$$\frac{\partial \tilde{\rho} b_0}{\partial \tilde{t}} + \frac{\partial \tilde{m} b_0}{\partial \tilde{x}} = \nu \frac{\partial^2 \tilde{\rho} b_0}{\partial \tilde{x}^2} \tag{B.50}$$

with the boundary condition:

$$\frac{\partial b_0}{\partial \tilde{x}} = 0 \tag{B.51}$$

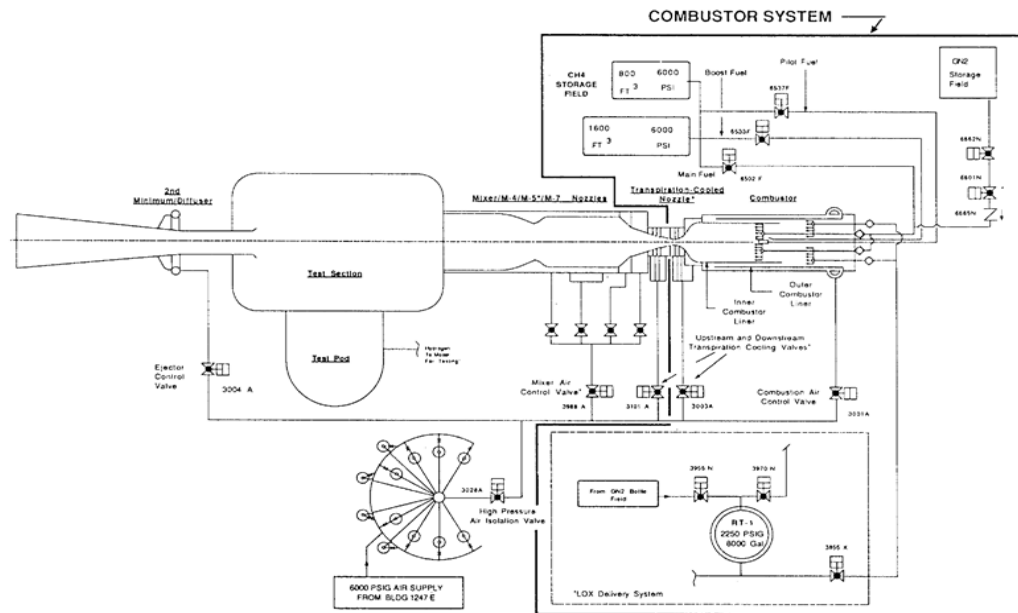
18.3 Example: Explosion gas dynamics

Consider the geometry of NASA's high temperature tunnel shown in Figure B.14. The tunnel operates at pressures ranging from 600 to 4000 psi and temperatures ranging from 2500 R to 3560

R using gaseous methane as a fuel and air as an oxidant to produce mach 4, 5, and 7 flows. The burner is located at $x=3.5$ m and the nozzle at approximately $x=8$ m.

We would like to assess potential explosion damage to the vessel following a flame-out and subsequent re-ignition leading to explosion of a stoichiometric "slug" of fuel spontaneously ignited due to turbulent mixing with the hot combustion products. Assuming both ends of the combustor are closed, using the gas dynamics equations presented earlier in the text construct a one-dimensional flame model to simulate a moving flame front towards $x=0$ at a given burning velocity. Assuming ideal gas behavior, calculate the temporal variation of pressure, temperature, velocity, and density at $x=0$ and $x=8$ m. What effect does real gas behavior has on the results. What effect does the flame speed has on the peak pressure attained and the final constant volume pressure.

Figure B.14: NASA's 8-Foot High Temperature Tunnel. (Courtesy of Langley Research Center)



18.4 Solution

Let n be the number of spatial nodes used in the analysis and dx the spatial dimension of one cell in meters:

$$dx = \frac{L}{n - 1} \tag{B.52}$$

The amount of heat released per unit mass at every cell swept by the flame is equivalent to the energy content per unit mass divided by the time it takes the flame to cross a given cell:

$$q = \frac{Q}{dt} = Q \frac{S_u}{dx} \tag{B.53}$$

Similar to the shock tube problem, we scale the conservation equations using the following new variables:

$$\begin{aligned}\tilde{A} &= \frac{A}{x_o^2} \\ \tilde{C}_v &= C_v \frac{T_o}{c_o^2} \\ \tilde{q} &= q \frac{x_o}{c_o^3} \\ \tilde{g} &= g \frac{x_o}{c_o^2} \\ \tilde{T} &= \frac{T}{T_o} \\ \tilde{R} &= R \frac{T_o}{c_o^2}\end{aligned}$$

The scaled conservation equations describing the explosion process are as follows:

Continuity

$$\frac{\partial \tilde{\rho}}{\partial \tilde{t}} = -\frac{1}{\tilde{A}} \frac{\partial}{\partial \tilde{x}} [\tilde{\rho} \tilde{u} \tilde{A}] \quad (\text{B.54})$$

Energy

$$\frac{\partial \tilde{T}}{\partial \tilde{t}} = -\tilde{u} \frac{\partial \tilde{T}}{\partial \tilde{x}} + Q \frac{S_u}{dx \tilde{C}_v} \frac{x_o}{c_o^3} - \frac{\tilde{P}}{\tilde{C}_v \tilde{\rho} \tilde{A}} \frac{\partial}{\partial \tilde{x}} [A \tilde{u}] + \frac{f \tilde{u}^3}{\sqrt{\frac{\tilde{A}}{\pi}} \tilde{C}_v} \frac{\tilde{u}}{|\tilde{u}|} + \nu \frac{\partial^2 \tilde{T}}{\partial \tilde{x}^2} \quad (\text{B.55})$$

Momentum

$$\frac{\partial \tilde{u}}{\partial \tilde{t}} = -\frac{1}{\tilde{\rho}} \frac{\partial \tilde{P}}{\partial \tilde{x}} - \tilde{u} \frac{\partial \tilde{u}}{\partial \tilde{x}} - \tilde{g} \sin \theta - \frac{f \tilde{u}^2}{\sqrt{\frac{\tilde{A}}{\pi}} |\tilde{u}|} + \nu \frac{\partial^2 \tilde{u}}{\partial \tilde{x}^2} \quad (\text{B.56})$$

Equation of state

$$\tilde{P} = \frac{\tilde{\rho} \tilde{R} \tilde{g} \tilde{T}}{M_w} \quad (\text{B.57})$$

The boundary conditions for closed ends are:

$$\frac{\partial \tilde{P}}{\partial \tilde{x}} = 0 \quad (\text{B.58})$$

$$\frac{\partial \tilde{T}}{\partial \tilde{x}} = 0 \quad (\text{B.59})$$

$$\frac{\partial \tilde{\rho}}{\partial \tilde{x}} = 0 \quad (\text{B.60})$$

$$\tilde{u} = 0 \quad (\text{B.61})$$

The term ν is an artificial dissipation term used to stabilize the numerical solution. Its value is set at 0.05.

Bibliography

- [1] H. Ozog, G. A. Melhem, B. van den Berg, and Paul Mercx. Facility siting case study demonstrating benefit of analyzing blast dynamics. In *International Conference and Workshop on Process Safety Management and Inherently Safer Processes*, pages 293–315. AIChE/CCPS, October 1996.
- [2] G. A. Melhem. An overview of explosion modeling for facility siting. In *DIERS Users Group Meeting*. AIChE, October 2010.
- [3] J. Shepherd, G. A. Melhem, and P. Athens. Unconfined vapor cloud explosions: A new perspective. In *International Conference and Workshop on Modeling*. AIChE/CCPS, 1991.
- [4] A. C. van den Berg. The multi-energy method. a framework for vapour cloud explosion blast prediction. *Journal of Hazardous Materials*, 12:1–10, 1985.
- [5] M. J. Tang and Q. A. Baker. A new set of blast curves from vapor cloud explosion. *Process Safety Progress*, 18(4):235–240, 1999.
- [6] TNO/Century Dynamics Ltd. Autoreagas theory manual and user documentation, 1994.
- [7] S. E. Rigby, A. Tyas, T. Bennett, S. D. Clarke, and S. D. Fay. The negative phase of the blast load. *International Journal of Protective Structures*, 5(1):1–20, 2014.
- [8] S. E. Rigby, A. Tyas, S. D. Fay, S. D. Clarke, and J. A. Warren. Validation of semi-empirical blast pressure predictions for far field explosions - is there inherent variability in blast wave parameters? In *6th International Conference on Protection of Structures Against Hazards*, 2014.
- [9] G. A. Melhem, P. A. Croce, and H. Abraham. Data summary and analysis of NFPA’s BLEVE tests. *Process Safety Progress*, 12(2):76–82, 1993.
- [10] H. Ayvazyan et al. *Structures to Resist the Effects of Accidental Explosions, Volume III*. U.S. Army Armament Research, Development and Engineering Center. AD-A176-673, 1986.
- [11] ASCE. *Design of Blast Resistant Buildings in Petrochemical Facilities*. Number ISBN 0-7844-0265-5. American Society of Civil Engineers, 1997.
- [12] N. M. Newmark and J.D. Haltiwanger. *Air Force Design Manual - Principles and Practices for Design of Hardened Structures*. Number AFSWC-TDR-62-138. U.S. Air Force, 1962.

- [13] S. Glasstone. *The Effects of Nuclear Weapons*. U.S. A.E.C., U.S. Government Printing Office, 1962.
- [14] F. P. Lees. *Loss Prevention in the Process Industries, Volumes 1 and 2*. Butterworths, 1980.
- [15] H. Giesbiecht. Evaluation of vapor cloud explosions by damage analysis. *Journal of Hazardous Materials*, 17:247–257, 1988.
- [16] R. G. Zalosh. Dispersal and blast wave analysis for vces. *3rd International Symposium on Loss Prevention and Safety Promotion in the Process Industries*, (2):7/542–7/555, 1980.
- [17] K. Gugan. *Unconfined Vapor Cloud Explosions*. The Institution of Chemical Engineers, 1978.
- [18] B. J. Wiekema. Vapor cloud explosion model. *J. of Hazardous Materials*, 3:221–232, 1980.
- [19] J. H. S. Lee and I. O. Moen. The mechanism of transition from deflagration to detonation in vapor cloud explosions. *Prog. Energy Combustion Science*, 6:359–389, 1980.
- [20] J. G. Marshall. The size of flammable clouds arising from continuous releases into the atmosphere - Part 2. *Institute of Chemical Engineers Symposium Series*, (58):11–23, 1980. Note that Part I is in Institute of Chemical Engineers Symposium Series No. 49, pp. 99-109, 1977.
- [21] W. Geiger and R. Synofzik. A simple model for the explosion of pancake-shaped vapour clouds. In *3rd International Symposium on Loss Prevention and Safety Promotion in the Process Industries*, 1980.
- [22] R. A. Strehlow. Blast waves generated by accidental explosions. Technical report, Proc. of the International Symposium on Shock Tubes and Waves, 1981. AD-P000227.
- [23] H. Phillips. U.k. research into unconfined vapor cloud explosions. Technical report, University of Waterloo Press, 1982. Fuel-Air Explosions.
- [24] H. Phillips. *UCVEs - Evaluation of Gugan's Book*. The Chemical Engineer, June 1981.
- [25] K. Hasegawa and K. Sato. A study of the blast wave from deflagrative explosions. *Fire Safety Journal*, 5:265–274, 1983.
- [26] C. Koch et al. Transition from slow deflagration to detonation. Technical report, Commission of the European Communities, 1984. NTIS: PB85-186641/XAB.
- [27] C. J. M. Wingerden and A. C. van den Berg. On the adequacy of numerical codes for the simulation of vapour cloud explosions, Part 1. Technical report, Nuclear Science and Technology, Commission of the European Communities, 1984. Report No. EUR 9541 EN/I.
- [28] J. H. Pickles and S. H. Bittleston. Unconfined vapor cloud explosions - the asymmetrical blast from an elongated cloud. *Combustion and Flame*, 51:45–53, 1983.
- [29] P. H. Taylor. Vapor cloud explosion - the directional blast wave from an elongated cloud with edge ignition. *Combustion Science and Technology*, 44:207–219, 1985.

- [30] K. J. Dorge, D. Pangritz, and H. Wagner. Experiments on velocity augmentation of spherical flames by grids. *Acta Astronautica*, 3:1067–1076, 1976.
- [31] J. Brossard et al. Truly unconfined explosions of ethylene-air mixtures. *Prog. Astronautics and Aeronautics*, 106:90–106, 1986.
- [32] H. Wagner. Some experiments about flame acceleration. pages 77–99. Proc. of the Intl. Specialist Conf. on Fuel-Air Explosions, U. Waterloo Press, 1981.
- [33] I. O. Moen, M. Donato, R. Knystautas, and J. H. Lee. Flame acceleration due to turbulence produced by obstacles. *Comb. Flame*, 39:21–32, 1980.
- [34] I. O. Moen, M. Donato, R. Knystautas, J. H. Lee, and H. Wagner. Turbulent flame propagation and acceleration in the presence of obstacles. *Prog. Astronautics and Aeronautics*, 75:33–47, 1981.
- [35] I. O. Moen, J. H. Lee, B. H. Hjertager, K. Fuhre, and R. K. Eckhoff. Pressure development due to turbulent flame propagation in large-scale methane-air explosions. *Comb. Flame*, 47:31–52, 1982.
- [36] J. H. Lee, R. Knystautas, and A. Freiman. High-speed turbulent deflagrations and transition to detonation in H₂-air mixtures. *Comb. Flame*, 56:227–239, 1984.
- [37] C. Chan, I. O. Moen, and J. H. Lee. Influence of confinement on flame acceleration due to repeated obstacles. *Comb. Flame*, 49:27–39, 1983.
- [38] P. A. Urtiew, J. Brandeis, and W. J. Hogan. Experimental study of flame propagation in semiconfined geometrics with obstacles. *Combust. Sci. Tech.*, 30:103–119, 1983.
- [39] C. J. van Wingerden and J. P. Zeeuwen. Investigation of explosion enhancing properties of a pipe-rack-like obstacle array. *Prog. Astronautics and Aeronautics*, 106:53–65, 1986.
- [40] M. P. Sherman, S. R. Tieszen, W. B. Benedick, J. W. Fisk, and M. Carcassi. The effect of transverse venting on flame acceleration and transition to detonation in a large channel. *Prog. Astronautics and Aeronautics*, 106:66–89, 1986.
- [41] M. P. Sherman, S. R. Tieszen, and W. B. Benedick. FLAME facility. Technical Report SAND85-1264, Sandia National Laboratories, 1989.
- [42] S. R. Tieszen, M. P. Sherman, and W. B. Benedick. Flame acceleration studies in the MINI-FLAME facility. Technical Report SAND89-0859, Sandia National Laboratories, 1989.
- [43] I. O. Moen, A. Sulmistras, B. H. Hjertager, and J. R. Bakke. Turbulent flame propagation and transition to detonation in large fuel-air clouds. *21st Symp. (Intl.) on Combustion*, pages 1617–1627, 1986.
- [44] R. Knystautas, J. H. Lee, I. Moen, and H. Wagner. Direct initiation of spherical detonation by a hot turbulent gas jet. *17th Symp. (Intl.) on Combustion, The Combustion Institute*, pages 1235–1245, 1978.

- [45] M. Schildknecht, W. Geiger, and M. Stock. Flame propagation and pressure buildup in a free gas-air mixture due to jet ignition. *Prog. Astronautics and Aeronautics*, 94:474–490, 1984.
- [46] I.O. Moen, D. Bjerketvedt, A. Jenssen, and P.A. Thibault. Transition to detonation in a large fuel-air cloud. *Comb. Flame*, 61:285–291, 1985.
- [47] D.J. Mackay, Murray. S.B., I.O. Moen, and P.A. Thibault. Flame-jet ignition of large fuel-air clouds. *22nd Symp. (Intl.) on Combustion, The Combustion Institute*, pages 1339–1353, 1988.
- [48] U.S. Army Corps of Engineers. User's guide for the single degree of freedom blast effects design spreadsheet (SBEDS). Technical Report PDC TR-06-02 Rev 1, U.S. Army Corps of Engineers, 2008.
- [49] R. J. Harris and M. J. Wickens. Understanding vapour cloud explosions - an experimental study, 55th autumn meeting of the institution of gas engineers, kensington, UK, 1989.
- [50] A. C. Van den Berg and A. Lannoy. Methods for vapour cloud explosion blast modelling. *J. of Haz. Mat.*, 34:151–171, 1993.
- [51] Center for Chemical Process Safety of the American Institute of Chemical Engineers. Guidelines for evaluating process buildings for external explosions and fires, 1996.
- [52] J. P. Zeeuwen, C. J. M. Van Wingerden, and R. R. Dauwe. Experimental investigation into the blast effect produced by unconfined vapor cloud explosions. In *4th Int. Symp. Loss Prevention and Safety Promotion in the Process Industries. Harrogate, UK, IChemE Symp. Series 80*, pages D20–D29. IChemE, 1983.
- [53] A. J. Harrison and J. A. Eyre. The effect of obstacle arrays on the combustion of large premixed gas/air clouds. *Comb. Science and Techn.*, 52:121–137, 1987.
- [54] C. J. M. Van Wingerden. Experimental investigation into the strength of blast waves generated by vapour cloud explosions in congested areas. In *6th Int. Symp. Loss Prevention and Safety Promotion in the Process Industries, Oslo, Norway*, pages 26–1/26–16, 1989.
- [55] A. C. Van den Berg and J. B. M. M. Eggen. GAME - guidance for the application of the multi-energy method. In *The Second International Specialist Meeting on Fuel-Air Explosions Bergen, Norway, June 27/28, 1996*.
- [56] W.E. Baker, P.E. Cox, P.S. Westine, J.J. Kulesz, and R.A. Strehlow. Explosion hazards and evaluation. *Fundamental Studies in Engineering*, 5:127–140, 1983.
- [57] R. A. Strehlow, R.T. Luckritz, A.A. Adamczyk, and S.A. Shimpi. The blast wave generated by spherical flames. *Combustion and Flame*, 35:297–310, 1979.
- [58] Chemical Center for Process Safety (CCPS). *Guidelines for Evaluating the Characteristics of Vapor Cloud Explosions, Flash Fires, and BLEVES*. American Institute of Chemical Engineers, 1994.

- [59] Q. A. Baker, M. J. Tang, E. A. Scheier, and G. J. Silva. Vapor cloud analysis. *Process Safety Progress*, 15(2):106–109, 1996.
- [60] J. Pierorazio, J. K. Thomas, Q. A. Baker, , and D. E. Ketchum. An update to the baker-strehlow-tang vapor cloud explosion prediction methodology flame speed table. *Process Safety Progress*, 24(1):59–65, 2005.
- [61] I.O. Moen, P.A. Thibault, and J.A. Funk. Blast waves from non-spherical fuel-air explosions. *Proceedings of the 8th International Symposium on Military Applications of Blast Simulation*, Spiez, Switerzland, 1983.
- [62] C. K. Westbrook and P. A. Urtiew. Prediction of chemical kinetic parameters in gaseous detonation. *19th Symp. (Intl.) on Combustion, The Combustion Institute*, pages 615–623, 1982.
- [63] J. H. S. Lee. Dynamic parameters of gaseous detonation. *Ann.Rev. Fluid Mech.*, 16:311–316, 1984.
- [64] J. E. Shepherd. Chemical kinetics of hydrogen-air-diluent detonations. *Prog. Astronautics and Aeronautics*, 106:263–292, 1986.
- [65] J. E. Shepherd, I.O. Moen, S.B. Murray, and P.A. Thibault. Analyses of the cellular structure of detonations. *21st Symp. (Intl.) on Combustion, The Combustion Institute*, pages 1649–1658, 1987.
- [66] J. H. S. Lee. Initiation of gaseous detonation. *Ann. Rev. Phys. Chem.*, 28:75–104, 1977.
- [67] G. Bach, R. Knystautas, and J.H.S. Lee. Initiation of spherical detonation. *13th Symp. (Intl.) on Combustion, The Combustion Institute*, pages 1097–1110, 1970.
- [68] W. B. Benedick, C. Guirao, R. Knystautas, and J. H. Lee. Critical charge for the direct initiation of detonation in gaseous fuel-air mixtures. *Prog. Astronautics and Aeornautics*, 106:181–202, 1986.
- [69] R. Knystautas, J.H.S. Lee, O. Peraldi, and C.K. Chan. Transmission of a flame from a rough to a smooth-walled tube. *Prog. Astronautics and Aeornautics*, 106:37–52, 1986.
- [70] O. Peraldi, R. Knystautas, and J.H. Lee. Criteria for transition to detonation in tubes. *21st Symp. (Intl.) on Combustion, The Combustion Institute*, pages 1629–1637, 1988.
- [71] P. K. Barr. Simulation of flame propagation through vorticity regions using the discrete vortex method. Report SAND84-8715, Sandia National Laboratories, 1984.
- [72] R. J. Cattolica, P. K. Barr, and N. N. Mansour. Propagation of a premixed flame in a divided-chamber combustor. *Comb. Flame*, 77:101–121, 1989.
- [73] P. K. Barr. Acceleration of a flame by flame-vortex interactions. accepted for publication in *Comb, Flame* 1990.

- [74] B. H. Hjertager. Influence of turbulence on gas explosions. *J. Hazardous Materials*, 9:315–346, 1984.
- [75] B. H. Hjertager. Simulation of transient compressible turbulent reactive flow. *Combust. Sci. Tech.*, 27:159–170, 1982.
- [76] K. D. Marx. Development and application of a computer model for large-scale flame acceleration experiments. Technical Report SAND87-8203, Sandia National Laboratories, 1987.
- [77] W. E. Baker et. al. *Explosion Hazards and Evaluation*. Elsevier, 1983.

About the Author



Dr. Melhem is an internationally known pressure relief and flare systems, chemical reaction systems, process safety, and risk analysis expert. In this regard he has provided consulting, design services, expert testimony, incident investigation, and incident reconstruction for a large number of clients. Since 1988, he has conducted and participated in numerous studies focused on the risks associated with process industries fixed facilities, facility siting, business interruption, and transportation.

Prior to founding ioMosaic Corporation, Dr. Melhem was president of Pyxsys Corporation; a technology subsidiary of Arthur D. Little Inc. Prior to Pyxsys and during his twelve years tenure at Arthur D. Little, Dr. Melhem was a vice president of Arthur D. Little and managing director of its Global Safety and Risk Management Practice and Process Safety and Reaction Engineering Laboratories.

Dr. Melhem holds a Ph.D. and an M.S. in Chemical Engineering, as well as a B.S. in Chemical Engineering with a minor in Industrial Engineering, all from Northeastern University. In addition, he has completed executive training in the areas of Finance and Strategic Sales Management at the Harvard Business School. Dr. Melhem is a Fellow of the American Institute of Chemical Engineers (AIChE) and Vice Chair of the AIChE Design Institute for Emergency Relief Systems (DiERS).

Contact Information

Georges. A. Melhem, Ph.D., FAIChE
E-mail. melhem@iomosaic.com

ioMosaic Corporation
93 Stiles Road
Salem, New Hampshire 03079
Tel. 603.893.7009, x 1001
Fax. 603.251.8384
web. www.iomosaic.com



US Offices

New Hampshire (Salem) –
Headquarters

Texas (Houston)

Minnesota (Minneapolis)

California (Berkeley)

International Offices

Kingdom of Bahrain (Al Seef)

United Kingdom (Bath)

Software Solutions



[Process Safety Enterprise[®]](#)

Centralize the process safety management lifecycle to accelerate business goals



[Process Safety Office[®]](#)

Identify, evaluate, and control process hazards with tools used by process safety consultants



[Process Safety Learning[®]](#)

Build your process safety competencies incrementally with online training



[Process Safety tv[®]](#)

View, share, and discuss PSM worldwide on a secure platform

Contact Us

www.ioMosaic.com

sales@ioMosaic.com

1.844.ioMosaic

About ioMosaic Corporation

Through innovation and dedication to continual improvement, ioMosaic has become a leading provider of integrated process safety and risk management solutions. ioMosaic has expertise in a wide variety of areas, including pressure relief systems design, process safety management, expert litigation support, laboratory services, training and software development.

As a certified ISO 9001:2015 Quality Management System (QMS) company, ioMosaic offers integrated process safety and risk management services to help you manage and reduce episodic risk. Because when safety, efficiency, and compliance are improved, you can sleep better at night. Our extensive expertise allows us the flexibility, resources, and capabilities to determine what you need to reduce and manage episodic risk, maintain compliance, and prevent injuries and catastrophic incidents.

Our mission is to help you protect your people, plant, stakeholder value, and our planet.

[Consulting Services](#)

- Asset Integrity
- Auditing and Due Diligence
- Combustible Dust Hazard Analysis and Testing
- Facility Siting
- Fault Tree/SIL/SIS Analysis
- Fire and Explosion Dynamics
- Incident Investigation, Litigation Support and Expert Testimony
- Liquefied Natural Gas Safety
- Pipeline Safety
- Process Engineering Design and Support
- Process Hazards Analysis (PHA)
- Process Safety Management (PSM)
- Reactive Chemicals Evaluation and Testing
- Relief and Flare Systems Design and Evaluations
- Risk Management Program Development
- Quantitative Risk Assessments (QRA)
- Software Solutions
- Structural Dynamics
- Training

[Laboratory Testing Services \(ISO accredited\)](#)

- Chemical Reactivity
- Battery Safety
- Combustible Dust
- Specialized Testing